UNIVERSIDADE DE SÃO PAULO

ESCOLA POLITÉCNICA

Amir Hossein Omidvar

Non enzymatic glucose biosensor design, fabrication, and application

São Paulo

2023

Amir Hossein Omidvar

Non enzymatic glucose biosensor design, fabrication, and application

Versão Corrigida

Tese apresentada à Escola Politécnica da Universidade de São Paulo para a obtenção do título de Doutor em Ciências.

Área de Concentração :Microeletrônica

Orientador: Prof. Dr. Gustavo Pamplona Rehder

São Paulo

2023

Este exemplar foi revisado e corrigido em relação à versão original, sob responsabilidade única do autor e com a anuência de seu orientador.

São Paulo, 21 de Julho de 2023

Assinatura do autor: _____

Assinatura do orientador: _____

Catalogação-na-publicação

Omidvar, Amir Hossein
Projeto, fabricação e aplicação de biosensores de glicose não enzimáticos / A. H. Omidvar -- versão corr. -- São Paulo, 2023.
112 p.

Tese (Doutorado) - Escola Politécnica da Universidade de São Paulo. Departamento de Engenharia de Sistemas Eletrônicos.

1.Sensores de micro-ondas 2.Polimeros de impressão 3.Glicose 4.Filmes finos 5.Biosensores I.Universidade de São Paulo. Escola Politécnica. Departamento de Engenharia de Sistemas Eletrônicos II.t.

Acknowledgement

First and foremost, I am extremely grateful to my supervisors, Prof. Dr. Gustavo Rehder and Prof. Dr. Ariana Lacorte Caniato Serrano for their invaluable advice, continuous support, and patience during my PhD study. Their immense knowledge and plentiful experience have encouraged me in all the time of my academic research and daily life. I would also like to thank Prof. Dr. Jonas Gruber and Dr. Wellington B. Gonçalves for their technical support on my study. I would like to extend my sincere gratitude and appreciation to all the dedicated technicians in the microelectronic lab and physics department whose invaluable expertise, assistance, and support were essential in the successful completion of this experiment.. Finally, I would like to express my gratitude to my wife. Without her tremendous understanding and encouragement in the past few years, it would be impossible for me to complete my study.

Resumo

O diabetes é uma das quatro principais doenças não transmissíveis e se tornou uma das doenças que mais crescem no mundo. Será a sétima principal causa de morte em todo o mundo até 2030. A Federação Internacional de Diabetes (IDF) divulgou um novo relatório que demonstra que a população global com diabetes atingiu 537 milhões, aumentando 16% desde sua estimativa anterior em 2019. Infelizmente, não há cura conhecida para esta condição crônica de saúde; a única alternativa para prevenir complicações para pacientes com diabetes é monitorar constantemente seus níveis de glicose no sangue. Além disso, o intervalo seguro para os níveis de glicose no sangue é muito estreito (entre 80-120 mg/dl). Portanto, o método de detecção deve ser capaz de detectar uma ligeira mudança na concentração nesta faixa. Para medir o nível de glicose, os biossensores são muito práticos. Um biossensor é um transdutor capaz de converter uma resposta biológica em um sinal mensurável.

É apresentado um novo polímero de impressão molecular biossensorial com microfluido de micro-ondas sensível e de baixo custo. O dispositivo sensor é baseado em ressonadores de stub duplos para caracterizar soluções de glicose na água. A ponta de um dos stubs é revestida com MIP para aumentar a seletividade do sensor e, portanto, a sensibilidade em comparação com o polímero não revestido ou não impresso. O sensor foi fabricado em substrato FR4 para fins de baixo custo. Na presença do MIP, observou-se que o sensor carregado com uma solução de glicose variando de 50 mg/dL a 400 mg/dL experimentou uma mudança de frequência de absorção de 73 MHz quando as soluções fluem em um canal microfluídico passando pela área de detecção, enquanto o sensor Descobriu-se que o LLD do sensor era de 2,4 ng/dL. Os resultados experimentais mostraram uma alta sensibilidade de 1,3 MHz /(mg/dL) em termos de frequência de absorção.

Palavras-chaves: Ressonadores de microondas; Polímero de impressão molecular; Biossensor; Glicose; Filmes finos, nitreto de alumínio.

Abstract

Diabetes is one of the four main noncommunicable diseases and has become one of the fastest-growing diseases in the world. It will be the seventh leading cause of death worldwide by 2030. The International Diabetes Federation (IDF) has released a new report that demonstrates the global population with diabetes has reached 537 million, increasing 16% since their previous estimation in 2019.

Unfortunately, there is no known cure for this chronic health condition; the only alternative to prevent complications for diabetes patients is constantly monitoring their blood glucose levels. Also, the safe range for blood glucose levels is very narrow (between 80-120 mg/dl). Therefore, the sensing method should be able to detect a slight change in concentration in this range. In order to measure the glucose level, biosensors are very practical. A biosensor is transducer capable of converting a biological response into a measurable signal.

A novel, low-cost, sensitive microwave microfluidic glucose detecting biosensor incorporating molecularly imprinted polymer is presented. The sensing device is based on dual stub resonators to characterize water glucose solutions. The tip of one of the stubs is coated with MIP to increase the selectivity of the sensor and hence the sensitivity compared to the uncoated or non-imprinted polymer one. The sensor was fabricated on an FR4 substrate for low-cost purposes. In the presence of the MIP, the sensor load-ed with a glucose solution ranging from 50 mg/dL to 400 mg/dL was observed to experience an absorption frequency shift of 73 MHz when the solutions flow in a microfluidic channel passing sensing area, while the Lower Limit of Detection (LLD) of the sensor was discovered to be 2.4 ng/dL. The experimental results showed a high sensitivity of 1.3 MHz /(mg/dL) in terms of absorption frequency.

Keywords: Microwave resonators; Molecular imprinted polymer; Biosensor; Glucose; Thin film; Aluminum nitride.

Contents

List of Figures

List of Abbreviations

IoMT	Internet of Medical Things
WHO	Work Health Organization
IDF	International Diabetes Federation
HA1c	hemoglobin A1c
BG	Blood Glucose
SMBG	Self- monitoring of blood glucose
DM	Diabetes Mellitus
GOD	Glucose oxidase
MIT	Molecular Imprinting Technology
MIPs	Molecular Imprinted Polymers
FBAR	Film Bulk Acoustic Resonator
AlN	Aluminum nitride
LLD	Low limit of Detection
BAW	Bulk Acoustic Waves
SAW	Surface Acoustic Waves
QCM	Quartz Crystal Microbalance
SH-APM	Shear Horizontal Acoustic Plate Modes
Sc-AlN	scandium-doped aluminum nitride
ZnO	zinc oxide
TFBAR	Thin Film Bulk Acoustic Resonators
SMR	Bragg acoustic mirror
MUT	material of the test
CMOS	complementary metal oxide semiconductor
MEMS	MicroElectroMechanical systems
DMTL	Transmission Line
CSRR	Complementary Split-Ring Resonator
PDMS	Polydimethylsiloxane
AAc	Acrylic acid

PMMA	Poly (methyl methacrylate)
EGDMA	Ethylene glycol Di methacrylate
AIBN	2,2′-azo-bis-isobutyronitrile
DMSO	Dimethyl sulfoxide
NIP	non-imprinted polymer
PMMA	Polymethyl methacrylate
o-PD	o-Phenylenediamine
ACPA	4,4′-Azobis (4-cyanopentanoic acid)
PML	Perfectly Matched Layer
Mo	molybdenum
Si	silicon
PZT	Lead zirconate titanate
XRD	X-ray diffraction
AAO	Anodic Aluminum Oxide
KOH	**Potassium hydroxide**
ADS	Advanced Digital Systems
VNA	vector network analyzer
DUT	device under test
IF	imprinting factor

Chapter 1: Introduction

The way healthcare is delivered is completely changing due to the Internet of Medical Things (IoMT). The healthcare sector and its related industries have embraced IoMT technology in nearly every stage of the healthcare process, regardless of being relatively late adopters. The IoMT relies heavily on sensors. They make it possible to develop an ecosystem for gathering information about a particular environment and processing it so it can be monitored, managed, and controlled more effectively. One of the technologies that can be useful in health monitoring applications is the passive sensor. They collect target data by detecting vibrations, light, heat, radiation, or other phenomena in the subject's environment. They stand in contrast to active sensors, which use transmitters to send a signal, a wavelength of light, or electrons that are then reflected off the target and collected data by the sensor is shown in Figure 1.1.

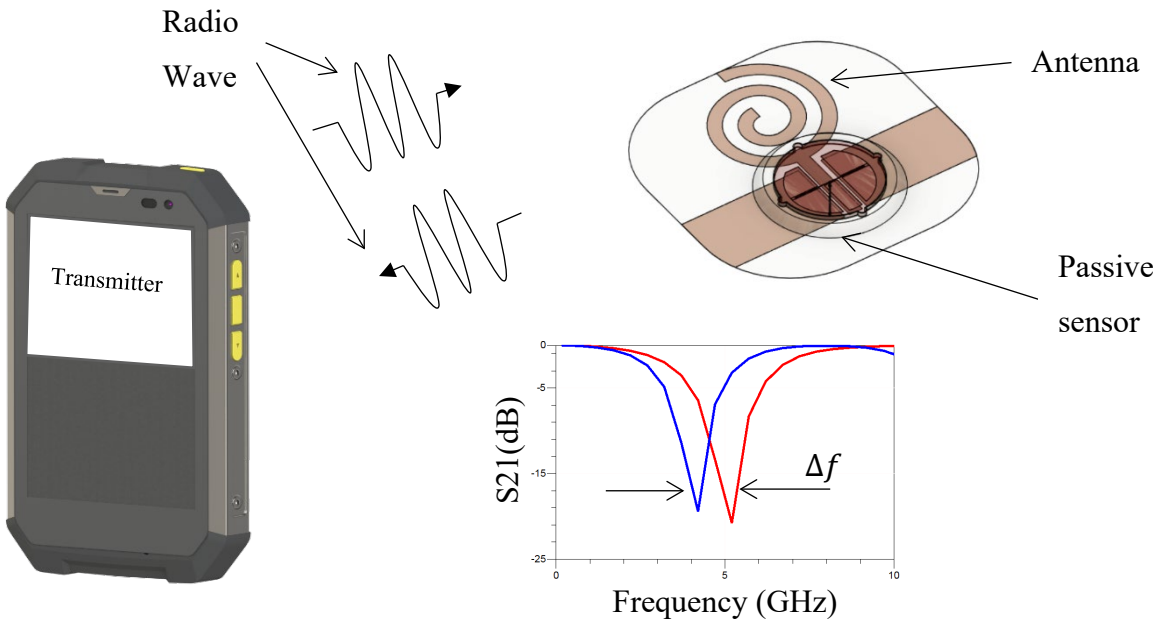

Figure 1. 1 Passive sensor concept (designed by author)

Chronic noncommunicable diseases are the leading cause of death globally. According to the Work Health Organization (WHO) report, it increased to 7 out of 10 from 4 out of 10 in 2000 ("Noncommunicable diseases", 2022). Diabetes is one of the four main noncommunicable diseases and has become one of the fastest-growing diseases in the world. It will be the seventh leading cause of death worldwide by 2030 ("The top 10 causes of death", 2020). The International Diabetes Federation (IDF) has released a new report that demonstrates the global population with diabetes has reached 537 million, rising 16% since their previous estimation in 2019 (International Diabetes Federation., 2019). The passive sensor may be helpful for those with diabetes due to diabetes' high prevalence in the world.

People with diabetes is diagnosed with severe hyperglycemia which results in several complications, including kidney failure, nerve damage, cardiovascular diseases, and damage to the blood vessels if not controlled(Association, 2019). Unfortunately, there is no known cure for this chronic health condition, and it is estimated over a million deaths are related to poor management of blood glucose(Van Dieren et al., 2010). The only alternative to prevent complications for diabetes patients is constantly monitoring their blood glucose levels and it is valuable in clinical diagnosis and individual evaluation.

Diabetes is diagnosed and managed using a variety of laboratory tests. In addition to hemoglobin A1c (HbA1c) levels, blood glucose (BG) levels are the main diagnostic criteria for diabetes (Association, 2010) and is an effective tool for patient monitoring. One tool that has been proven to be effective in managing diabetes is Self- monitoring of blood glucose (SMBG) (Boutati & Raptis, 2009; Tunis & Minshall, 2010). In order to postpone or even avoid the progress of vascular diseases such as microvascular and macrovascular, self-monitoring blood glucose level is important in managing diabetes and maintaining it in a safe range is essential.

Various glucose-measuring devices have been created based on doctors` recommendations for keeping normal blood glucose. Biosensor technology is advancing rapidly and plays a significant role in the provision of practical analytical tools with numerous applications, particularly in medicine. Although many glucose biosensors for diabetes mellitus (DM) have been developed until today, utilizing various methods, each has potential value in diagnostic applications; none of them can provide continuous measurement, micro/nano sample volume, minimal invasive, low limits of detection, high sensitivity, and require tiny amounts of power to

sense at the same time. Thus, blood glucose monitoring technology has a lot to overcome, and provides opportunities for further research.

Biosensing technologies are constantly being examined, and two types of optical(Zhong & Jang, 2014) and electrochemical (Heller & Feldman, 2008) biosensors are available in the market. Since 1962, when the first electrode with a glucose oxidase coating was introduced, electrochemical sensing technology has dramatically succeeded in blood glucose detection. It would be no exaggeration to say that most blood glucose meters on the market today are based on highly sensitive and reliable electrochemical blood glucose measurement technology. The majority of these conventional glucose sensors are based on enzymatic methods adapting different approaches such as electrochemical, colorimetric, and chemiluminescence (Carneiro et al., 2005; Chen et al., 1999; J. Li & Lin, 2007). However, these biosensors have limitations, such as, vulnerability of enzyme to deactivation, invasiveness, and limited power source, which restrict their application possibilities. As a result, it is essential to present new detection technologies in order to overcome the limitations of electrochemical biosensors and close the gap in BG monitoring technology.

Turner defined biosensor as a "compact analytical device or unit incorporating a biological or biological derived sensitive recognition element integrated or associated with a physio-chemical transducer" (Turner, 2000) showed in Figure 1.2. The following three components construct a biosensor: (1) Sensitive components that identify the target molecules among the molecules of different chemicals. (2) A transducer element for converting the biorecognition response into a recognizable electrical signal. (3) An analysis and display component that can process the electric signal extracted from the reaction. Examples of molecular recognition elements include enzymes, nucleic acids, receptors, lectins microorganisms and antibodies. Electrochemical, optical, thermometric, piezoelectric, and magnetic transducers are the five major types of transducers.

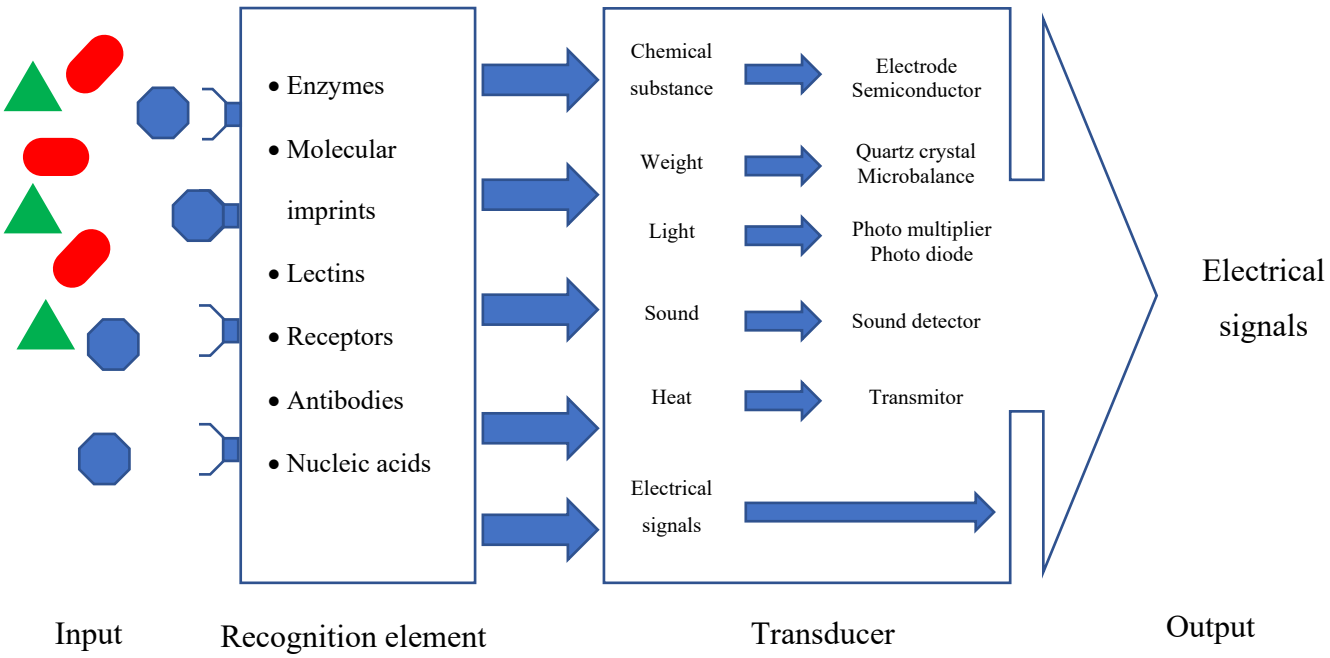

Figure 1.2 Principal of Biosensor (Turner, 2000)

The vast majority of glucose biosensors, due to their high sensitivity, reproducibility, ease of maintenance, and low cost, are utilized an electrochemical method to measure glucose levels. Amperometric, conductometric, and potentiometric sensors are the three types of electrochemical sensors. The most popular technique in commercially available devices is enzymatic amperometric, which has been the subject of in-depth study over the past ten years. This sensor measures the current is produced by electrons while exchanging between a biological system and an electrode, either directly or indirectly. These sensors require an external power source restricted to more traditional energy sources like lithium batteries.

1.1 Sensitive elements

Redox enzyme biocatalysts are receiving more and more attention in developing electronic biomaterials and devices in various fields, such as clinical, industrial, and environmental applications. Glucose oxidase (GOD), a commonly used enzyme, is a reagent used extensively in medical diagnostics, particularly for detecting glucose in the blood.

Clark and Lyons (Clark & Lyons, 1962) were the first presenters in 1962 who developed enzyme-coated electrodes for detecting glucose. They initially utilized glucose oxidase (GOD) enzyme, based on a co-product of enzymatic oxidation of glucose molecules by tracking H_2O_2 to detect and measure glucose.

$$glucose + O_2 + H_2O \xrightarrow{GOD} glucose\ acid + H_2O_2$$

Furthermore, the glucose concentration can be detected indirectly via oxygen electron transfer:

$$O_2 + 4H^+ + 4e^- \rightarrow 2\,H_2O_2$$

Considering that Updike and Hicks created the first glucose biosensor in 1962, immobilizing and stabilizing GOD has provided electrochemically simplified glucose analysis (Updike & Hicks, 1967b, 1967a). The main problem was that in order to increase selectivity, a high operational potential was needed for the amperometric measurement of hydrogen peroxide (Yoo & Lee, 2010). The limitations of first-generation glucose biosensors were addressed by the introduction of redox mediators, which move electrons from the enzyme to the surface of the working electrode (Liu Jie & Wang Joseph, 2001). During the ’80s, great efforts were devoted to the development of redox mediator-based glucose biosensors as the second generation of glucose biosensors (Cass et al., 1984; Frew & Hill, 1987).

Third-generation glucose biosensors developed in the 1990s, in which there were no reagents based on direct interaction between the electrode-coated mediators and enzyme. As illustrated in Figure 1.3, the electrode can perform direct electron transfer without the need for highly toxic mediators by using organic conducting materials based on charge-transfer complexes. (Palmisano et al., 2002). As a result, implantable, needle-type devices for continuous in vivo blood glucose monitoring have been developed using third-generation glucose biosensors. These biosensors have better selectivity because there are no mediators present.

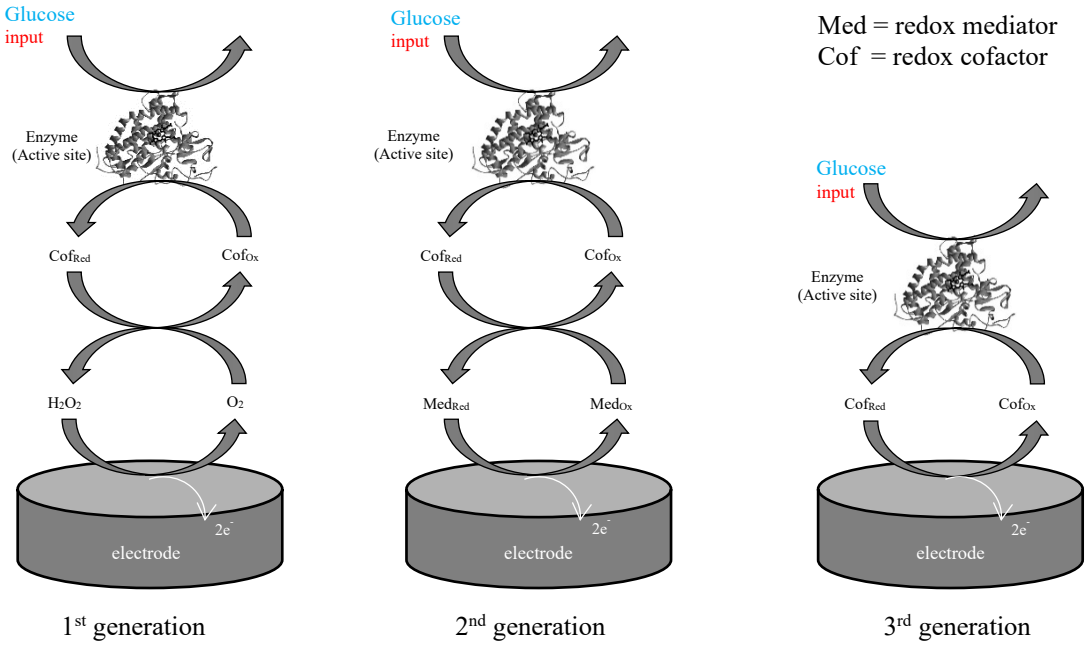

Figure 1. 3 Glucose biosensors (a) First-, (b) Second-, (c) Third generation. (designed by author)

Due to their high sensitivity and reproducibility, electrochemical methods have been used in most glucose biosensors created in recent decades. On the other hand, the expensive enzyme itself is a significant drawback of the enzymatic biosensor. In addition, GOD can be damaged by some chemical substances and detergents or changes in its optimal environment for instance, temperatures above 40 °C, pH below 2, or above 8. Indeed, those GOD-based glucose sensors are always vulnerable to deactivation due to chemical deformation and possible thermal changes during fabrication, storage, or even while using (Widi et al., 2017). Because an operational potential was necessary for the amperometric measurement in enzymatic-based sensors, they do not work well with passive sensors.

Therefore, synthetic receptors are presented with the potential of reducing and/or removing limitations mentioned before; accordingly, molecular imprinting is proposed to develop such synthetic receptors (Bakhtiar et al., 2019). Molecular Imprinting Technology (MIT) forms artificial receptors in addition to prearranged selectivity in relation to a specifically targeted molecule that is practical in various fields(Ding et al., 2020). Polyakov was the first to present the MIT in early 1930 and described how the type of template could impact selectivity. In order to explain how the immune system functions, Pauling proposed the concept of MI in the 1940s. This

theory is based on the self-assembly of protein antibodies with an antigen that serves as a target molecule (Ma et al., 2018).

Molecular imprinted technique offers the advantage of overcoming the limitations of enzyme-based sensors hence developing imprinting sensors with high selectivity by polymerizing a prepolymer in the existence of the target (Schirhagl, 2014). This method has been applied practically to combine materials with molecular selectivity in past decades (Figueiredo et al., 2016). As a result of advancements in imprinting technology, these polymeric matrices can recognize molecular components and unique recognition sites formulated on size, shape, and combination to the template compound and identify binding sites that simulate the biological ones (Pan et al., 2018; Peeters et al., 2016). Thus, Molecular imprinted polymers (MIPs) attract lots of attention in sensor fabrication due to their excellent selectivity. Indeed, various sensors based on a combination of MIPs were developed in a wide range of applications (Dehdashtian & Hashemi, 2019; Mirmohseni et al., 2014a). By integrating functional groups in the polymer, sensitivity and signal-to-noise ratio are improved.

I. Brief introduction of MIP

Molecular imprinting technology is a proper artificial method used today to produce robust molecular recognition materials that can imitate natural recognition entities, such as antibodies and organic receptors. (Poma et al., 2010)

In recent years, molecular imprinting has been one of the methods used to create materials with recognition ability comparable to natural systems. The design of synthetic materials that mimic the natural recognition processes has become an important and active area of research. MIT is regarded as a flexible and promising method that can identify biological and chemical molecules such as proteins and amino acids (Scorrano et al., 2011), nucleotide derivatives (Longo & Vasapollo, 2008a), pollutants (Pichon & Chapuis-Hugon, 2008), drugs, and food (Baggiani et al., 2007; Puoci et al., 2007) , and others. The following application areas are also covered: separation and purification (Haginaka, 2008; Lasáková & Jandera, 2009), chemical sensors (W. Li & Li, 2007), catalysis (Puoci et al., 2008), drug delivery (Ge & Turner, 2009), and biological antibodies and receptors (Longo & Vasapollo, 2008b).

An analyte (template) and a functional monomer come together to form a complex, which is the foundation of MIT. A three-dimensional polymer network (Ramström & Mosbach, 1999) is created when a cross-linking agent is in significant quantity. Following polymerization, the template is eliminated from the polymer, leaving behind particular recognition sites that are similar to the template molecule in terms of size, shape, and chemical functionality (Figure 1.4). Thus, the resulting polymer only recognizes and binds the template molecules. The intermolecular interactions between the template molecule and functional groups present in the polymer matrix, such as hydrogen bonds, dipole-dipole interactions, and ionic interactions, are typically what drives the molecular recognition phenomenon.

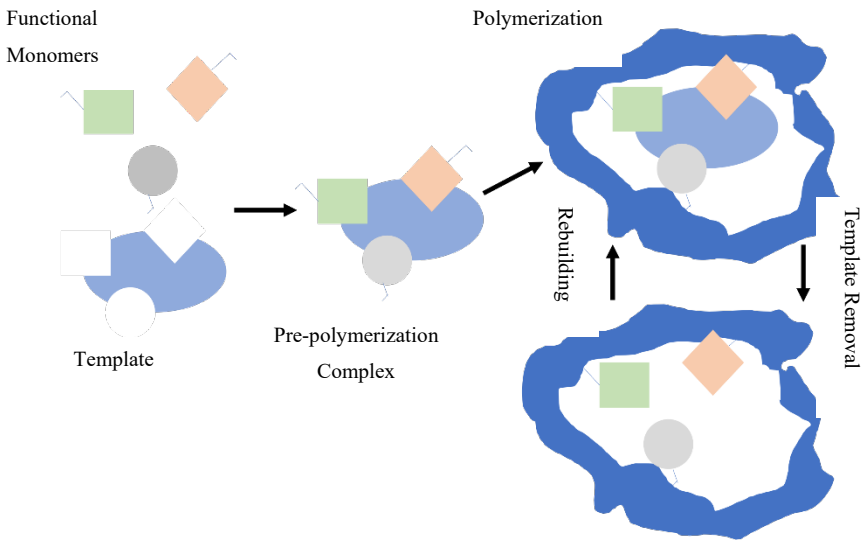

Figure 1. 4 Molecular imprinting schematic illustration (designed by author)

High selectivity and affinity for the target molecule used in the imprinting process are the main benefits of molecularly imprinted polymers (MIPs). Imprinted polymers outperform biological systems like proteins and nucleic acids in terms of physical robustness, strength, resistance to high temperatures and pressures, and inertness to acids, bases, metal ions, and organic solvents. Furthermore, they can be produced more cheaply, and the polymers can retain their recognition ability for a long time at room temperature thanks to their very long storage lives.

According to what is previously stated, molecular imprinting is a method for creating highly cross-linked polymers that can recognize specific molecules. Figure 1.4 illustrates the basic idea: a monomer will polymerize in the presence of a target molecule (template) that is incorporated into the polymer matrix. The process starts with a porogenic solvent solution of the

template, initiator, cross-linking agent, and functional monomer. Since stable template-monomer complex formation is necessary for effective molecular recognition, functional monomers are chosen to co-operate with the template molecule. By copolymerizing with cross-linking monomers, they are fixed in their spatial positions around the template. The final product is a microporous matrix with microcavities that complements the template's three-dimensional structure. Therefore, binding sites that are complementary in shape to the template are left behind after the template molecules are removed from the polymer by washing with solvent. The way in which monomer and template interact during polymerization is traditionally used to categorize molecular imprinting. As a result, the final polymer only recognizes and binds the template molecules. Depending on the interactions created during the polymerization process, the binding sites exhibit a variety of characteristics.

1.2 Objective

This project's primary goal is to design an RF sensing platform for passive wireless biosensors. A non-enzymatic RF glucose sensor will be developed as a proof-of-concept for the sensing platform. To be able to measure the glucose concentration, a synthetic bioreceptor will be developed. This synthetic bioreceptor will change the resonant frequency of an RF resonator. This work focuses on the design of Film Bulk Acoustic Resonator and Microstrip line based (open-Stub) Resonator, following which the creation of a sensor by making use of the above resonator. The other objective of this thesis was to develop a synthetic bioreceptor to measure the glucose concentration.

To accomplish the goal, the following objectives have been established:

1. Developing a synthetic bioreceptor to estimate glucose concentration. This project aims to utilize molecularly imprinted polymers (MIP) as glucose-selective receptors.
2. Designing and fabricating Film Bulk Acoustic Resonator (FBAR), acquiring the knowledge of thin film piezo electric’s structural and crystallographic characterization.

3. Utilizing the microwave-based sensor and deploying the manufactured synthetic receptor on the sensor to monitor and differentiate the impact of various glucose concentrations.

We aimed to propose a novel, simple, inexpensive, non-enzymatic, and sensitive characterization method by introducing a microfluidic integrated MIP-coated micro-wave biosensor capable of quantifying glucose concentration.

The structure of this thesis is as follows. The introduction, found in Chapter 1, explains the work's motivation and justification. The fundamental principles of sensors' operation and current technologies are discussed in Chapter 2. Chapter 3 discusses the various ways that molecularly imprinted polymers are made in this work. The in-house fabrication process used to fabricate the MIP precisely and accurately is described in detail in this chapter. In order to confirm that the bioreceptor is operating following the intended parameters, the manufactured MIP will then be put through various functional verification tests. The development of the FBAR simulation, fabrication technology, and characterization techniques are covered in Chapter 4. The application and integration goals could be achieved thanks to the first component of this work. Aluminum nitride (AlN) is deposited using RF spotting technology. Another success in this regard is the knowledge of AlN's structural and crystallographic characterization that has been acquired. The Stub resonator sensor's integration with the bioreceptor created in Chapter 3 is the subject of Chapter 5, which is devoted to its simulation, fabrication, and functional verification. This chapter describes the sensor's capacity to identify various glucose concentrations. The work presented is concluded and summarized in Chapter 6. The thesis and explores concepts for further research.

Chapter 2: Sensor Principals

Progress in science and technology has allowed us to reasonably consider the detection and real-time monitoring of outside physical quantities as well as chemical or biological substances in gaseous or liquid environments, including biological fluids. The development of sensors with high sensitivity, stability, low limit of detection (LLD), scalability, reproducibility, sufficient discrimination between chemical or biological types, despite impressive technological advancements, maintaining energy independence, straightforward results exploitation, and a reasonable cost level remains a significant challenge (Rai et al., 2017).

2.1 Transducer elements

Numerous well-known resonance phenomena in electronics, optics, and acoustics are either the result of standing waves or result from scattering waves. As a result, resonators can be created in a variety of ways based on interventions between electromagnetic, electronic, optical, and acoustic waves, as well as their coupling. Resonance can be energy-free in sensors, enabling high signal-to-noise ratio measurements and serving as a selective filter to eliminate the parts of the signal that is not inefficient. There have been reports of resonating transducers based on various wave frequencies, including microwaves (Hallil et al., 2019), radiofrequency (Pasquier et al., 2019), and acoustic waves. The inherent passiveness, generality, portability, and suitability of these technologies for high-frequency operation make them potentially wirelessly measurement. Indeed, the use of additive or semiconductor technologies in their production enables mass production at cost-effective prices.

This section advises focusing on the common and promising passive resonant sensors, which have revolutionized measurements in real-time. A thorough review of the principles of remote sensing and acoustic, and microwave transducers is covered in this section.

I. Resonant sensor principles

- Bulk wave acoustic platforms

When molecules and other nearby objects move in a mechanical wave motion, they generate a frequency shift that electromechanical devices use to function. The surrounding objects' inertial mass influences this frequency shift. Thin films, microcantilevers, and transducers based on the acoustic vibrational modes of crystals are some of the most sensitive transducers. The typical high frequency ones rely on bulk acoustic waves (BAW), surface acoustic waves (SAW), or plate waves. These devices convert electrical energy and mechanical wave bilaterally using the direct and reverse piezoelectric effects. The primary sensor output signal, the acoustic wave propagation velocity, is affected by various factors, including changes in the mass that is mechanically attached to the device surface.

The quartz crystal microbalance (QCM), which is a component of BAW devices and typically operates at a few MHz or tens of MHz, is the earliest type of acoustic detection device. It has been extensively used for the detection of target compounds as well as nearby physical variables like temperature and pressure. Studies of Lamb waves and shear horizontal acoustic plate modes (SH-APM) that propagate in piezoelectric thin film devices are frequently conducted in the frequency range of 2-200 MHz (Ballantine et al., 1997). However, unreasonably thin plates would be necessary for good surface sensitivity and mode separation. Thick films of aluminum nitride (AlN), scandium-doped aluminum nitride (Sc-AlN), or are the main components of thin film bulk acoustic resonators (TFBAR or FBAR), a recent development in the family of BAW devices. These piezoelectric films are either mounted stably on a supporting structure with an integrated Bragg acoustic mirror (SMR) or on a membrane cavity, as shown in Figure 1.4. FBARs can function in a thickness shear or longitudinal mode, with the latter preferred for a liquid operation to reduce energy losses. From sub-GHz to tens of GHz, the FBARs' operating frequencies range (Link et al., 2007; Y. Zhang et al., 2018).

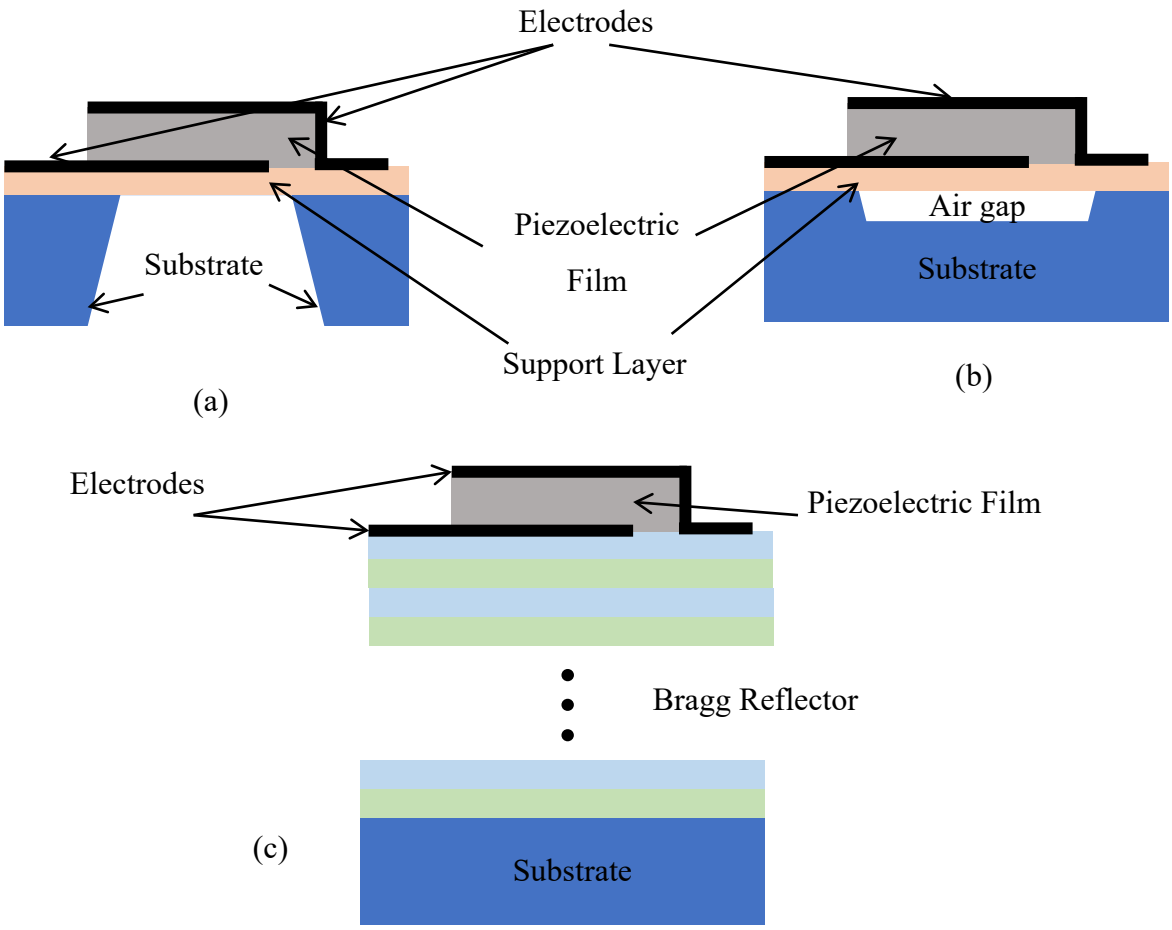

Figure 2. 1 The most common BAW resonator configurations are (a) membrane type, FBAR, (b) air gap type, FBAR, and (c) solidly mounted resonators (SMR) type.(Pang et al., 2017)

In general, there are a variety of factors that can influence the acoustic wave resonance frequency, and each one could result in a sensor response. Equation (1) shows how relative frequency varies in relation to changes in several factors such as electrical field (E), mechanical stress (σ), temperature (T), mass (m) and environmental.

$$\frac{\Delta f}{f_0} \cong \frac{1}{f_0}\left(\frac{\partial f}{\partial m}\Delta m + \frac{\partial f}{\partial E}\Delta E + \frac{\partial f}{\partial \sigma}\Delta \sigma + \frac{\partial f}{\partial T}\Delta T + \frac{\partial f}{\partial envi}\Delta envi\right) \quad (1)$$

Acoustic wave devices' sensitivity is determined by the partial frequency derivation from a given perturbation. It generally depends on the investigated mode's dispersion curve behavior under perturbation, the ratio of the waveguide or resonator's perturbed to unperturbed volume and the operation frequency. The most understandable acoustic wave sensor principle is the mass effect. The proper mode should be chosen based on the sensitivity of the dispersion curves,

followed by an increase in operation frequency, and then the resonator mass reference should be decreased to get it as close as possible to the equivalent loaded mass. The literature has reported several cavity resonators designs with high Q factors over the past ten years, demonstrating the full potential of this new technology line (Cicek et al., 2019; Moutaouekkil et al., 2019; Wang et al., 2016; Yankin et al., 2014).

- Electromagnetic Radio Frequency (RF) platforms

A new biosensing method uses microwave frequencies to study the electrical parameters of biological samples. The purpose of passive electromagnetic RF resonating sensors is to detect, assess, or continuously record changes in the material of the test (MUT). These sensors operate in the hundreds of kHz to the THz frequency range, utilizing an electromagnetic field as their foundation. Microwave biosensors have become popular among researchers, and electromagnetic waves have been employed to differentiate biological materials relying on detecting dielectric properties due to benefits such as being minimally invasive and cost-effective for many years. Microwave biosensors also offer high sensitivity and real-time monitoring of biological materials (Mehrotra et al., 2019).

The MUT's dielectric properties have an impact on how electromagnetic fields propagate. The complex permittivity models of these characteristics ε^* as shown in equation (2):

$$\varepsilon^* = \varepsilon' - j\varepsilon'' \tag{2}$$

Where the image part ε'' denotes the conduction and displacement currents induced within the matter, as well as the dielectric losses, and $\varepsilon'$is associated with the polarizability of the material. The resonance of the sensor interacting with the MUT is thus significantly affected by changes to the MUT's dielectric properties caused by changes to its structural, physical, or chemical characteristics. In general, equation 3 can be used to define the sensor's sensitivity S to changes in the dielectric.

$$S = \frac{\Delta f}{f_0 |\Delta \varepsilon^*|} \tag{3}$$

where, in comparison to an unloaded sensor or a sensor loaded with reference material, the induced resonance frequency shift is represented by Δf and Dielectric changes are indicated by the symbol $|\Delta\varepsilon^*|$. The MUT investigation's preferred scope will influence the operating frequency choice (Engineering of Micro/Nano Biosystems | INSIS, 2020). The lower RF spectrum (hundreds of kHz to tens of GHz) has seen extensive use of passive inductor-capacitor (LC) resonant sensors since the 1960s because they provide flexible, wireless sensing solutions, sensitive, and easy-to-design (Q. A. Huang et al., 2016) . Because of its resonance frequency f and quality factor Q, the LC circuit functions as a resonant energy storage component, as shown in equation (4):

$$f = \frac{1}{2\pi\sqrt{LC}} \text{ and } Q = \frac{1}{R}\sqrt{\frac{L}{C}} \quad (4)$$

The R, L, and/or C parameters, and consequently the resonance of the sensor, will change as a result of modifications to the MUT's dielectric properties brought on by structural, chemical, or physical changes, where the R indicates the resonator losses. The impedance of a monitoring coil placed a distance away from the LC sensor and inductively connected to it allows for the reading of these changes (Figure 1.5 a.). Because of this, passive LC sensors are especially well suited for low-invasive monitoring applications in harsh, sealed, or difficult-to-access environments. These applications greatly benefit from recent microfabrication technology advancements, enabling miniaturization, functionalization, flexibility, and minimally invasive sensing solutions.

The evaluation of a sample used as a waveguide or resonator charge's dielectric properties through direct measurement, as shown in Figure. 1.5.b. A fluid's or a solid's permittivity can be estimated (Velez et al., 2019). This type of measurement has been made easier for tasks requiring the detection of liquid media by incorporating a microfluidic chip. (Chuma et al., 2018). Metamaterial-based structures are shown in Figure 1.5.b. Specifically, because of the electromagnetic field's concentration, sensors of this kind now have improved sensitivity.

Over the past 20 years, a brand-new generation of microwave sensors has also emerged. The method of detection is indirect. based on observing the alteration in the conductivity and dielectric properties of an additional chemical substance immobilizing or interacting with the target chemical or biological species, Figure 1.5(c, d, and e) were developed. Low-cost manufacturing is typically made possible by microstrip and coplanar line-based geometries.

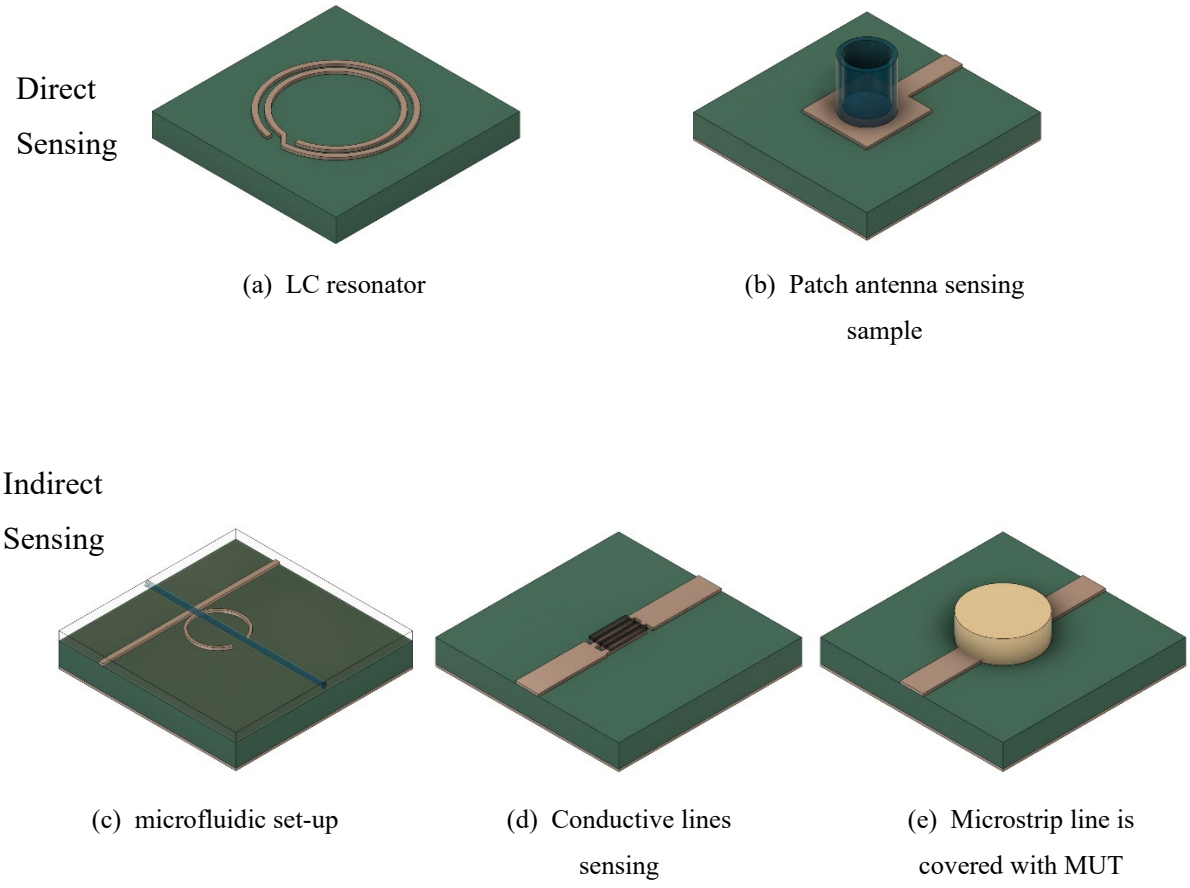

Figure 2. 2 Principle of a microwave sensor, both direct and indirect.

Three crucial issues in the field of sensor research can be solved by this kind of microwave transducer. To begin with, a variety of materials can be used to create them. They can operate at room temperature, which is number two. Thirdly, by directly relating sensor response to excitation frequencies, it is possible to better comprehend how to target molecules interact with microwave-sensitive materials. The dielectric properties are influenced by surface interactions between the sensitive material and its surroundings, such as adsorption (physisorption, chemisorption), Van der Waals and the covalent bond, or the dipole-dipole interactions. The final application dictates which sensitive material is selected (de Fonseca et al., 2015). It can either be locally deposited (Krudpun et al., 2019) or completely covered (Rossignol et al., 2013) by the resonant circuit.

2.2 State of Art

I. Acoustic biosensors

Mass-sensitive sensors are most commonly used in chemistry and biology, particularly in liquid and gas environments. As an example, resonant mass sensors were developed and utilized to detect various chemical and biological agents based on the microcantilever's vibration [Ref]. Although this sensor is proven to detect the mass attached to the microcantilever surface, its fragility and difficulty in packaging make it inappropriate for specific applications. Acoustic wave resonance sensors are widely investigated and utilized in further research and applications due to their high sensitivity, low-cost fabrication, and simple packaging.

A typical acoustic mass sensor was developed to study the change in the resonant frequency of an acoustic-wave resonator with respect to the various mass loaded on the resonator's surface (Voinova, 2009). The two most common acoustic mass sensors are classified as 1) Bulk Acustic Wave (BAW) and 2) Surface Acoustic Wave (SAW).

QCM is categorized in Bulk Acoustic Wave (BAW) device, which uses longitudinal waves, known as thickness-shear mode, to propagate in the bulk of the material. QCM includes a quartz disk that is sandwiched between two metal electrodes; At the same time, an electric field is applied to the electrodes, which causes an increase or decrease in the thickness of the quartz disk, depending on whether the area is parallel or perpendicular to the internal electrical polarization of the piezoelectric material. The quartz crystal's oscillation frequency in a mass sensor (QCM) relates to the total mass of the crystal substrate and the additional mass applied to the crystal's surface. Mass added to the sensor decreases the resonance frequency.

A combination of biologically sensitive elements with physical transducers was used in biosensors to detect the trace of biomarkers such as DNA (Auer et al., 2011; Nirschl et al., 2009) proteins (Kanno et al., 2000; Quan et al., 2011; Zhao et al., 2012), and cells (Ayala et al., 2009). In contrast, acoustic wave-based devices are less expensive without compromising their sensitivity. Bulk acoustic wave (BAW) resonators provide high sensitivity, real-time and label-free detection, and wireless capabilities (Voiculescu & Nordin, 2012). They have been extensively

used to detect mass (DeMiguel-Ramos et al., 2017; García-Gancedo et al., 2013; He et al., 2011; Nagaraju et al., 2014). pressure (Giangu et al., 2015)humidity (M. Zhang et al., 2015), and biomarkers (Chen et al. 2015b; Dickherber et al. 2008; Guo et al. 2015; Tukkiniemi et al. 2009; Weber et al. 2006; Wingqvist et al. 2008).

The most popular BAW-based sensor is the quartz crystal microbalance (QCM) that are commonly used for biosensing applications in both wet and dry environments (Fu et al., 2017) with typical resonant frequencies ranging between 5 to 20 MHz (Garcia-Gancedo et al. 2011a). Their ability to distinguish bio-substances in gas and liquid environments based on mass changes has been studied for decades, offering decent signal strength, excellent temperature stability, and sensitivity. QCMs have served as biosensors to detect DNA (Caruso et al. 1997; Steichen et al. 2009) and proteins (Corso et al. 2006; Kößlinger et al. 1992; Shons et al. 1972) since 1972 due to their inexpensive and label-free nature compared to other types of biosensors. However, one of the significant limitations of QCM-based biosensors is the large mass detection limit because of the low operating frequency and large base mass. In addition, the substrate is thick from 0.5 to 1 mm and has large surface areas of about 1 cm2. This limits their practical applications regarding sensitivity, scalability, and the possibility of miniaturization. Furthermore, integration with electronics components and microfluidic devices is challenging due to the bulk structure nature of QCMs, limiting their applications as biosensors (Arce et al. 2007; Kanazawa 1997; Marx 2003).

During the past decades, film bulk acoustic resonators (FBARs) were introduced as a member of the family of BAW-based devices and have been widely utilized for biological/medical analysis and diagnostics, such as cancer, cardiovascular disease, and hypertension (Fu et al. 2010; Hirsh 2006; Nirschl et al. 2010; Xu et al. 2012) due to the advantages such as ultra-high sensitivity, small size, simple operation and low fabrication cost (Krishnaswamy et al., 1990). Piezoelectric thin films are used in FBARs instead of bulk crystals in QCMs; hence, they have much higher resonant frequencies and smaller base mass, providing much higher sensitivity than QCMs. Furthermore, piezoelectric thin films can be grown on various substrates such as silicon, glass, and polymer films due to their good adherence. Therefore, they can be easily integrated with microfluidic devices for lab-on-a-chip applications (Garcia-Gancedo et al., 2010; García-Gancedo et al., 2011; Kim et al., 2012; Y. Zhang et al., 2013), and with complementary metal oxide semiconductor (CMOS) electronics for measurement control and signal acquisition and

processing. As previously stated, passive sensors can be used with vibration, making this technology one of the best options.

II. Radiofrequency biosensors

Radio-frequency/ Microwave spectroscopy (Hornyak et al., 2016; Rosen et al., 2002)is used to distinguish and characterize biomolecules in the frequency range up to 300 GHz. This biosensing method uses the different configurations of active and passive transmission networks and the scattering matrix elements as detection indicators. By measuring the resonant frequency shift and amplitude changes, useful information about the material under test can be obtained. Various biorecognition molecules, biochemical protocols, and architectures were presented. Some incorporated microwave transmission line resonators, while others used capacitive planar components. Some carried out time-consuming and complicated biochemical protocols to enhance the sensitivity, and a few used labels to detect a signal change.

Recently, several biosensors based on microwave transmission line networks integrated with microfluidic channels were reported in healthcare applications. They focused on detecting bio-analytes, biomarkers, single cells, biological tissues, and glucose concentration levels (Costanzo, 2017; García-Baños et al., 2006; Gudkov et al., 2015; Guha et al., 2017; Stuchly et al., 1982).

The primary focus of the RF biosensors developed recently is to characterize biomolecules utilizing resonators and coplanar waveguide structures. Resonators in RF/microwave are generally realized using microstrip technology, where they can be implemented in different shapes and sizes such as radial/open-end stub, ring, and coupled line. Electromagnetic waves have gained considerable interest as an investigation tool to analyze bio-analytes such as glucose levels. The following section provides a brief description and review of the most valuable research in this field.

III. Glucose RF biosensors

Various topologies, frequency ranges, and glucose concentrations have been proposed in the literature to study normal and diabetics glucose levels in human serum and often higher

unrealistic concentrations. Glucose sensors were mainly developed using planar technology. Microstrip lines and split ring resonators (SRR) are the most widely used structures for this purpose and attract interest due to their low cost, small size, and ease of fabrication. Some researchers proposed several configurations based on planar technology for resonant frequency (f_r-based) glucose sensors while others use the return loss (S_{11}) or insertion loss (S_{21}) as the sensing parameter. The principle of the sensors that use resonant frequency as the sensing parameter to measure glucose concentrations is the correlation between the resonant frequency and the changes in the relative permittivity (ε_r) (Shahri, Omidvar, Rehder, Serrano, et al., 2021).

A glucose biosensor based on distributed microelectromechanical systems (MEMS) transmission line (DMTL) was reported (L. Li & Uttamchandani, 2009). An acrylic fluidic channel is attached to the transmission line. Aqueous glucose solutions of different concentrations ranging from 0 to 347 mg/ml were tested to verify the performance of the proposed device by measuring the resonant frequency shift of S_{11} due to glucose presence up to 40 GHz.

Stub resonators have also been studied in the past decade, and a miniature double-stub resonant-based sensor was introduced to detect the glucose concentrations of two aqueous solutions positioned over the sensing area of each stub (Chretiennot et al., 2014). Glucose concentrations ranging from 15 to 80 mg/L were characterized. It was suggested that the microwave structure is capable of glucose analysis of multiple aqueous solutions.

Some use labels such as enzymes to enhance sensitivity. In this context, a single SRR configuration was proposed with an extended capacitive gap with an enzyme coating (Camli et al., 2016a, 2017). For this biosensor, the glucose oxidase (GOD) enzyme was incorporated for glucose sensing, and the shift in the resonant frequency of the transmitted signal was observed. A sensitivity of 0.174 MHz/(mg/dL) with different glucose solution concentrations was obtained.

A metamaterial microstrip line sensor composed of a modified Hilbert-shaped curve in the middle was proposed to detect glucose concentrations in water solutions ranging up to 250 mg/dL (Parsamyan et al., 2018). The test samples were put in a cylindrical container on top of the H-shaped resonator. The variation in the magnitude of the transmitted signal with respect to glucose concentrations was studied in the frequency range of 5.5-6.5 GHz. The biosensor provided a sensitivity of 9.8×10^{-2} dB / (mg /dl).

A microstrip line-based glucose sensor using the main field was also investigated (S. Y. Huang et al., 2019) . Two frequency ranges of 100–500 MHz and 1.4–1.9 GHz were studied to evaluate the sensor's functionality by measuring the magnitude of the reflected signal to characterize NaCl (0.9%) samples with a glucose concentration of 78 -5000 mg/dL. The sensor presented an average sensitivity of 1.8 × 10−3 dB / (mg /dl) in the frequency range between 1.4 GHz and 1.9 GHz, where the samples were injected in the block under the line through inlets and outlets.

A microwave-based microfluidic glucose biosensor composed of an open-ended microstrip transmission line with a complementary split-ring resonator (CSRR) was presented (Ebrahimi et al., 2020). A PDMS channel was placed on the CSRR where glucose samples ranging from 0–500 mg/dL flowed. The resonance frequency and return loss were considered sensing parameters in the 2.4–2.6 GHz frequency range. By interpreting the measured results on the Clarke grid, they concluded that this biosensor is a good candidate for distinguishing glucose concentrations at physiological levels.

In one of our experiments, a simple, sensitive, low-cost microwave sensor capable of conducting glucose concentration measurements without chemical bindings was developed (Shahri, Omidvar, Rehder, Serrano, et al., 2021). The sensing device used a microstrip transmission line to detect variations in the glucose component of the solutions placed in a microchamber under it. The shift in the absorption frequency of the device was measured in the frequency range between 4.8 GHz and 5.7 GHz using solutions with different glucose concentrations ranging from 100 mg/dL to 300 mg/dL. The experimental results showed a high sensitivity of 0.32 MHz/ (mg/ dL) for the glucose level in the physiological range.

However, certain limitations related to label-free biosensors are argued; for instance, the absence of enzymes or receptors to distinguish specific target biomolecules limits selectivity. Yet, the insufficient stability due to the nature of the enzymes is the main disadvantage of utilizing enzymes in monitoring glucose applications. MIPs are considered appropriate alternatives to enzymes because of their high stability (DOMB, 1996). Furthermore, MIPs can be synthesized for biomolecules for which no receptor or enzyme is available or are too expensive. In addition, the polymerization step is comparable with microfabrication used in sensor technology. MIPs have been developed for sugars, amino acid derivatives, drugs, solvents, and vapors (Hillberg et

al., 2005). MIPs are utilized in various sensing devices such as micro-balanced, mass-sensitive, and fluorescence-based, and also in electrochemical techniques such as surface plasmon resonance spectroscopy and chemical luminance(Opik et al., 2009).

The use of MIPs in separation is fast-growing, providing excellent opportunities in the chemical and pharmaceutical industries, including recombinant proteins and monoclonal antibodies (HJERTÉN et al., 1997). They have already been employed in protein separation (YE; CORMACK; MOSBACH, 2001), separating and purifying amino acids, DNA and RNA, peptides, hormones, and carbohydrates (Dai et al., 1997). MIPs are employed in stationary phases of chromatographic techniques such as HPLC, TLC, LEC, SFC, frontal chromatography, etc., to separate and determine various template molecules. MIP membranes have been utilized in ultrafiltration processes to separate different structurally related compounds (Piletsky et al., 2001).

Several attempts have been made to employ MIPs in pharmaceutical applications, and they have grown into a new subject in drug delivery due to their specifications, such as binding capacity and selectivity (Sellergren & Allender, 2005). Implementing MIPs in soft contact lenses is proven to prolong the permanence of timolol in the precorneal area, in contrast with conventional contact lenses and eye drops. Utilization of MIPs in controlling drug release provides promising results in tablets composed of propranolol imprinted beads for selective control release of the propranolol (Suedee et al., 2002) and also for Cyclodextrin, peptides, and protein imprinted polymers (Alvarez-Lorenzo & Concheiro, 2004).

Cell imprinted polymers in the biotechnology field could be used in the pharmacological analysis of drugs effects on individual cells rather than whole cell tissue (Sellergren, 2001) . MIP techniques were validated for preparing various essential compounds, including proteins, hormones, enzymes, and more complex structures such as DNA and carbohydrates, to be used as templates (DOMB, 1996). In short, the selective interaction of MIPs and biomolecules can be considered equivalent to the interaction of antibodies and antigens. Therefore, they are cheap, rapid, and stable alternatives to be used in biosensors.

Chapter 3: Molecularly Imprinted Polymer fabrication

The current study created a simple, low-cost, and accurate way to measure glucose. For constructing a RF-based sensor, a selective coating made of a glucose-imprinted polymer film was used. With the help of a continuous flow Quartz Crystal Microbalance (QCM) system and the sensor's analytical capabilities, glucose was determined. The following three methods were used in this project to obtain MIP, and the MIP obtained was tested on QCM to confirm the glucose selectivity. The experiments were conducted at the Chemical Institute of USP (University of São Paulo).

3.1 Thermal Polymerization

This method, a monomer is converted to a polymer using only thermal energy in a purely thermal polymerization. Numerous monomers and monomer pairs have been reported to initiate homo- and co-polymerization spontaneously (Moad et al., 1989). In this work, the first attempt used thermal polymerization to make the polymer faster, but the bulk polymerization made coating the sensor difficult, due to the difficulty of patterning and distributing the uniform layer.

The chemicals used in this experiment are listed below:

- Acrylic acid (AAc).
- Poly (methyl methacrylate) (PMMA).
- Ethylene glycol Di methacrylate (EGDMA).
- 2,2′-azo-bis-isobutyronitrile (AIBN)
- Dimethyl sulfoxide (DMSO).

In this research, all the chemicals utilized were analytical-reagent grade and acquired from Sigma Aldrich Co.

In this experiment, two polymers were made, the first of which is referred to as a molecularly imprinted polymer (MIP) and is a selective polymer with the capacity to bind target molecules,

and the second of which is referred to as a non-imprinted polymer (NIP) and exhibits no binding properties toward a target molecule. The preparation of MIP, and NIP and the sensor was executed as follows, and the steps are illustrated in Figure 3.1:

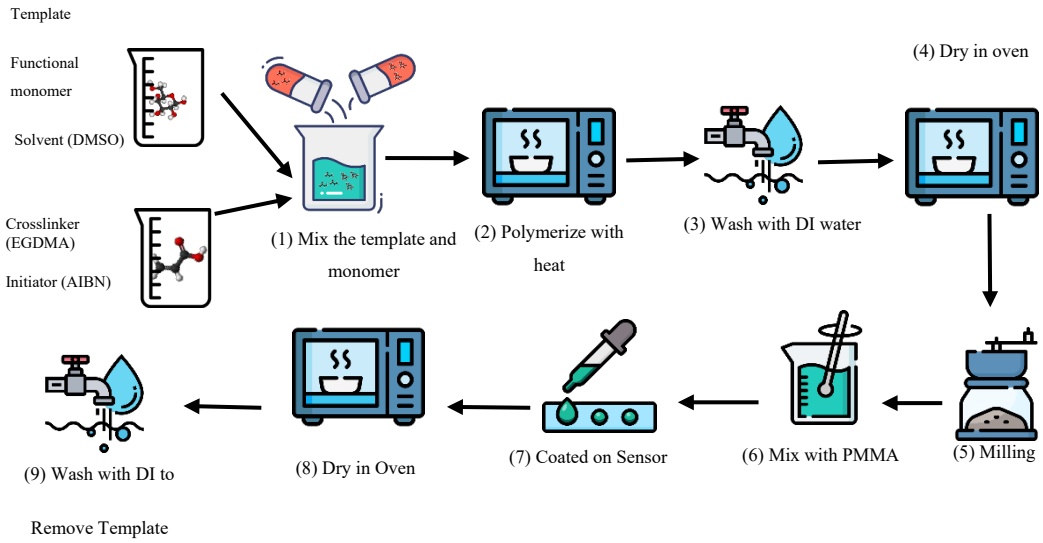

Figure 3. 1 Illustration of Thermal polymerization preparation.

(1) 1 mmol (69 µL) of AAc, called a functional monomer, and 0.25 mmol (0.045 g) of glucose, used as a template were dissolved in 5 mL DMSO and stirred for 1 hour. In another flask, 4.0 mmol (0.79 g) of EGDMA and 0.0050 g of ACPA were stirred for 1-hour and then mixed with the former solution. Nitrogen gas was bubbled for 15 min to remove dissolved oxygen.

(2) Polymerization was initiated by heating at 60 °C for 24 h.

(3) Bulk polymers were washed with water to remove any non-polymerized monomers and solvents.

(4) The MIP was dried by heating at 60°C for 12 h.

(5) Then milled with mortar and pestle to make a fine powder. The same procedure was repeated to prepare the non-imprinted polymer (NIP), however, without adding the template (glucose).

(6) The polymer powders were mixed with a solution of 5% PMMA (Adhesion) in Acetone. The ratio of PMMA to MIP (or NIP) powders was 50:50.

(7) In this step, the sensor was prepared by applying a certain amount (20 µl) of the mixed solution dropped on top of the gold electrode of the quartz crystal. Due to the rapid vaporization, a thin layer of MIP (or NIP) was formed on the sensor's surface.

(8) To evaporate the remaining solvent, the sensor was heated at 60 °C for 24 hours.

(9) The final step was to remove the template (glucose) from the MIP by washing the coated senor with DI water for 5 hours.

3.2 Electro polymerization

The electro polymerization technique was applied in the second attempt. A polymer is deposited on the surface of solid electrode material during electrochemical polymerization. A widely accepted mechanism for how it happens involves the oxidation of the monomer on the solid electrode material, which results in the creation of a cationic radical explained by (Saleh, 2021). A potentiostat/galvanostat AUTO LAB model PGSTAT128N was used for the electro-polymerization of o-Phenylenediamine (o-PD). The electrochemical cell used in a three-electrode configuration, using the gold electrode of the quartz resonator, a Pt wire, and an Ag/AgCl/KCl saturated electrode as working, counter, and reference electrodes, respectively. Figure 3.2 displays the electro-polymerization setup.

Following, Figure 3.3 illustrates the polymerization cycle, polymerization of o-PD was performed by cyclic voltammetry (20 scans) in the range 0.0-0.8 V (scan rate 50 mV/s) from a solution of o-PD 5 mM in acetate buffer (pH 5.2). For imprinted polymerizations, glucose was also added at a concentration of 20 mM. After the synthesis, the polymer film, still mounted inside the holder, was subjected to a washing procedure in triply distilled water, to remove the glucose possibly entrapped in the polymeric matrix.

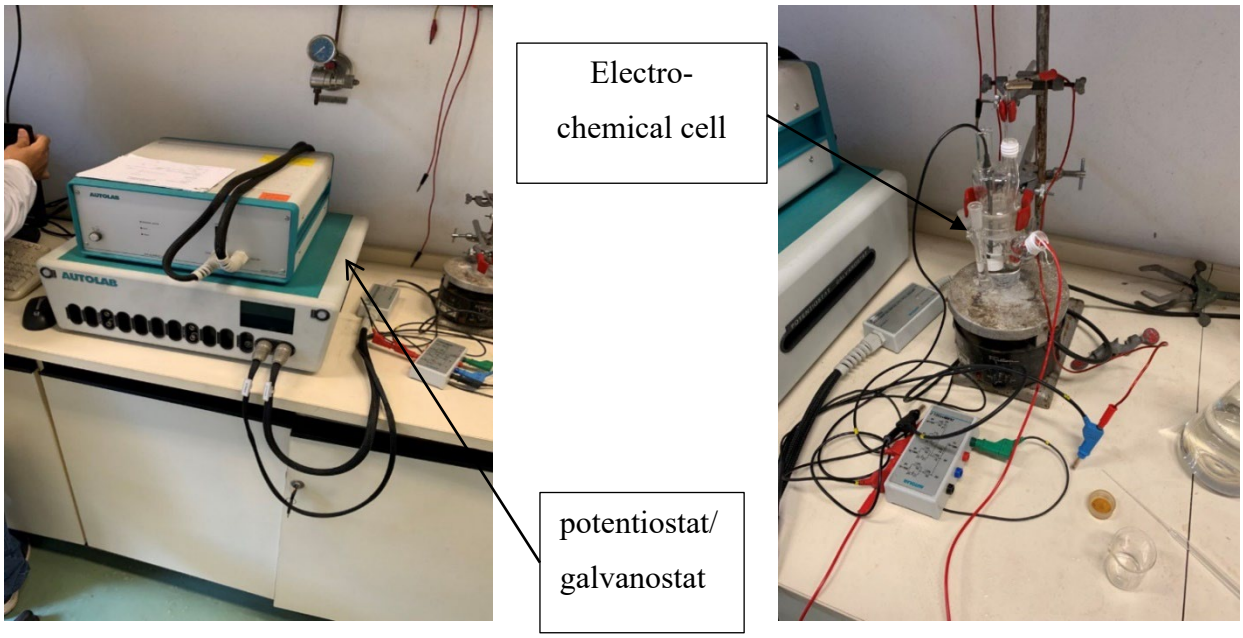

Figure 3. 2 Electro polymerization setup and electro-chemical cell

Figure 3. 3 Cyclic voltammetry (20 scans) in the range 0.0-0.8 V (scan rate 50 mV/s)

3.3 UV light Polymerization

Monomer polymerization occurs during the UV polymerization process in the presence of a photo initiator. The photo initiator absorbs UV light between 300 and 400 nm, which is the proper

wavelength range. As a result, it splits apart into radicals that start the polymerization of monomers with specific structures, as described in (Shao et al., 2014). The chemicals used in this project are listed below:

- Acrylic acid (AAc);
- Poly (methyl methacrylate) (PMMA);
- Ethylene glycol Di methacrylate (EGDMA);
- 4,4′-Azobis (4-cyanopentanoic acid) (ACPA);
- Dimethyl sulfoxide (DMSO);

All the chemicals used in this study were analytical-reagent grade and came from Sigma Aldrich Co.

Again, in this experiment, two polymers are created: the first, known as a molecularly imprinted polymer, is a selective polymer with the ability to bind target molecules, and the second, known as a non-imprinted polymer, has no binding properties toward a target molecule. The subsequent steps were followed to prepare MIP, NIP, and the sensor; they are shown in Figure 3.4:

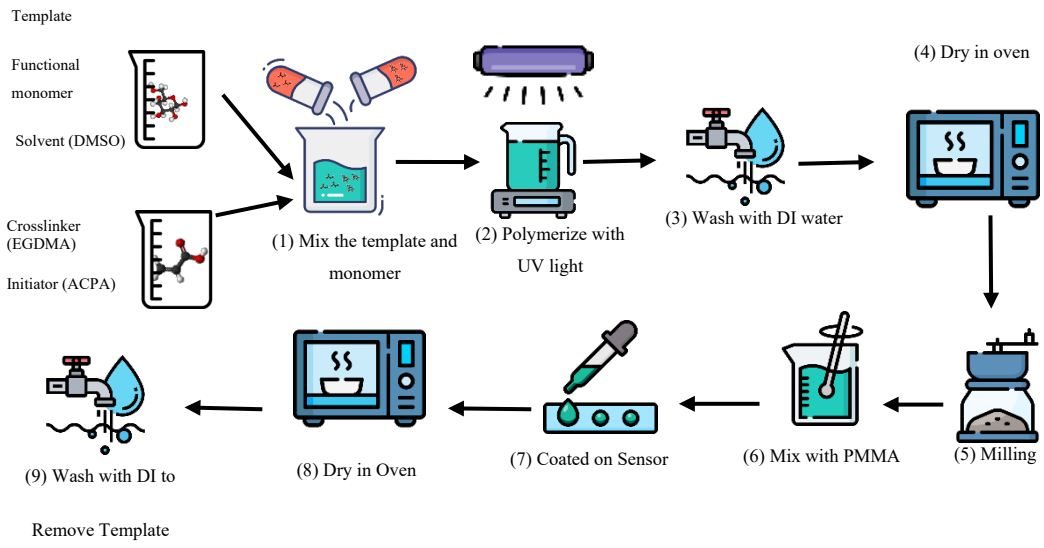

Figure 3. 4 Illustration of UV polymerization preparation.

(1)1 mmol (69 µL) of AAc, called a functional monomer, and 0.25 mmol (0.045 g) of glucose, used as a template were dissolved in 5 mL DMSO and stirred for 1 hour. In another flask,

4.0 mmol (0.79 g) of EGDMA and 0.0050 g of ACPA were stirred for 1-hour and then mixed with the former solution. Nitrogen gas was bubbled for 15 min to remove dissolved oxygen.

(2) UV light with wavelengths of 385 nm and 405 nm was used to start the polymerization process. which Figure 3.5 illustrates.

(3) Bulk polymers were washed with water as is shown in Figure 3.6 (a) to remove any non-polymerized monomers and solvents.

(4) Figure 3.6 (b) shows that the MIP was dried by heating at 60°C for 12 h and

(5) then milled with mortar and pestle to make a fine powder. The same procedure was repeated to prepare the non-imprinted polymer (NIP), however, without adding the template (glucose).

(6) The polymer powders were mixed with a solution of 5% PMMA (Adhesion) in Acetone. The ratio of PMMA to MIP (or NIP) powders was 50:50.

(7) A certain amount (20 μL) of the mixed solution was applied to the tip of the Stub resonator. Due to the rapid vaporization, a thin layer of MIP (or NIP) was formed on the sensor's surface.

(8) To evaporate the remaining solvent, the sensor was heated at 60 °C for 24 hours.

(9) The final step was to remove the template (glucose) from the MIP by washing the coated senor with DI water for 5 hours.

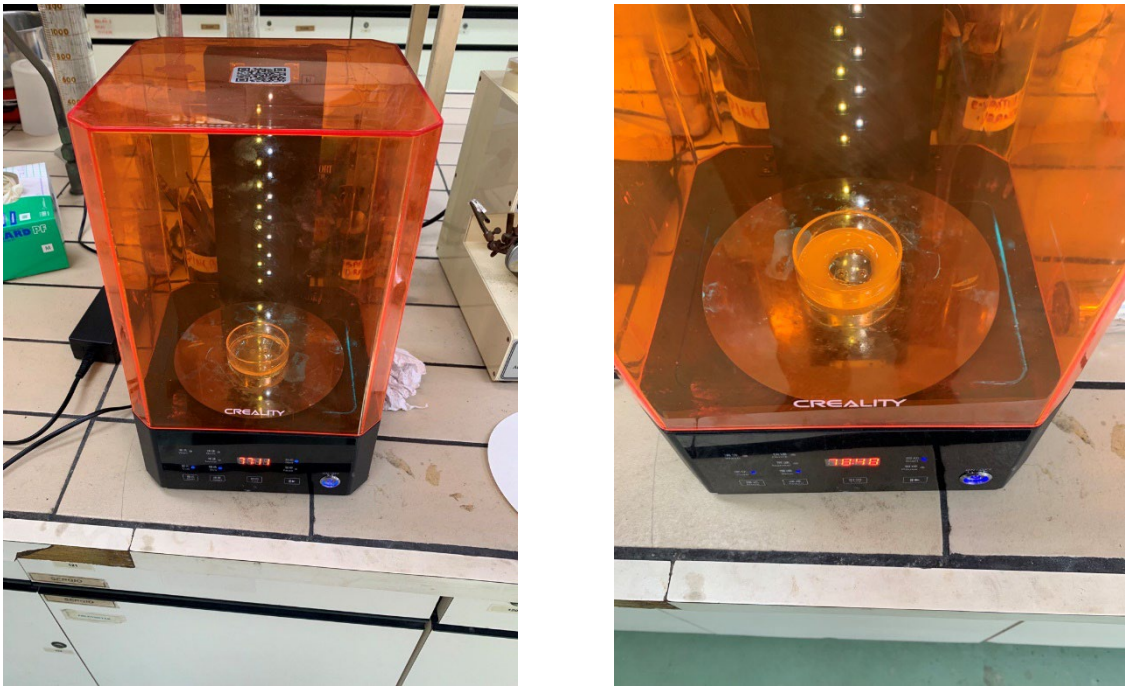

Figure 3. 5 Polymerization initiated by apply UV light

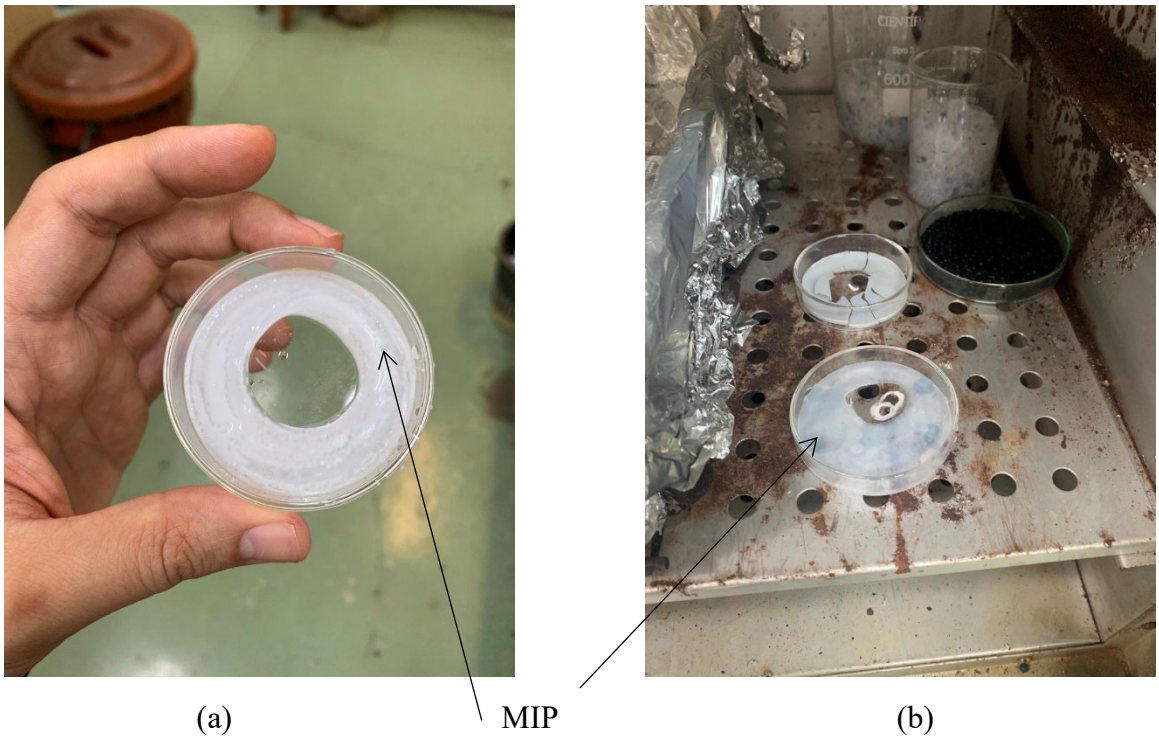

Figure 3. 6 (a) Wash the MIP with DI water to remove the solvent, (b) Dry the MIP in oven for 24 hrs.

We dried the polymer for 24 hours to mill it and achieve fine power, and then we tried to weigh the polymer before and after. This process was used twice, and neither time did the weight differ significantly from the first.

(a) (b)

Figure 3. 7 (a) weight before drying in oven, (b) weight after drying in oven for 24 hrs. in 60 ℃.

3.4 MIP validation with QCM technique

The Quartz Crystal Microbalance (QCM) is an incredibly sensitive mass balance that can detect changes in mass per unit area at the nano- to microgram level. A quartz disc, shown in figure 3.8, is the heart of the technology. Applying the proper voltage, typically through metal electrodes, quartz, a piezoelectric material, can oscillate at a specific frequency. The addition or removal of small amounts of mass from the electrode surface can change the oscillation frequency. Real-time monitoring of this change in frequency can provide important information about molecular interactions or reactions, such as film growth, oxidation, corrosion/decay, etc.

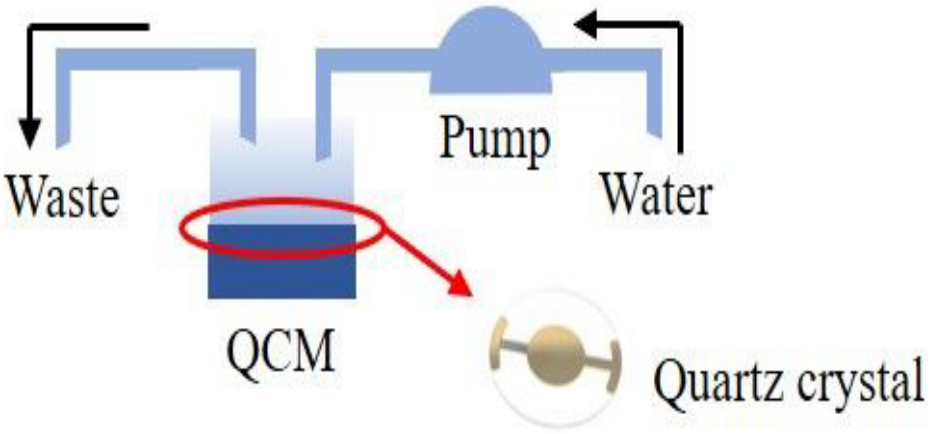

Figure 3. 8 QCM flow system

In this experiment, the MIP that is produced in previous section coated on the surface of quartz disc. The glucose concentrations in a series of two water solutions ranged from 100 mg/dL to 200 mg/dL. After the water glucose solutions had been allowed to reach anomeric equilibrium for roughly 12 hours, the experiment was carried out. In each procedure, data were gathered while the solution flowed continuously at a rate of 5 mL/min. DI water was pumped into the channel to wash it and flush absorbed glucose from the MIP after each measurement. Following pumping, the solution's oscillation frequency decreased and changed to a frequency of approximately 60 Hz, twice the initial concentration in the 200 mg/dL glucose solution. As a result, as shown in Figure

3.9, the oscillation frequency increases as the solution passes through the quartz crystal that has been coated with MIP, and it decreases as the solution passes through the quartz crystal that has been coated with 100 mg/dL of MIP around 30 Hz. This experiment demonstrated the flawless operation of the manufactured MIP.

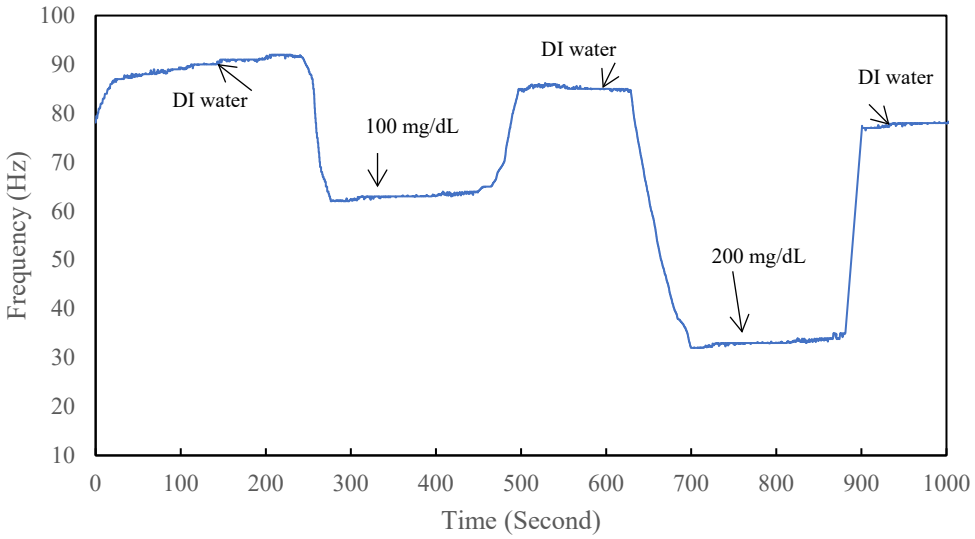

Figure 3. 9 Frequency changes of MIP-coated quartz crystal

Chapter 4: FBAR simulation and fabrication

In today's microsystems technology, the piezoelectric effect is used in various ways. Piezoelectric materials are utilized to create sensors and actuators. The direct piezoelectric effect and the indirect piezoelectric effect are distinguished. Pressure sensors and energy harvesting are two potential uses for the direct piezoelectric effect, which allows a voltage to be tapped when a force is applied to a material. The indirect piezoelectric effect involves applying a voltage that causes a material to deform, as in oscillating crystals.

Thin-film technology frequently uses aluminum nitride (AlN) as a piezoelectric material. For instance, it can be used at higher working temperatures than zinc oxide and presents a lower risk of contamination than lead zirconate titanate. Aluminum nitride is a unique material with special properties, including high piezoelectric constants, electromechanical coupling coefficient, degree of hardness, acoustic speed, and dielectric constant. AlN demonstrates piezoelectric characteristics in its wurtzite structure (Galsin, 2019). Many processes, such as physical or chemical vapor deposition, can deposit this hexagonal pattern as a thin film on a substrate.

Two steps are involved in the fabrication of the sensor in this work. The sensor design and fabrication come after the AlN is first developed with the desired orientation. Prior to beginning the fabrication process, the FBAR sensor was simulated using COMSOL Multiphysics, which was then used to optimize the desired AlN thickness.

4.1 FBAR Simulation

Narrowband resonators for radio-frequency applications can be made using bulk acoustic waves (BAW). Their main advantage over conventional electromagnetic resonators is that they can be made smaller because they can be made to have an acoustic wavelength that is shorter than the electromagnetic wavelength. The resonator structure might have a lot of spurious modes with very close spacing in addition to the desired bulk acoustic mode. Maximizing the main component's crystallization quality while minimizing the impact of spurious modes is typically the

design objective. The eigenfrequency and frequency-response analyses used in this section are used to model thin-film BAW resonators in 2D.

Figure 4.1 illustrates the resonator's geometry. The topmost layer of the resonator is an electrode made of molybdenum. Silicon, shown in Figure 4.1 with gray color, is utilized as the bottom layer of the resonator. The ground electrode is made up of a layer of molybdenum placed on top of the substrate layer, electrodes are demonstrated with dark blue in figure below. The active piezoelectric layer, which is made of aluminum nitride (AlN) which has shown with yellow color, is sandwiched between two molybdenum layers. Here, the geometry is the same as in Makkonen's research.(Makkonen et al., 2001)

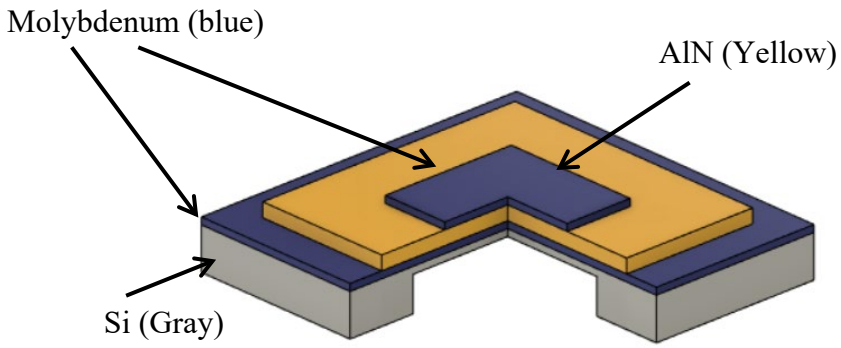

Figure 4. 1 Arbitrarily scaled geometry of a thin film BAW resonator

The top electrode's dimensions are 200 x 200 µm, forming the BAW resonator's active area. After etching a large portion of the silicon layer, the thickness of the silicon layer in the center is 7 µm, 300 µm is the width of the silicone's thinnest layer, and the thickness of the two molybdenum electrodes is 200 nm. The thickness of the piezoelectric layer defines the resonance frequency of FBAR in this project, considered 700 nm. The material properties used in this simulation were obtained from the MEMS module material library of the COMSOL Multiphysics software.

The two sides of the resonator are effectively lengthened by the Perfectly Matched Layer (PML) domains being used, has shown in Figure 4.2, which also simulates the effect of elastic wave propagation and absorption in the surrounding areas.

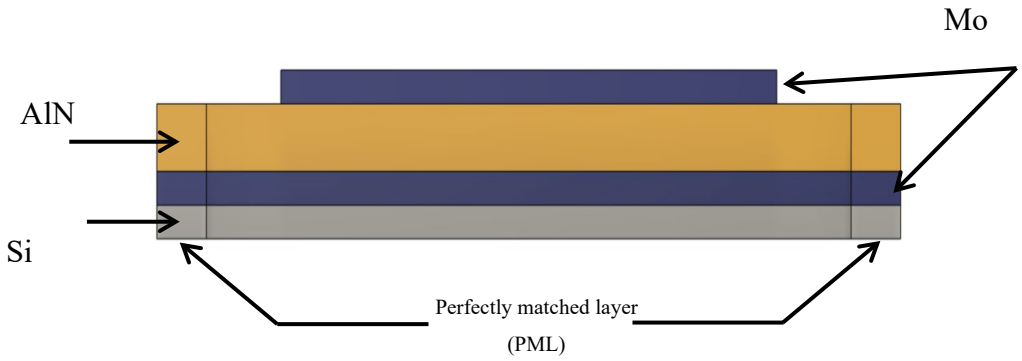

Figure 4. 2 The 2D geometry (not drawn to scale) used in the simulation.

In this simulation, COMSOL Multiphysics only solves the structural equation in the other layers, leaving the piezoelectric layer to solve both the structural and electrical equations. Figure 4.3 illustrates the structure's lowest BAW mode, which happens at 2.05 GHz. The eigenfrequency analysis results were used to create this plot. The primary longitudinal thickness mode is shown in this figure. Only for the purpose of visualizing the mode shape, the plot display scaled deformation. It should be noted that COMSOL Multiphysics computes complex valued eigenfrequencies, with the imaginary part providing a measure of the damping resulting from structural loss, polarization loss, and anchor loss.

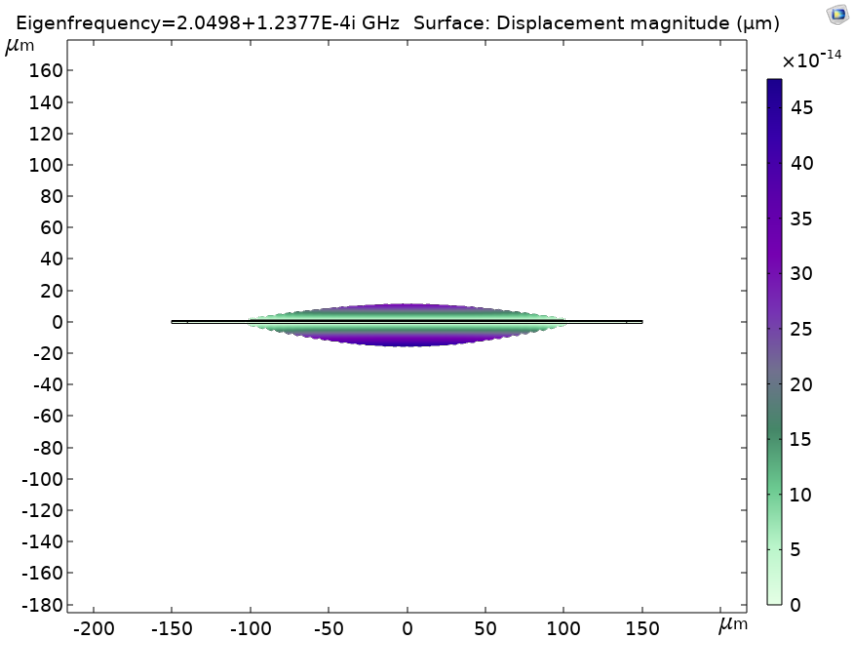

Figure 4. 3 The lowest bulk acoustic mode of the resonator identified from the solutions of the eigenfrequency analysis.

When the aluminum nitride layer is excited with 1 volt (zero-to-peak voltage) at 2.05 GHz, Figure 4.4 represents the resonator's deformation as determined by a frequency response analysis. The maximum deflection is approximately 6 nm.

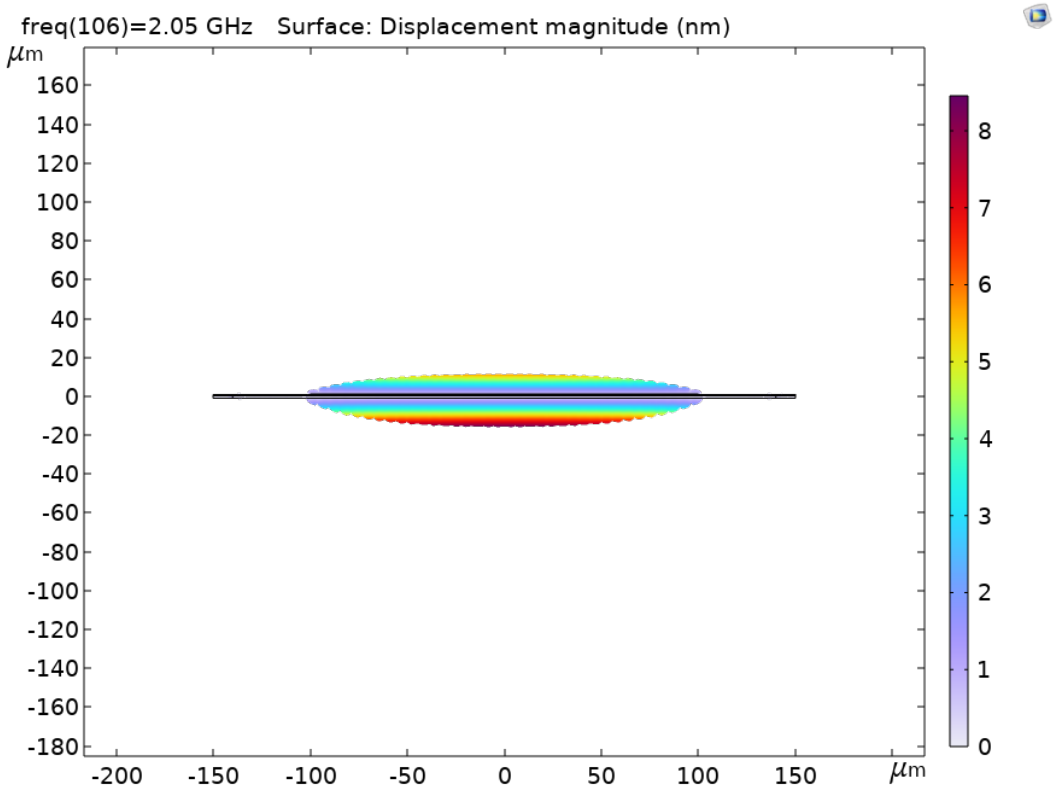

Figure 4. 4 The lowest bulk acoustic mode of the resonator identified from the solutions of the frequency domain analysis

The admittance is the proportion of the voltage across the piezoelectric material to the total current flowing through it. The admittance is automatically determined by the Terminal boundary condition in COMSOL Multiphysics, which is used to specify the voltage on the piezoelectric material.

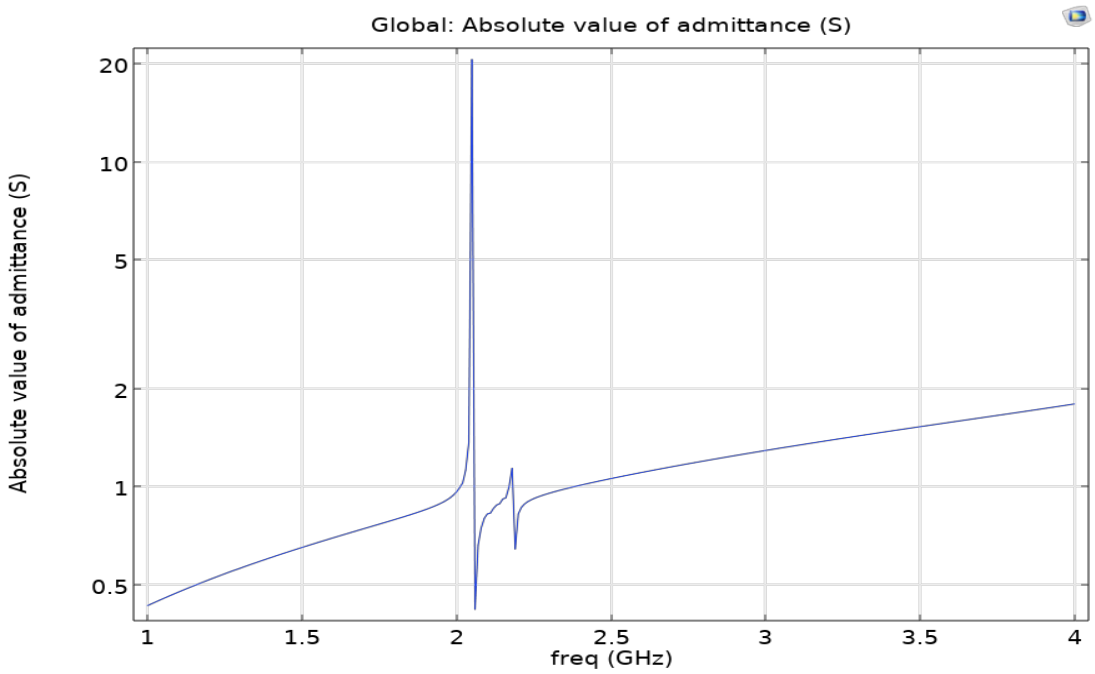

Figure 4. 5 Absolute value of the admittance vs. frequency

This quantity for a lossy material has a complex value. Usually, the imaginary part represents the displacement current, and the real part represents the conduction current and other losses in the structure. The absolute value of admittance is shown in Figure 4.5 as a function of frequency.

The quantity factor, also known as the Q-factor, describes how many cycles (at the specified frequency) it takes for the system's total energy to fall by a factor of $e^{2\pi}$. COMSOL Multiphysics also performs an automatic calculation of this. This frequency-response analysis value agrees with the Q-factor calculated from the eigenfrequency analysis. The eigenfrequency analysis indicates that the Q-factor at 2.05 GHz is 1845.

4.2 Sensor Fabrication

The piezoelectric thin film is the heart of a BAW resonator. Despite the fact that there are numerous piezoelectric materials such as ZnO, AlN, or less frequently PZT are the widely used ones. AlN is most frequently chosen for BAW resonators and sensors, especially if the integration above IC is anticipated due to its best balance of performance, manufacturability, and reliability. AlN crystallizes as a wurtzite hexagonal structure, as seen in Figure 4.8.

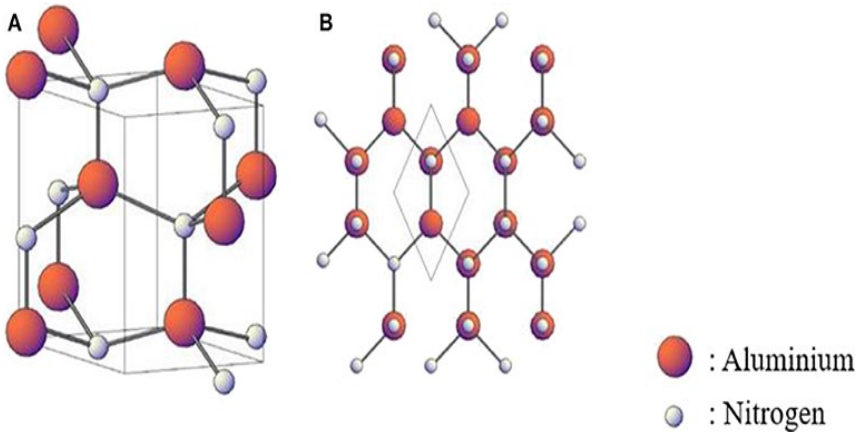

Figure 4. 6 Diagrams illustrating the assembly of (A) 3-D and (B) 2-D aluminum nitride (AlN) crystals. (Alsaad et al., 2020)

In piezoelectric applications, where the orientation of (002) is preferred to obtain a high piezoelectric coefficient, the crystal orientation of aluminum nitride (AlN) thin film presents a challenge. From the crystal's point, the (002) orientation extends the length of the crystal as shown in Figure 4.9(Xu et al., 2001).

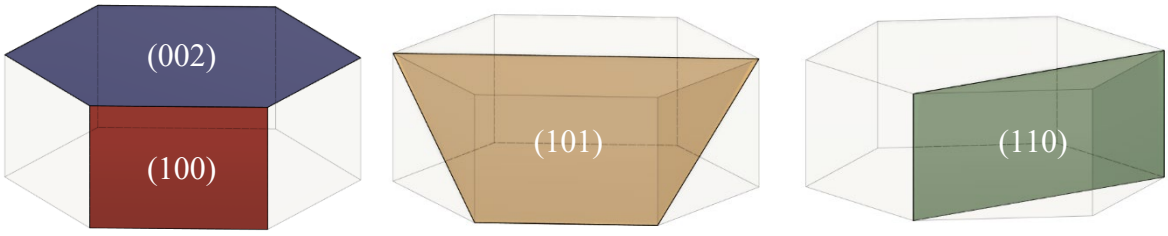

Figure 4. 7 Crystallographic planes' geometries for the hexagonal AlN lattices (100), (002), (101), and (110).

As can be seen in figure 4.10, X-ray diffraction was used to characterize the deposited film. Table 4.1 details how each orientation occurs at which angle.

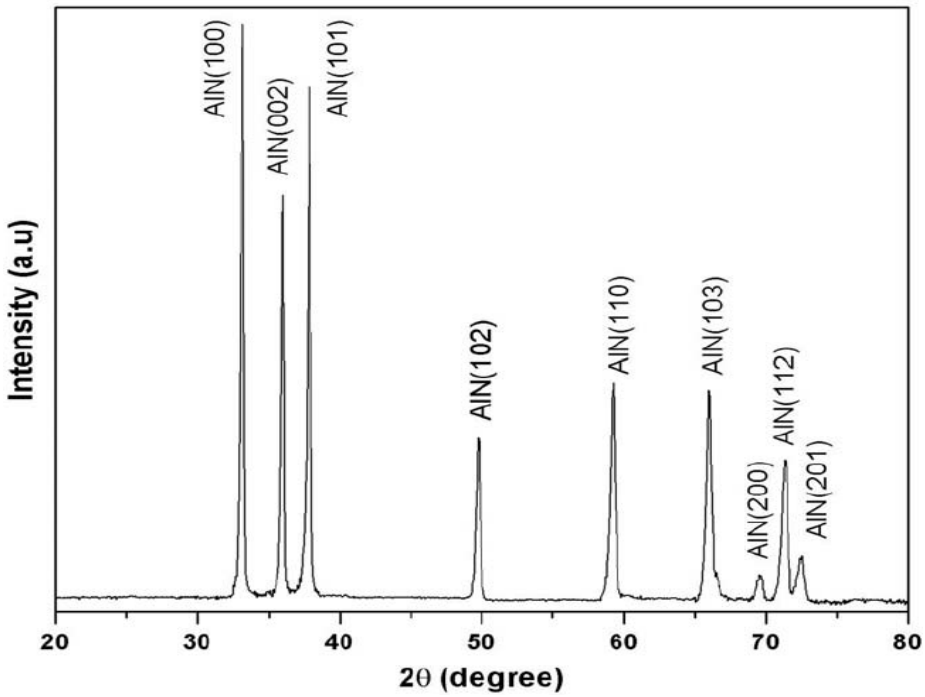

Figure 4. 8 X-ray diffraction pattern of fine AlN(Panda et al., 2014)

2θ $(degree)$	Intensity **(f)**	**Orientation (h k l)**
33.216	100.0	(1 0 0)
36.04	60.0	(0 0 2)
37.916	80.0	(1 0 1)
49.814	25.0	(1 0 2)
59.349	40.0	(1 1 0)
66.052	30.0	(1 0 3)
69.729	5.0	(2 0 0)
71.438	25.0	(1 1 2)
72.627	10.0	(2 0 1)
76.442	1.0	(0 0 4)

Table 4. 1 Hexagonal AlN- Powder Diffraction (Marlene C Morris et al., 1981)

In comparison to other materials, AlN has two key advantages. First of all, silicon semiconductor technology is completely compatible with it. Second, AlN has a material with a

large resistivity and a large band gap (6 eV). The AlN's properties were listed in the Table 4.2 below.

	AlN	**ZnO**	**PZT**
Density (kg/m^3)	3230	5610	7570
Piezoelectric constant (C/m^3)	E31 = -0.58 E33 = 1.55	E31 = -0.57 E33 = 1.32	E31 = -6.5 E33 = 23.3
Thermal conductivity (W/cm.℃)	2.85	0.6	0.018
Thermal expansion (1/℃)	= 4.2x10^{-6} = 5.3x10^{-6}	= 6.5x10^{-6} = 3.0x10^{-6}	= 2x10^{-6}
Young's modulus (GPa)	308	201	68
Acoustic velocity (m/s)	10,127	5,700	3,900
Index of refraction	2.08	2.01	2.67
Band gap (eV)	6.2	3.4	2.67
Resistivity(Ωcm)	1x10^{11}	1x10^{7}	1x10^{9}

Table 4. 2 common MEMS piezoelectric materials' properties.(Haynes, 2016)

Reactive magnetron sputtering was used to create AlN thin films from an aluminum target with a purity of 99.999 percent while using a high purity gas mixture of 99.995 percent argon and 99.995 percent nitrogen. A water-cooled target with a 6 cm diameter served as the magnetron cathode. Prior to deposition, the sputtering chamber pressure was lowered to 5.5x10^{-07} Torr.

Because it was available and affordable for the initial test, the glass substrate was chosen for the deposition of AlN films. Acetone and isopropanol were used to clean the substrate and get rid of any contamination on the surface. After pre-depositing AlN for an additional 5 min, the deposition power and gas ratio of the films were adjusted based on previous work (Armas Alvarado, 2017), as shown in Table 4.3. followed by a 60-minute deposit period. In this experiment, the Argon gas flux was chosen to be between 50 and 70 standard cubic centimeters per minute (sccm), and the Nitrogen gas was chosen to be between 30 and 50 (sccm). The chamber's pressure during the deposition process was set between 5 and 10 mTorr. The structure of the AlN films depicted in the figure was examined using an X-ray diffractometer (XRD).

Table 4. 3 Deposition parameters for AlN in attempt of reproducing previous work (Armas Alvarado, 2017).

Recipe	1st	2nd	3rd
Substrate	Glass	Glass	Glass
Flux Ar (sccm)	70	70	50
Flux N_2 (sccm)	30	30	50
High Vacuum (Torr)	5.50E-07	6.00E-07	8.00E-07
Pressure (mtorr)	5	5	10
Power (W)	190	60	190
Deposition time (min)	60	60	60

In the first iteration, as shown in Figure 4.12, we could not crystallize AlN; however, the third recipe depicts a small pick in the 37.5° region that, according to Table 4.1, is associated with (101) orientation of AlN. We changed the recipe by looking at those in the literature that our sputtering device could implement. We then considered the effects of each parameter, including the ratio of Ar:N_2 flux, pressure during the deposition, and power of deposition, in order to achieve the desired crystal orientation.

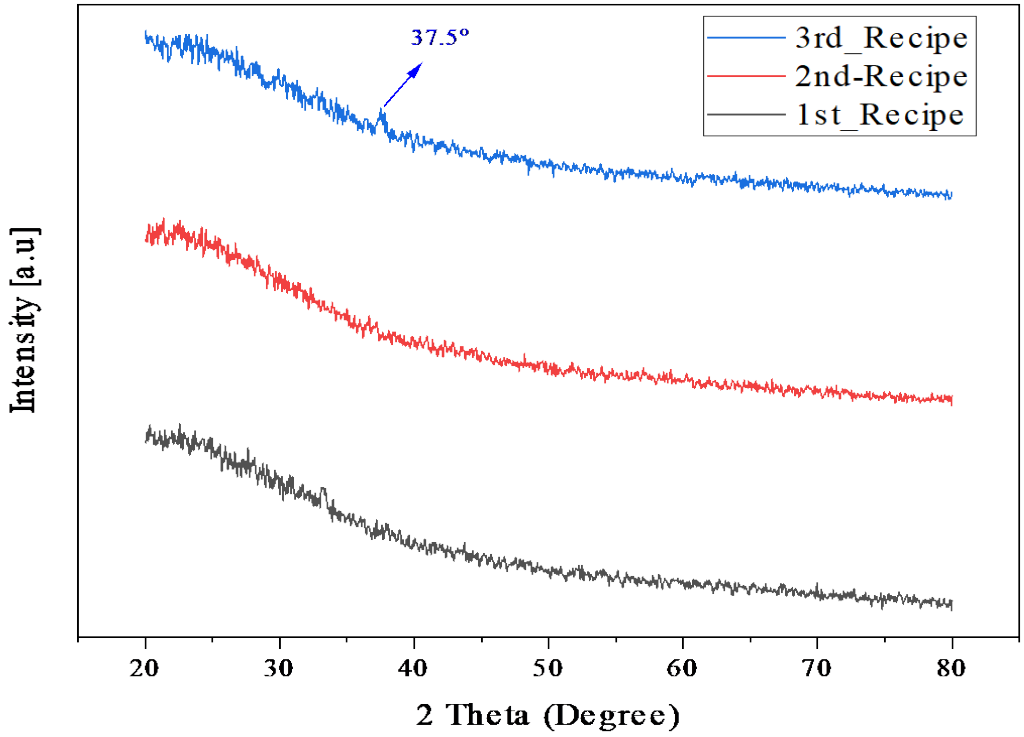

Figure 4. 9 First iteration of AlN deposition with three different recipes on the glass substrate.

In order to further our investigation, AlN was deposited on various substrates, including silicon and glass. In one recipe, a thin layer of molybdenum with 200nm thickness was first deposited on the glass substrate before the AlN film. Table 4.4 provides a summary of these recipes.

Table 4. 4 Deposition parameters for AlN in different substrates.

Recipe	1st	2nd	3rd
Substrate	Glass	Glass/Mo	Si
Ar (sccm)	50	50	50
N_2 (sccm)	50	50	50
Pressure (mtorr)	5	5	10
Power (W)	190	190	190
Deposition time (min)	50	50	50

We were able to confirm the presence of some peaks associated with various crystalline orientations, as shown in Figure 4.13. These peaks, however, needed to be oriented as desired. The

peaks at 33°and 37° in the first two recipes correspond to the AlN's (100) and (101) orientations, respectively (according to Table 4.2). We could see a small peak associated with the (002) orientation at 36° on the silicon substrate in the third recipe, they indicated that the substrate could influence the AlN's orientation. Although the Glass/Mo and Si substrates had intensity peaks visible at 33°, the Si substrate offers a higher peak than the Glass/Mo.

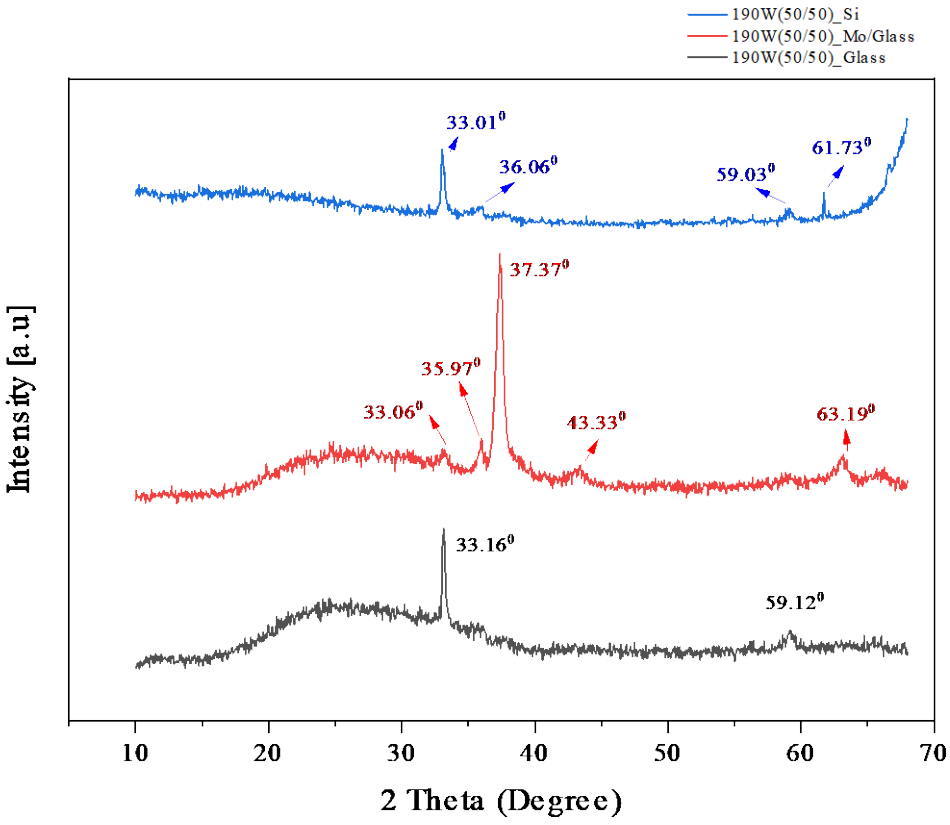

Figure 4. 10 AlN deposition with three different substrates (Glass, Glass/Mo, Si)

Now that the intensity peaks have been obtained, the optimization of the crystallization process followed by the third iteration recipes is summarized as shown in Table 4.5. In fact, we tried depositing on the same substrates used in the second attempt to verify the results while the gas flux has changed.

Table 4. 5 Deposition parameters for AlN in attempt of changing the Ar: N_2 ratio on different substrate.

Recipe	1st	2nd	3rd
Substrate	Glass	Glass/Mo	Si
Ar (sccm)	60	60	60
N_2 (sccm)	40	40	40
Pressure (mTorr)	5	5	5
Power (W)	190	190	190
Deposition time (min)	50	50	50

Table 4. 6 Si and Mo Powder Diffraction (Marlene C Morris et al., 1981)

Si Reflection			
2-Theta	**d(Å)**	**I(f)**	**(h k l)**
28.442	3.1355	100.0	(1 1 1)
47.302	1.9201	55.0	(2 2 0)
56.121	1.6375	30.0	(3 1 1)
69.130	1.3577	6.0	(4 0 0)
76.377	1.2459	11.0	(3 3 1)
88.026	1.1086	12.0	(4 2 2)

Mo Reflection			
2-Theta	**d(Å)**	**I(f)**	**(h k l)**
40.515	2.2247	100.0	(1 1 0)
58.608	1.5738	16.0	(2 0 0)
73.682	1.2847	31.0	(2 1 1)
87.595	1.1129	9.0	(2 2 0)

To study the crystallization, the flux ratio of Ar: N2 was selected 60:40. However, as seen in Figure 4.14, the (002) orientation has yet to appear in this iteration. However, it proved that altering the flux ratio of the gases improved crystallization quality. According to Table 4.6, the peak that occurred at 43.33° is related to Mo, and peaks at 59.13° and 61.9° in the silicon substrate are related to Si reflection on (3 1 1) and (4 0 0) orientation, respectively.

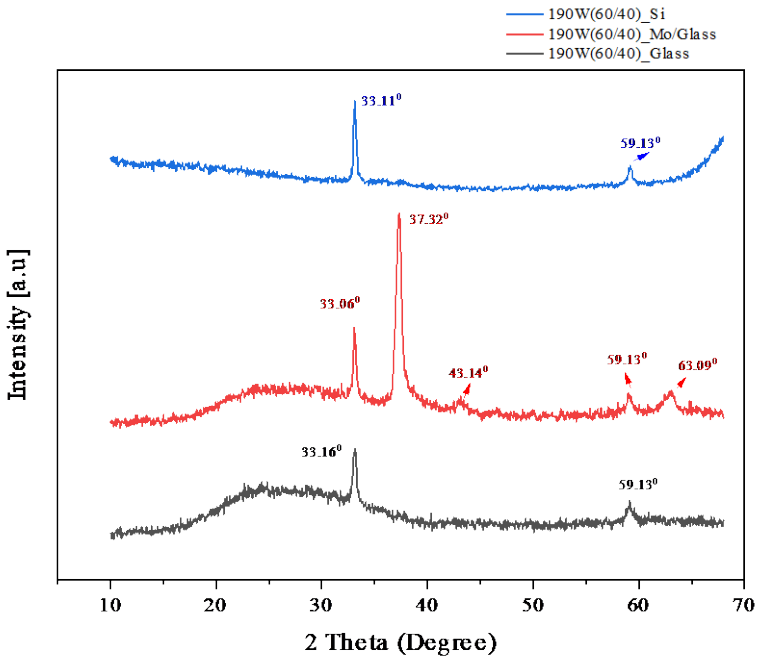

Figure 4. 11 AlN deposition with changing in gas Flux on different substrate

We continued the experiment by examining the changes in peak intensity from different orientations. The third test showed that modifying the gas flow ratio in the deposit could alter the crystallization quality. In this experiment, the influence of power changes on crystallization quality has been examined. For this purpose, we deposited AlN on the three substrates mentioned above by increasing the power while maintaining a fixed gas flow rate for all deposits, summarized in Table 4.7.

Table 4. 7 Deposition parameters for AlN in different substrates utilizing different power.

Recipe	1st	2nd	3rd
Substrate	Glass	Glass/Mo	Si
Ar (sccm)	50	50	50
N_2 (sccm)	50	50	50
Pressure (mtorr)	5	5	5
Power (W)	210	210	210
Deposition time (min)	50	50	50

Figure 4.15 shows the peak intensity at 36°. It can be observed that the peak in the glass substrate has been enhanced with a layer of Mo. Furthermore, the substrate for Si showed this

peak. This demonstrated that increasing the power to 210W could improve crystallization in the desired orientation at 36°.

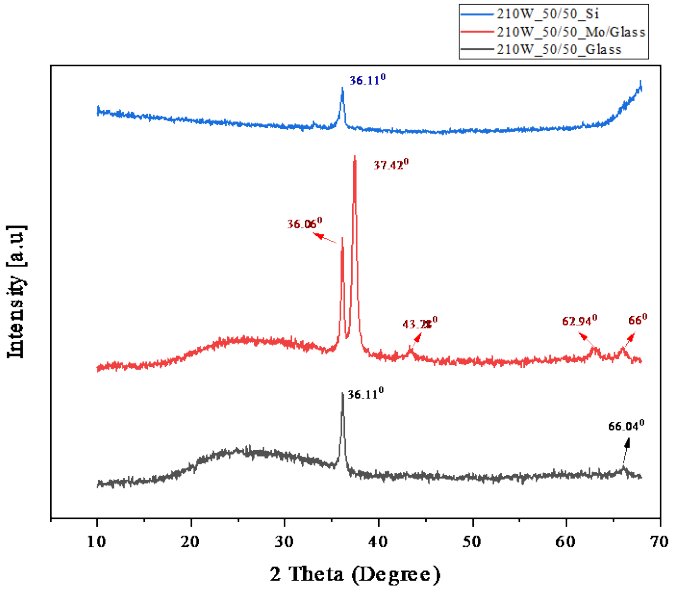

Figure 4. 12 AlN deposition by increasing the power of the deposition

Increased power can enhance the quality of the intensity peak in glass with a Mo substrate, according to the previous iteration. In order to confirm a better crystallization outcome, we investigated higher power using the same recipe on glass substrate with a Mo coated, increasing the power from 230 W to 270 W. Table 4.8 provides information regarding the fifth recipe used in this iteration.

Table 4. 8 Deposition parameters for AlN utilizing different power.

Recipe	1st	2nd	3rd
Substrate	Glass/Mo	Glass/Mo	Glass/MO
Ar (sccm)	50	50	50
N_2 (sccm)	50	50	50
Pressure (mTorr)	10	10	10
Power (W)	230	250	270
Deposition time (min)	50	50	50

Figure 4.16 showed that by increasing the power from 230 to 270 W, the intensity peak of the orientation increased. This test was designed to determine the impact of power on

crystallization. Due to limitations in our sputtering equipment, which could not operate at higher power for an extended period, we were forced to optimize our recipe. To get around this restriction, we concentrated on adjusting the gas flux ratio and lowering the power to reach the peak's maximum at 36° for AlN orientation.

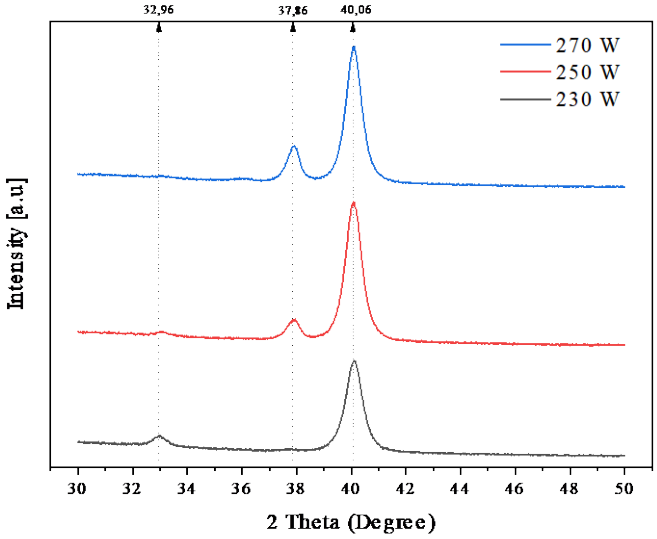

Figure 4. 13 AlN deposition with three different powers of deposition

Changing the gas flux ratio allowed researchers to study crystallization(Jiao et al., 2015). We proposed a new recipe that could be used with our sputtering device after analyzing the impact of power intensity on crystallization in our first recipe. As a result, we ran tests on glass with Mo substrates. Below is a summary of the recipe that was used for this iteration.

Table 4. 9 Deposition parameters for AlN with various Ar:N_2 ratio.

Recipe	1st	2nd	3rd	4th
Substrate	Glass/Mo	Glass/Mo	Glass/Mo	Glass/Mo
Ar (sccm)	50	34	25	20
N_2 (sccm)	50	66	75	80
Pressure (mTorr)	5	5	5	5
Power (W)	200	200	200	200
Deposition time (min)	50	50	50	50

In this experiment, the effect of the gas flux on the crystallization's intensity was confirmed using the various gas flux ratios shown in Table 4.9. We increased the crystallization of our desired orientation by altering the Argon to Nitrogen gas ratio and increasing Nitrogen. The power level was determined to be 200 W, which was more than enough for our equipment. According to Figure 4.17, the ideal ratio of Ar to N2 is 1:3. As explained before, Mo intensity peak occurs at 40° and the desire orientation of AlN acquires at 36°.

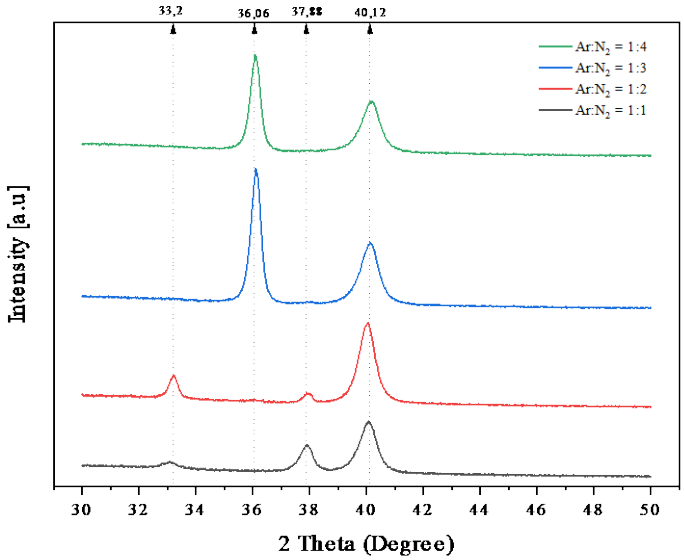

Figure 4. 14 AlN deposition with four different ratio of gas flux

After using the recipe to produce a high peak intensity, the optimization process was conducted by cleaning the chamber in order to create an effective crystal result. The clean chamber, free of any other materials, is necessary for depositing the AlN and growing the desired orientation. As a result, we coated our chamber using various pre-Sputtering times ranging from 5 to 120 minutes, as shown in Table 4.10.

Table 4. 10 Deposition parameters for AlN utilizing different power (ratio of Ar:N_2 1:3).

Recipe	1st	2nd	3rd
Substrate	Glass/Mo	Glass/Mo	Glass/MO
Ar (sccm)	25	25	25
N_2 (sccm)	75	75	75
Pressure (mTorr)	5	5	5
Power (W)	200	200	200
Pre-deposition time (min)	5	60	120
Deposition time (min)	50	50	50

Applying 120 minutes of pre-sputtering time before depositing the AlN on the substrate increased the intensity of the desired orientation, as shown in Figure 4.18. Additionally, this experiment demonstrated that the chance of growing the AlN (002) orientation was increased by cleaning the chamber with different pre-deposition timing.

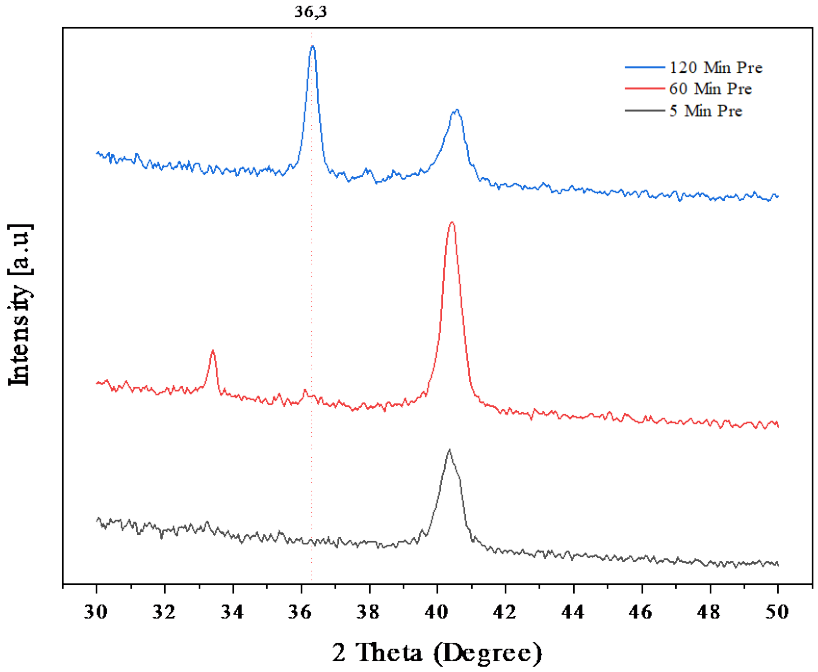

Figure 4. 15 AlN deposition with three different durations of pre-deposition

The optimization process was conducted on the glass with a Mo substrate. In the following step, we deposited a seed layer of AlN before deploying Mo to examine the impact of this seed layer deposition on crystallization in order to grow the desired orientation crystal. The literature demonstrated that depositing an AlN seed layer first, followed by a final piezoelectric layer, improved the last layer's crystallization (Kamohara et al., 2008).

Table 4. 11 Deposition parameters for AlN utilizing seed layer.

Recipe	1st
Substrate	Glass
Flux Ar (sccm)	25
Flux N_2 (sccm)	75
Pressure (mTorr)	5
Potential (W)	200
Pre-deposition time (min)	5
Deposition time (min)	30

The XRD depicted in Figure 4.19 shows the AlN's desired orientation has improved significantly. In this test, the seed layer of AlN was deposited 30 minutes before the deposition of Mo, in an effort to enhance the quality of the crystallization. In this experiment, a sample was patterned, etched, and then the orientation of the deposited layers was observed using XRD.

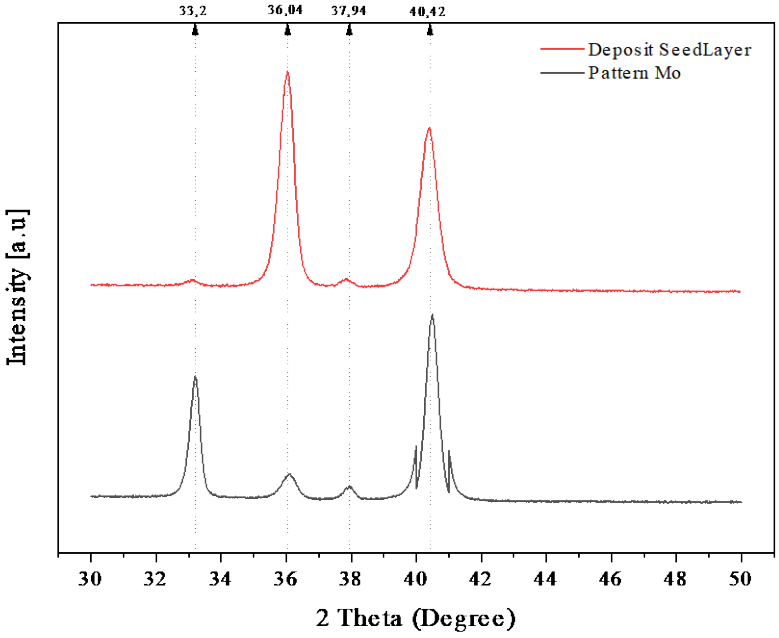

Figure 4. 16 AlN deposition by applying seed layer of AlN

Our main objective is to enhance the quality of the desired orientation, so we have used various techniques while modifying other variables to improve the crystallization for AlN. Argon and N_2 gas flux ratios in this test were 1:3 in volume. A fixed 200 W was set as the potential. Using the same recipe previously used on the glass substrate with a seed layer, we tried annealing for 4 hours. The substrates were heated to various temperatures between 300 and 700 °C, summarized in Table 4.12.

Table 4. 12 Deposition parameters for AlN applying different annealing temperature.

Recipe	1st	2nd	3rd
Substrate	Glass/Mo	Glass/Mo	Glass/MO
Ar (sccm)	25	25	25
N_2 (sccm)	75	75	75
Pressure (mTorr)	5	5	5
Power (W)	230	250	270
Deposition time (min)	50	50	50
Annealing (4 hours) ℃	300	500	700

Most of the time, annealing could alter the orientation of the material. The impact of annealing on the crystallization of the glass substrate with the AlN seed layer is shown in Figure 4.20. It is shown that 500 ℃ is the ideal temperature for a maximum intensity peak.

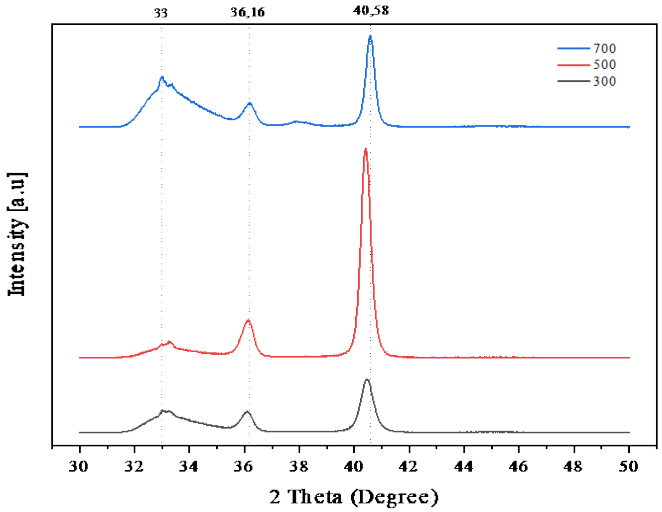

Figure 4. 17 AlN deposition with three different temperatures on Glass substrate with seed layer of AlN

In the following test, we skipped the seed layer and annealed the glass substrate without it. The same recipe was used shown in table 4.12. The temperature ranged from 300 to 700 ℃. The maximum intensity peak was reached at a temperature of 300 ℃, as shown in Figure 4.21. However, the crystallization quality did not significantly change as the temperature raised.

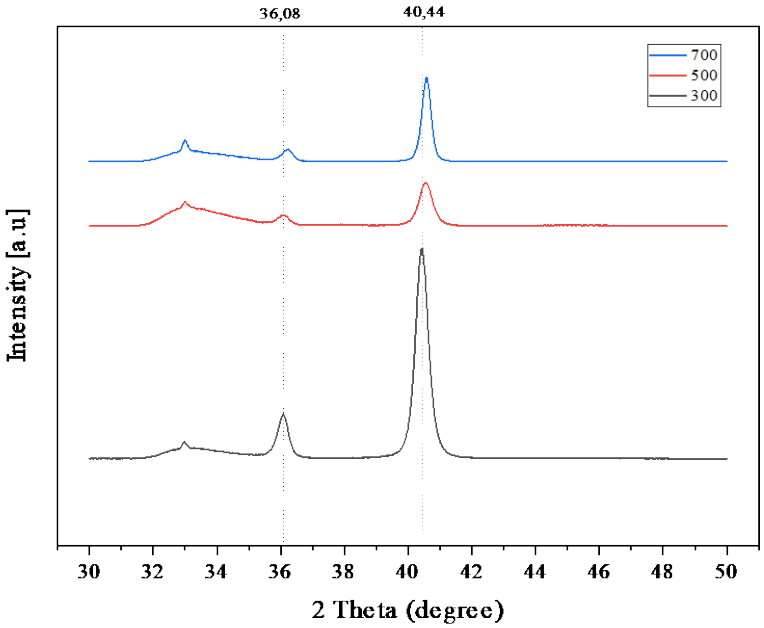

Figure 4. 18 AlN deposition with three different temperatures without applying seed layer

After performing a few experiments on glass, we tried depositing the AlN and Mo on the Si to see how the substrate and annealing would affect the crystallization. Table 4.13 provides a summary of the recipes. It can significantly enhance crystallization by adjusting the temperature, as shown in Figure 4.22.

Table 4. 13 Deposition parameters for AlN depositing on Si and applying different annealing temperature

Recipe	1st	2nd	3rd	4th
Substrate	Si	Si	Si	Si
Flux Ar (sccm)	25	25	25	25
Flux N_2 (sccm)	75	75	75	75
Pressure (mTorr)	5	5	5	5
Potential (W)	200	200	200	200
Sputtering (min)	50	50	50	50
Annealing (4 hours)℃	-	300	500	700

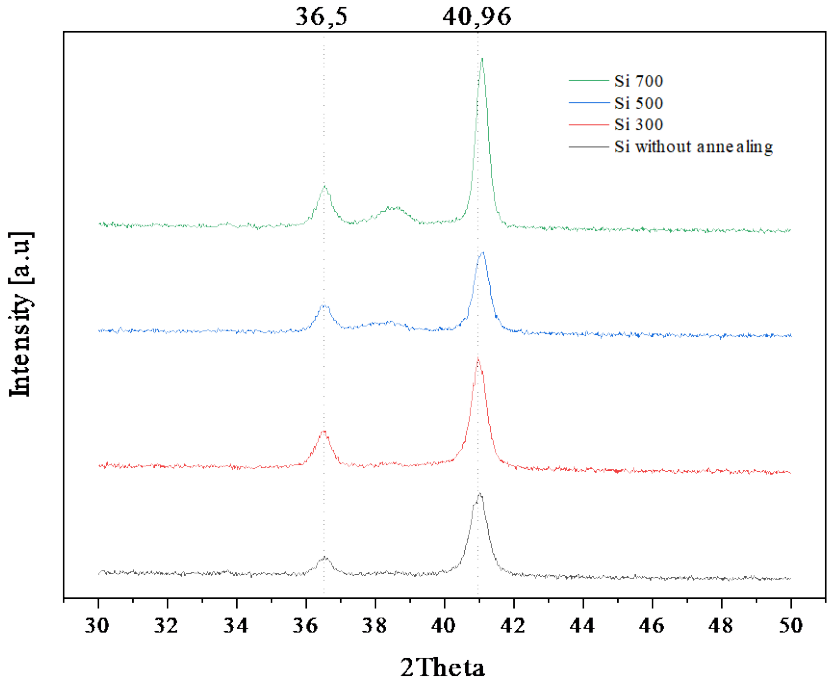

Figure 4. 19 AlN deposition with three different temperatures on Si substrate

However, raising the temperature had an impact on other orientations that were intended for something other than our application and didn't improve much the quality of the desired orientation. A temperature of 300°C is appropriate for this experiment, as shown in Figure 4.22.

Finally, using the knowledge from our study, we were able to deposit AlN on the 50 m thick alumina membranes as a substrate in the desired orientation. The Intensity peak of (002) is shown in Figure 4.23 at 36°, and Mo is shown at about 40°.

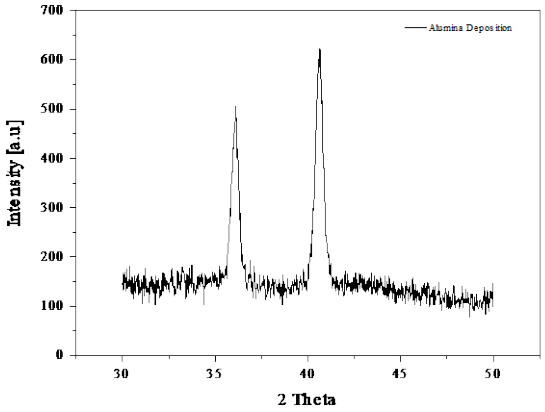

Figure 4. 20 AlN deposited on Alumina

4.3 FBAR sensor fabrication

This section demonstrates the manufacturing process of sensor FBAR step by step. Figure 4.24 presents the geometry of the guides manufactured in this work. Each stage of the sensor FBAR manufacturing process is described in this section. The FBAR was made in this study using N-type crystalline silicon that met the specifications of 1 surface polish, resistivity 0-100 ohm-cm, orientation (100), and a diameter of 2 inches. AAO (Nano porous Anodic Aluminum Oxide) from InRedox, which has a 50 μm thickness and a 25 mm diameter, has also been used. A substrate endures a chemical RCA cleaning process to remove contaminants before the deposition.

The deposition and patterning of the sensor are done in the order described below:

A. SiO_2 deposition: In order to protect the substrate from wet etching, SiO_2 deposited on desire surface. The recipe has been utilized in this process describe as follows:
    - Flux Ar: 40 sccm
    - Flux O_2: 60 sccm
    - Power: 100W
    - Pressure: 2 mTorr
    - Pre-deposition time: 5 min
    - Deposition time: 60 min
B. AlN deposition (Seed layer): In this step, a seed layer of AlN was deposited to be sure about the crystallization of the AlN, the process takes 30 min depositing with the same recipe for AlN piezoelectric layer. In this process of deposition 10-15 min pre-deposition has been applied. If the target is changed before the deposition, the holder and chamber were exposed for about 60 min to clean the chamber and be ready for final deposition. The thickness produced by this deposition is approximately 350 nm. The recipe that has been utilized in this process describe below:
    - Flux Ar: 25 sccm
    - Flux N_2: 75 sccm
    - Power: 200 W
    - Pressure: 5 mTorr
    - Pre-deposition time: 10 min
    - Deposition time: 30 min
C. Mo deposition: For bottom electrodes, this layer is used. This procedure was carried out without opening the chamber after the first seed layer was deposited. This

layer's thickness is approximately 300 nm based on timing. The Mo deposited with the following recipe

- Flux Ar: 10 sccm
- Flux Pressure: 2 mTorr
- Power: 100 W
- Pre-deposition time: 5 min
- Deposition time: 30 min

D. AlN deposition: The recipe for this layer, which serves as the main layer of the piezoelectric sensor, is the same as the recipe used in step B. The thickness was measured around 700 nm which after 60 minutes of deposition time is acquired in this step.

E. Mo disposition (Top layer): The first use of this layer is as a mask to shield the AlN from wet etching with KOH, and the second is as the top electrode of the FBAR. The Mo was deposited using the same recipe, in step C.

F. Annealing: The FBAR sensor sample was placed in the oven at 300 ℃ for 4 hrs., the oven was turned off after 4 hours, and the sample was allowed to cool for 24 hrs. in order to reform and improve crystallization.

G. Masking Mo: The photoresist AZ1518 has been used as the first masking step in this step. One application (roughly 6-7 drops) was made to the substrate, which was then centrifuged for 30 seconds at 3000 rpm. The sample was then placed on a hot plate set at 110 ℃ for about a minute to allow the photoresist to dry. The photoresist was exposed using a MicroWriter at 450 j/cm^2 with one correction. After exposition, the sample was stirred for 45 seconds while being developed with AZ 351 to remove the photoresist that had not been exposed.

H. Wet etching the Mo (top layer): The Mo is removed in this step using Al etch solution. Etching the Mo and cleaning the surface took about 1:50 minutes. To

remove all the solution and stop any further etching caused by the solution remain on the substrate, rinse the substrate under DI water sufficiently.

I. Wet etching the AlN: the KOH solution has been used to etch AlN and it depends on the thickness of the AlN, it took between 1:30- 2:00 min for each 60 min deposition.

J. Masking the Mo (bottom layer): This process involves repeating the G step.

K. Wet etching the Mo (Bottom layer): This step has been conducted using the same methodology as H.

L. Covering electrode: The layer is protected by the AZ 9260 photoresist in order to avoid short circuits. In contrast to AZ1815, the AZ 9260 uses a different exposure formula. It is applied once, centrifuged for 30 seconds at 3000 rpm, and then heated on a hot plate for two minutes at 110 ℃. The exposure power was set to 960 j/cm^2. This method uses a 4:1 dilution of 400K developer, and the substrate is submerged in the solution for 3 minutes. In the final step of this procedure, the sample was heated on the hot plate for 3 minutes at 170 ℃.

M. Ti, Cu deposition: Ti and Cu are deposited as the signal and ground electrodes as the last step in the deposition process. The following recipe is used in this process to first deposit Ti, which serves as a copper adhesion. The second step of this procedure deposits a seed layer of copper (Cu) using the formula below. We grow copper using an electroplating technique so that we can better control its thickness.

    Recipe for Ti:

    - Flux Ar: 10 sccm
    - Power: 100 W
    - Pressure: 2 mTorr
    - Pre-deposition time: 5 min
    - Deposition time: 50 Sec

Recipe for Cu:

- Flux Ar: 10 sccm
- Power: 70 W
- Pressure: 2 mTorr
- Pre-deposition time: 5 min
- Deposition time: 20 min

N. Copper masking: step L is repeated in this process with the same photoresist and developing process.

O. Copper electroplating: The process of producing a metal coating on a solid substrate by reducing the cations of that metal using a direct electric current is known as the electroplating of copper, also known as electrochemical deposition or electrodeposition. The component that needs to be coated serves as the cathode (negative electrode) of an electrolytic cell; the electrolyte is a solution of the metal's salt, and the anode (positive electrode) is typically either a block of the metal itself or some other inert conductive material.

P. Back etching with laser

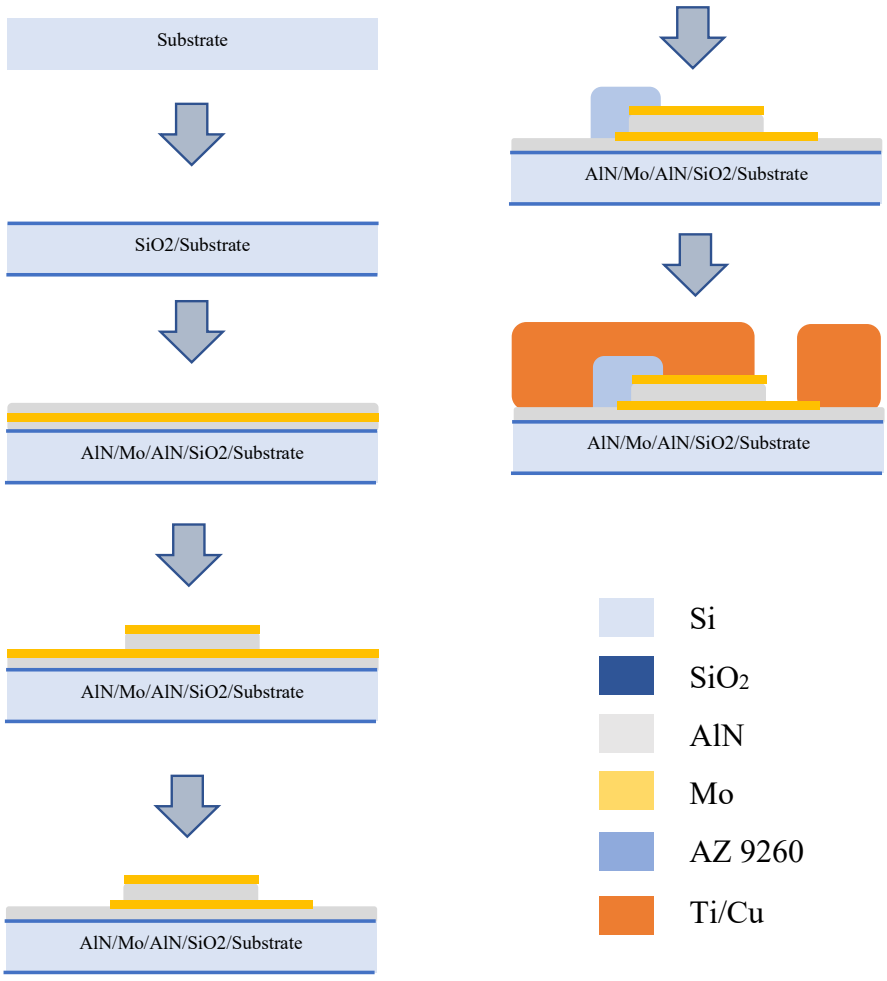

Figure 4. 21 Illustration of fabrication of FBAR in this project.

4.4 Sensor design

The biosensor mask in this section was created using Advanced Digital Systems (ADS). The two designs of the biosensor—Shunt and Series—are shown in the Figures below. The microscope image of FBAR biosensor is illustrated in Figure 4.26

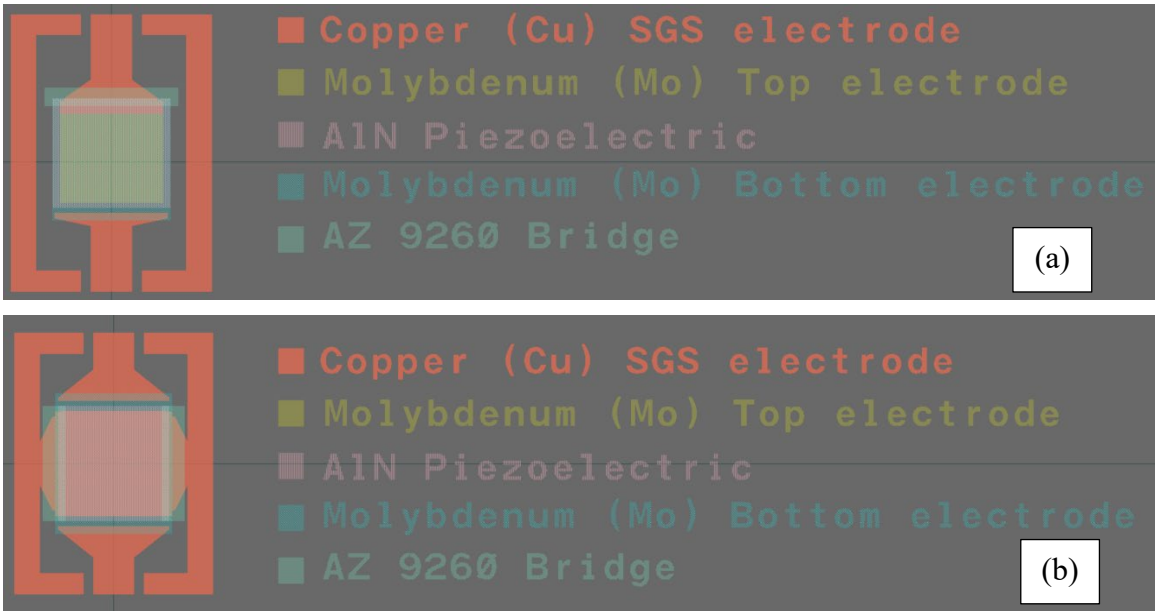

Figure 4. 22 Illustration of sensor design (a) Series (b) Shunt.

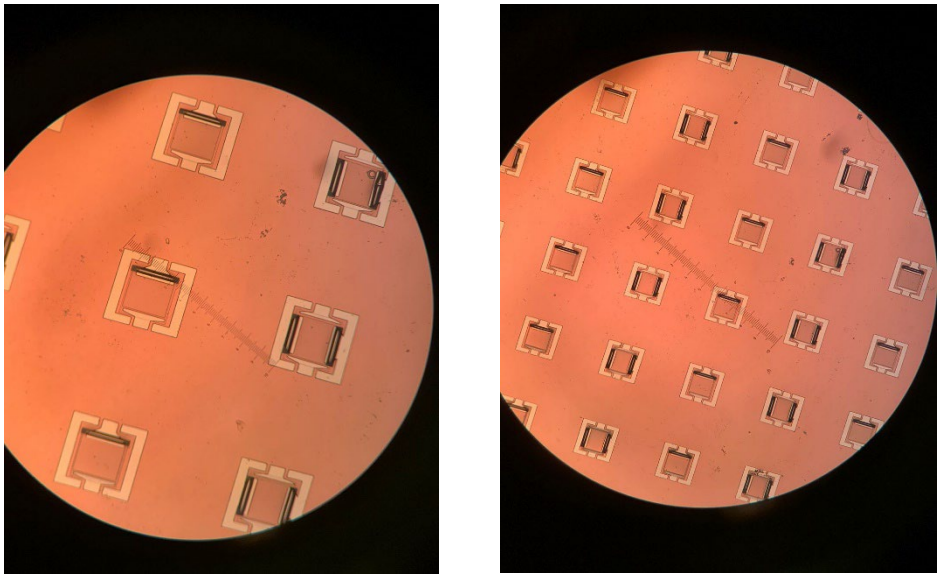

Figure 4. 23 Fabricated FBAR biosensor.

4.5 Test and result

The initial measurement was performed and is depicted in figures 4.25 and 4.26 with series and shunt arrangements on an Alumina membrane. The outcome shows a resonance of 1.2 GHz. However, resonance is not a desirable quality.

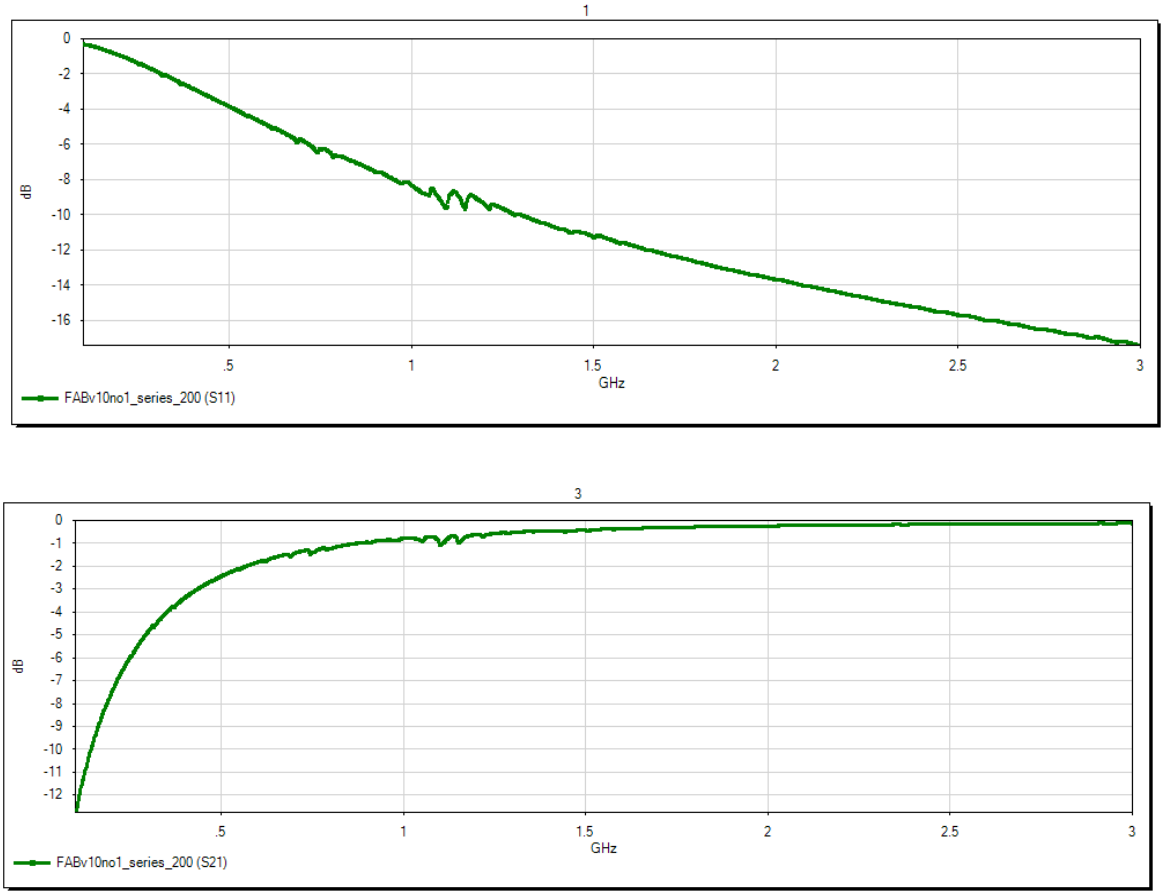

Figure 4. 24 Series arrangement of FBAR on Alumina membrane

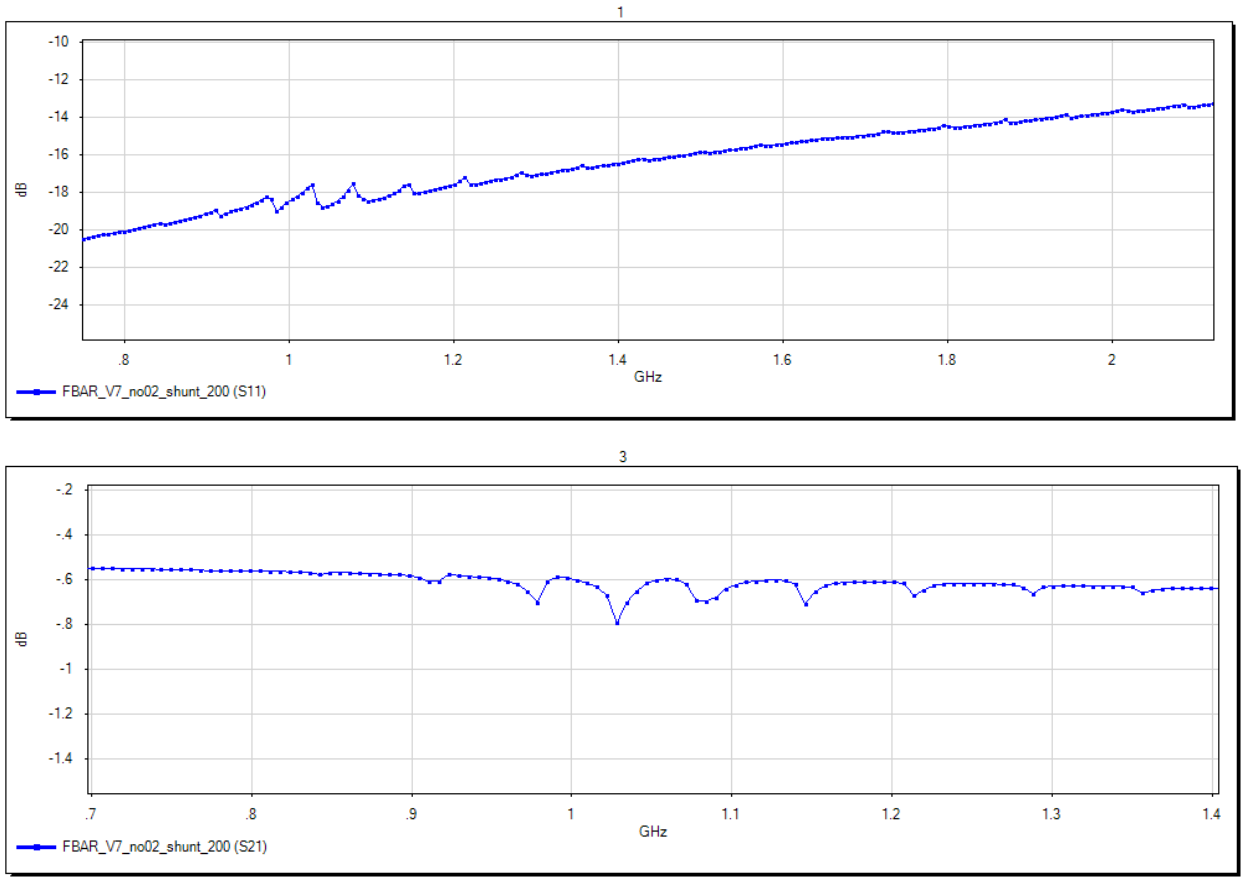

Figure 4. 25 Series arrangement of FBAR on Alumina membrane

Figure 4.27 shows the findings from the second measurement. The first sample had a shunt arrangement, and the second sample had the same device with the back etched. In fact, the resonant frequency is slightly improved by using back etching.

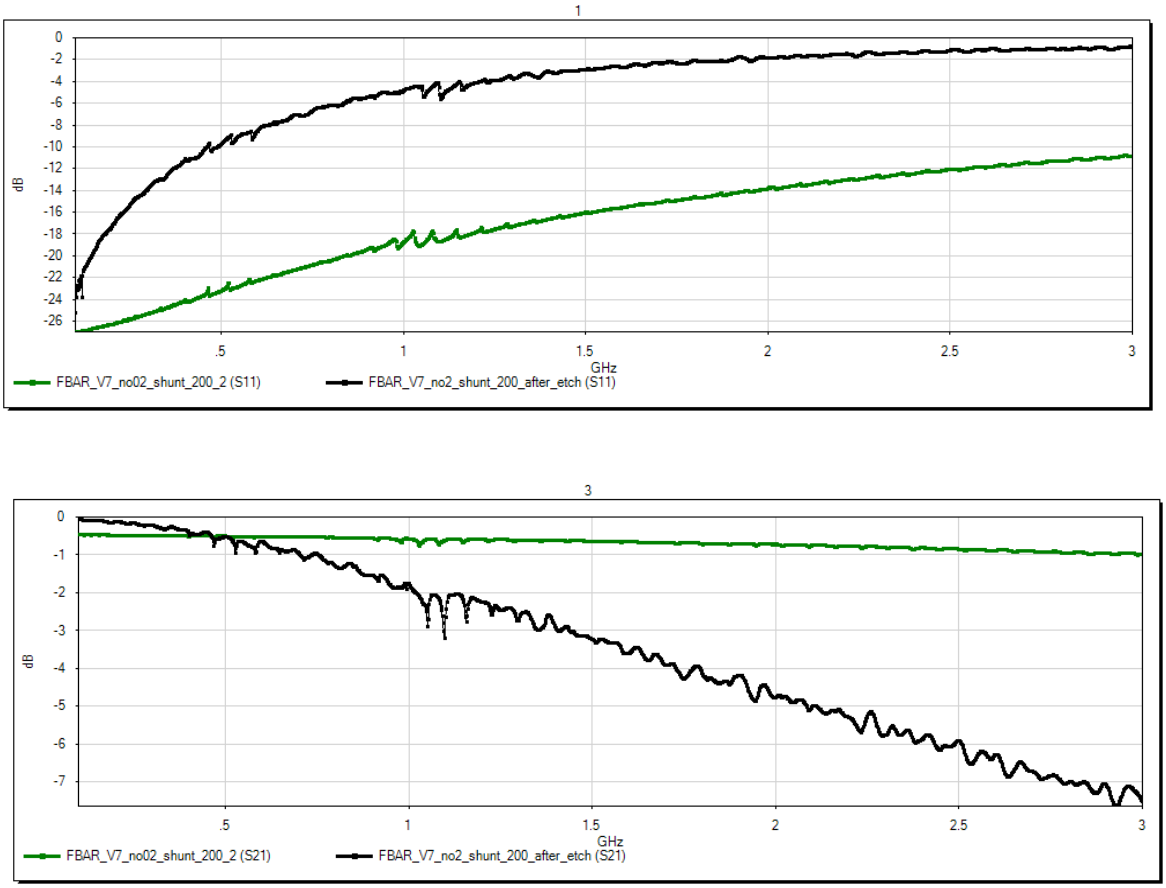

Figure 4. 26 FBAR sensor shunt arrangement with and without back etching

The project then proceeded to deposit sensor layers on a Si substrate, and the outcomes were as follows. The intriguing finding in the Figures are that both the shunt and series arrangements have multiple notches around the resonant frequency. These merely take place if the back is not etched.

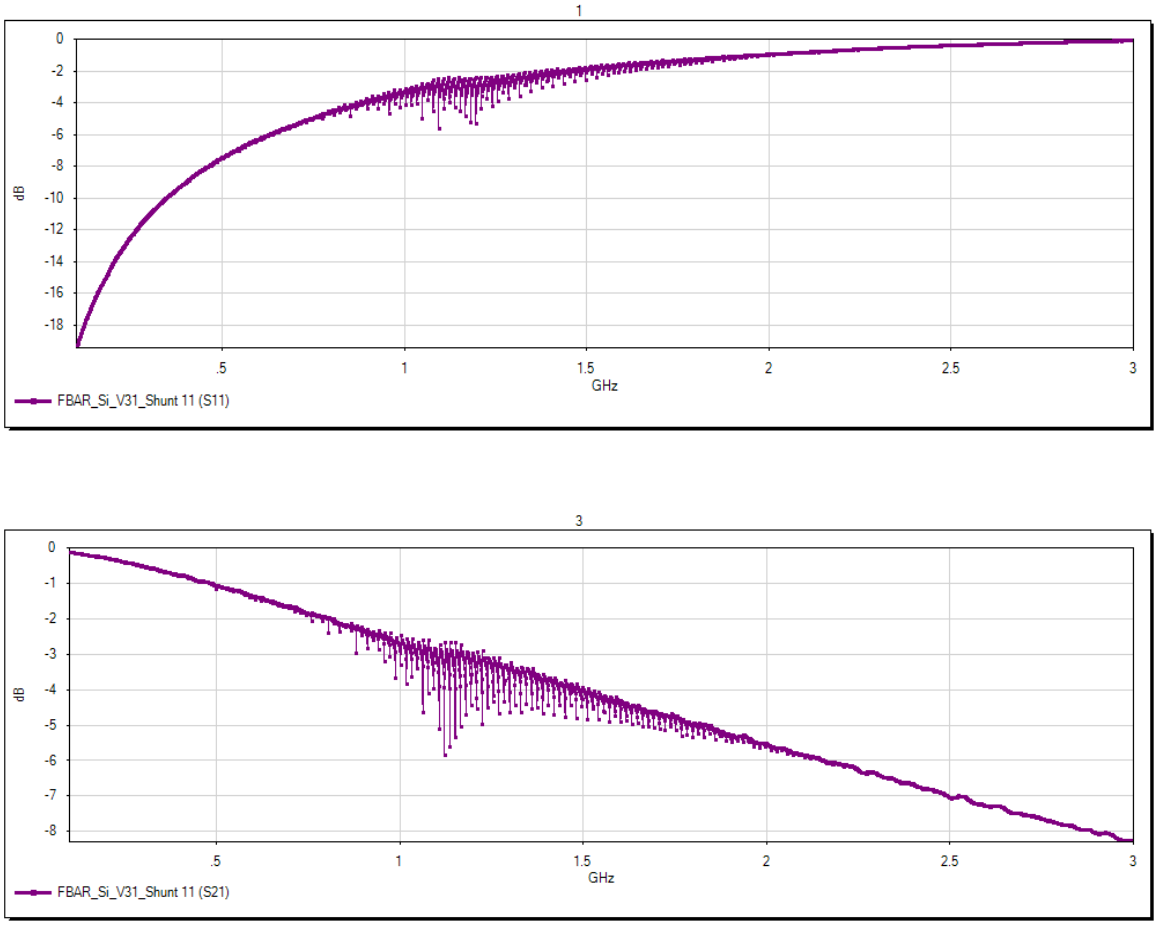

Figure 4. 27 FBAR Shunt arrangement on Si

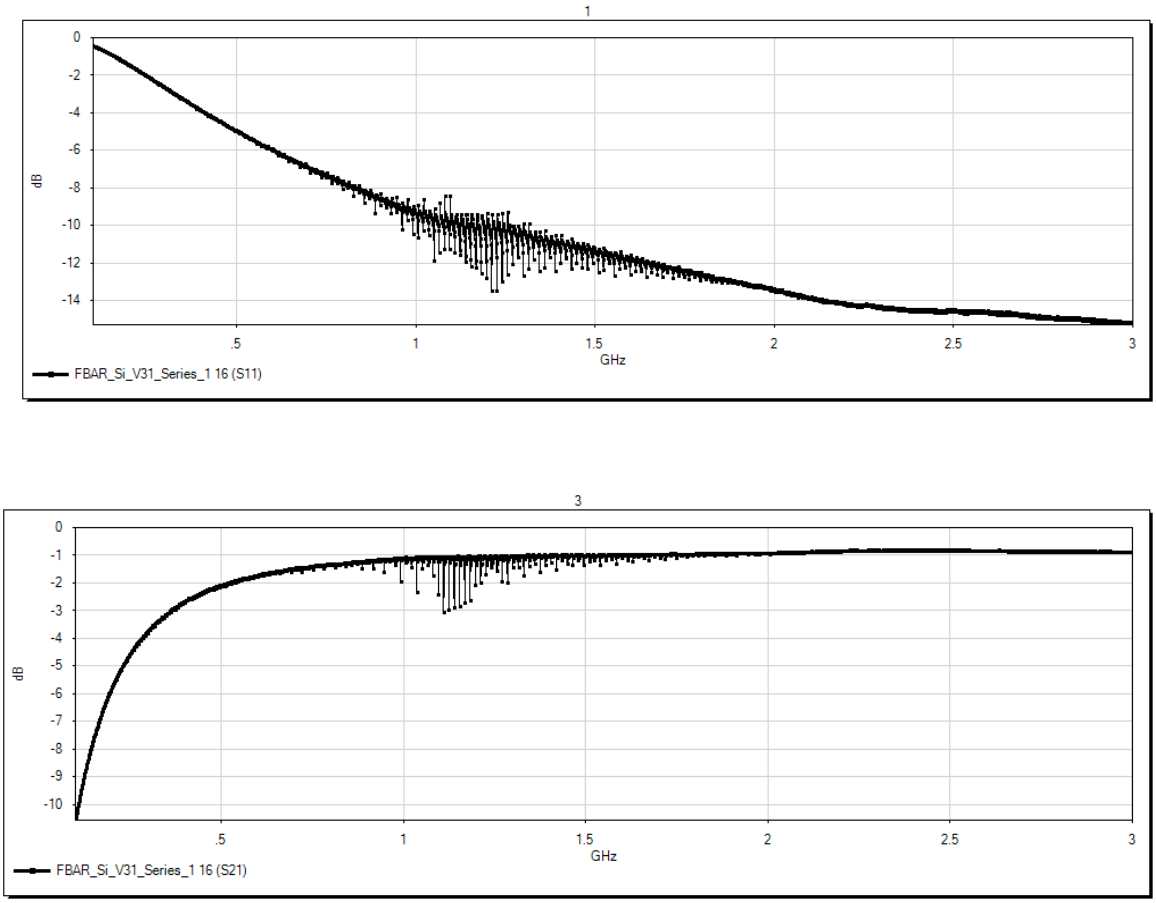

Figure 4. 28 FBAR Series arrangement on Si

Chapter 5: Stub resonator biosensor development

In this chapter, a biosensor that uses a stub resonator and is coated in MIP and NIP bioreceptors to detect different glucose concentrations is developed. This experiment is divided into two phases: designing and simulating the microwave stub resonator based on the desired frequency and fabricating the sensor using the material at hand, such as FR4, in the second and final part of the process, which involved fabricating the MIP, NIP bioreceptors and coating the sensor. In order to check the repeatability and selectivity of the proposed sensor, the sensor was evaluated by applying different concentrations of glucose, mannose, and galactose. The experiment is detailed and explained as follows. The experiment was conducted at the Microelectronics Laboratory of USP (LME-University of São Paulo).

5.1 Sensor design

The model of the proposed sensor can be seen in Figure 5.1. The entire sensor is 70 mm by 50 mm, without any miniaturization effort. The sensor was designed on the 1.6 mm thick FR4 with 17 μm of copper on both sides. The FR4 material has been chosen as substrate due to its availability and low cost. It has a relative permittivity of 4.4 and tan δ of 0.02 at 1 GHz frequency. On the top layer, a 50-Ω microstrip transmission line, 3 mm wide, was fabricated. A quarter wavelength stub with a length of 5 mm, and 3 mm wide was placed in the middle of the microstrip line. The copper of the FR4 was removed using a precise laser milling process (LPKF U3 system), while 1 mm off the tip of the stub was covered with glucose-sensitized MIP.

The same stub structure was built to use as a reference, without the MIP, to validate the measurements. The reference stub was constructed face to face with the sensing one to simplify the fabrication of the channel and flow of the aqueous solutions in the sensing region. It allows us to measure both responses simultaneously: the distance between two microstrips is 17 mm, and the tips of two stubs are 7 mm apart. Each microstrip was soldered to two subminiature version A

(SMA) connectors as input and output RF ports. Two duplicated sensors from the same fabrication process were elaborated to validate the performance of the biosensor at several attempts.

The microfluidic system was designed, and 3D printed by a high-resolution SLA/DLP 3D printer (Creality Model LD-002R) to provide a specific volume of the solution in the sensing area. It was glued with transparent epoxy on the top of both stub resonators at the center to seal the sensing area and prevent leakage. To track the flow visually, a transparent photo resin was chosen to create the microfluidic system. It was printed with a length of 40 mm, a width of 15 mm, and a height of 4 mm. Two pairs of inlets and outlets were designed with a diameter of 2 mm and placed 18 mm apart. At the bottom of the housing, two channels were designed with a depth of 1mm and a length of 18 mm to be filled with the glucose solutions to be characterized.

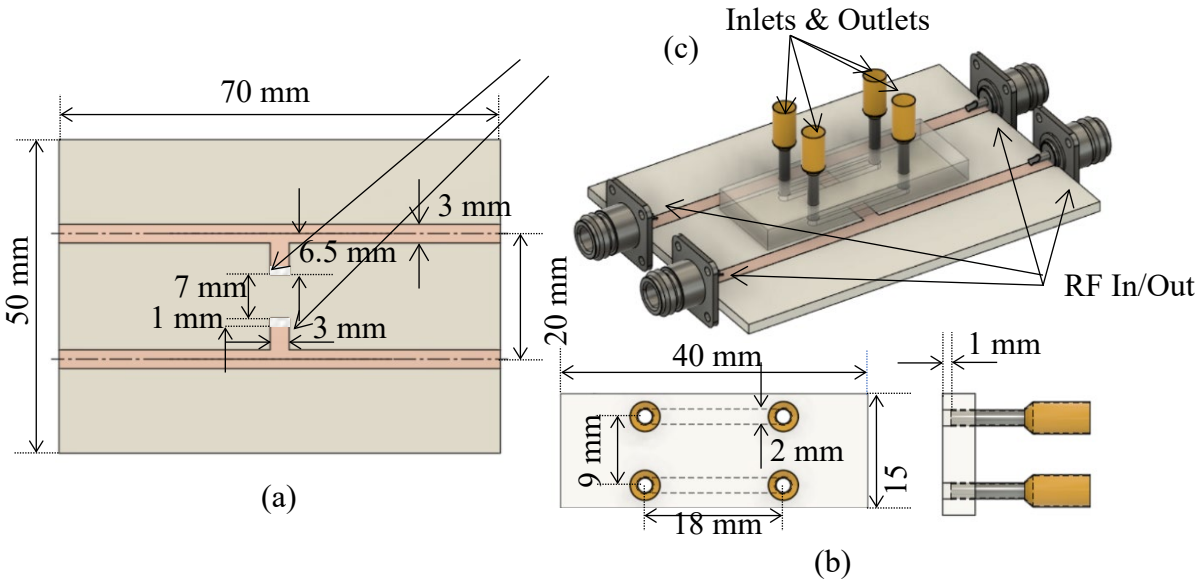

Figure 5. 1 The designed MIP-coated microwave-based stub biosensor (a) Top view of the biosensor (b) Top view and side view of the microfluidic system with the inlets and outlets (c) View of the assembled biosensor.

5.2 Simulation

In order to analyze the performance of the sensor in terms of frequency responses, Ansys Electronics Desktop was utilized as a 3D EM simulator. The unloaded sensors were designed to operate at 7 GHz, and a shift towards lower frequencies was expected when the liquid under test flowed in the sensing region at the tip of the stub resonator due to the high relative permittivity of

water ε_r ~ 80. The modeled structure of an uncoated sensing device, shown in Figure 5.2, was used as a proof of concept for the RF design. Therefore, a set of simulations was conducted in which the flow channel was first unloaded, filled with air, and then loaded, filled with DI water with a relative permittivity of 80.

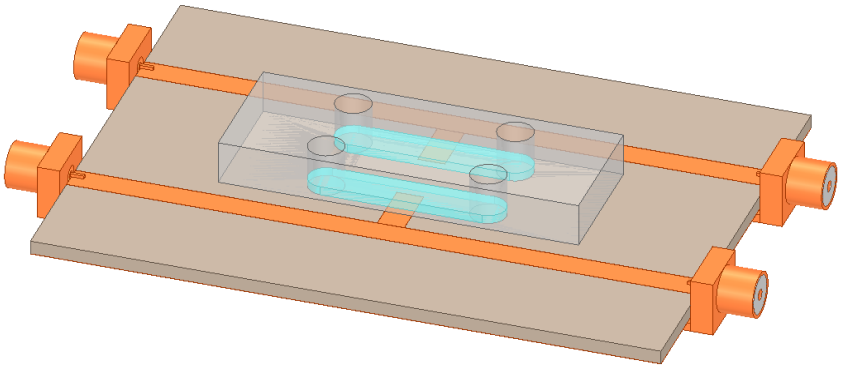

Figure 5. 2 HFSS model of the uncoated microwave-based stub sensing device.

5.3 General Theory of Open Stub Resonator

A general illustration of an open stub resonator is shown in Figure 5.3. The stub resonator is open-circuited at one end and connected in shunt with a 50- Ω transmission line at the other end.

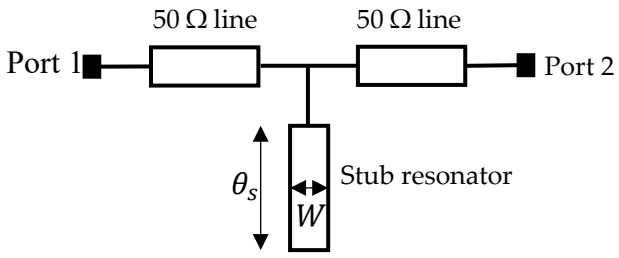

Figure 5. 3 Open stub resonator illustration.

The input impedance of the resonator was calculated as in equation (1) which is extracted from the mathematical model of the open stub resonator (Pozar, 2012).

$$Z_{in} = -jZ_s \cot \theta_s = \frac{Z_s}{j \tan \theta_s} \tag{1}$$

Where $Z_s$is the characteristic impedance of the open stub resonator and $\theta_s$is the electrical length in degree, the ABCD matrix (equation (2)) of the open stub resonator was extracted from equation (1), shown below:

$$[T_s] = \begin{bmatrix} 1 & 0 \\ Y_{in} & 1 \end{bmatrix} = \begin{bmatrix} 1 & 0 \\ \frac{j \tan \theta_s}{Z_s} & 1 \end{bmatrix} \tag{2}$$

Then, the S-parameters of the open stub resonator (S12, S21) were calculated by converting the ABCD matrix in equation (2) to S-parameter in equation (3). Hence,

$$\begin{aligned} S_{12} = S_{12} &= \frac{2}{A + \frac{B}{Z_0} + CZ_0 + D} \\ &= \frac{2}{1 + \frac{0}{Z_0} + \left(\frac{j \tan \theta_s}{Z_s}\right) Z_0 + 1} \\ &= \frac{2}{2 + \left(\frac{j \tan \theta_s}{Z_s}\right) Z_0} \end{aligned} \tag{3}$$

A normalized characteristic of impedance and impedance of resonator were considered Z_s=$Z_0 = 1$to simplify analysis and discussion of the attenuation response of stub resonators. The electrical length of the stub should be regarded as $\theta_s = 90^o$ (or π/2 radian) to achieve a notch response in an open stub resonator; hence, the S-parameter of equation (3) simplifies in equation (4),

$$S_{12} = S_{21} = \frac{2}{2 + \left(\frac{j \tan\left(\frac{\pi}{2}\right)}{Z_s}\right) 1} \approx 0 \tag{4}$$

or in decibel, as shown in equation (5)

$$|S_{12}|^2 dB = |S_{21}|^2 dB = 20\ log_{10}(0) = \infty\, dB \tag{5}$$

From equation (5), an ideal infinite attenuation or notch is obtained when the electrical length of the open stub resonator is a quarter-wave (λ/4).

Figure 5.4 illustrates the model of the biosensor with a stub as a quarter-wavelength resonator where the MIP was coated at the tip of the stub. An equivalent circuit model of our proposed sensor is shown in Figure 5 (b). The stub resonator can be modeled by a resistance (R), inductance (L), and capacitance (C) that is followed by capacitance representing solutions, shown as $C_{solution}$.

Therefore, the electrical length of the open stub resonator can be written as in equation (6):

$$\theta_s = 2\pi f l_{res}\sqrt{LC_{total}} \tag{6}$$

And the length l_{res} of the open stub resonator was calculated in equation (7) as

$$l_{res} = \frac{\lambda}{4} = \frac{1}{4f\sqrt{LC_{total}}} = \frac{c}{4f\sqrt{\varepsilon_e}} \tag{7}$$

Where λ and f are the operating wavelength and frequency, respectively, C_{total} is the total capacitance of C and $C_{solution}$, c is the speed of light in a vacuum, and $\mathcal{E}_e$ is effective permittivity is approximated in equation (8) by

$$\varepsilon_e = \frac{\varepsilon_r + 1}{2} + \frac{\varepsilon_r - 1}{2}\frac{1}{\sqrt{1 + 12(\frac{h}{W})}} \tag{8}$$

which satisfies $1 < \mathcal{E}_e < \mathcal{E}_r$ and depends on the relative permittivity ($\mathcal{E}_r$) and thickness (h) of the substrate, the conductor Width (W), and the frequency (f). The capacitance (C, $C_{solution}$) is a function of effective permittivity.

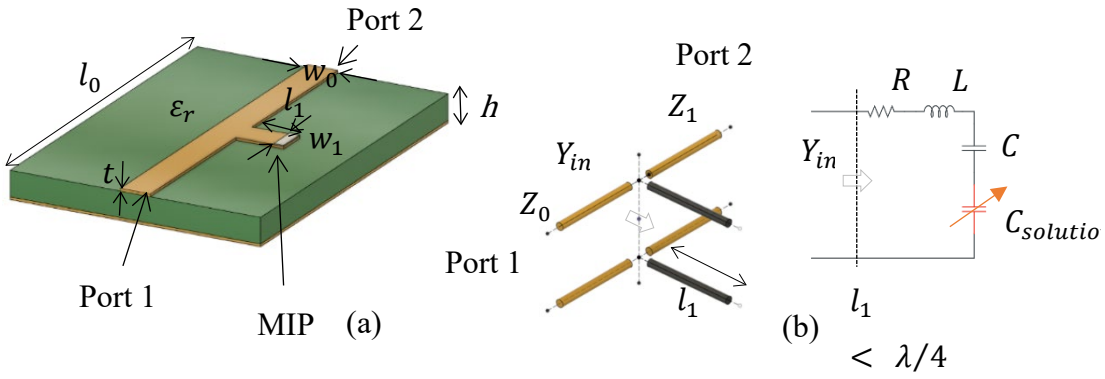

Figure 5. 4 (a) Schematic illustration and (b) Electrical equivalent model of the stub resonator with MIP.

By changing the electromagnetic properties, such as the relative permittivity of the materials constituting or surrounding the resonator, the amount of energy stored in it and its losses can vary dramatically. To measure changes in permittivity due to varying concentrations of glucose, MIP was used as a selective receptor to trap target analytes, and microfluidic channels were incorporated in the sensor where the solutions flowed in, and a change in permittivity was sensed. The variation of concentrations of biomolecules attached to the MIP changes the permittivity, thus resulting in changes in the total capacitance and a shift in the resonant frequency according to equation (7). The microfluidic device enables the water glucose solution to effortlessly pass the sensing area through the channels in the selected region where MIP was coated to study the changes in permittivity.

5.4 Preparation of proposed sensor and Glucose sample preparation

In this section, the MIP and NIP created in chapter 3 are coated on the sensor, as displayed in the Figure 5.5 after the stub resonator has been constructed. In order to deposit MIP and NIP accurately in the desired position (tip of the stub resonator) in sensors, a thin film of Kapton was utilized as a mask, shown in Figure 5.5(a). The microscope image of the uncoated and the MIP-coated biosensor is illustrated in Figure 5.5(b).

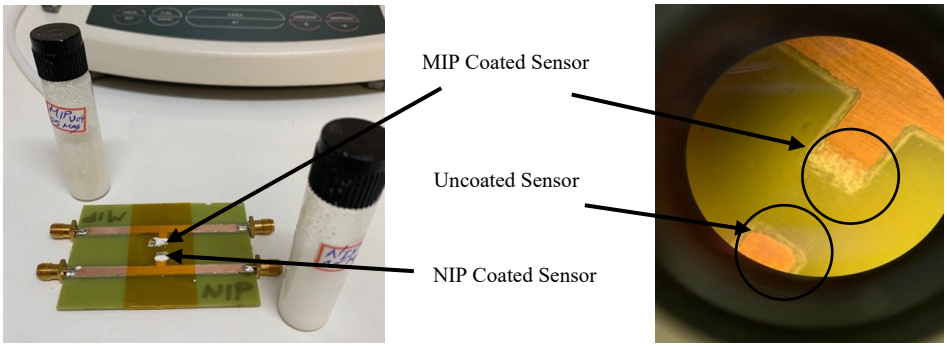

Figure 5. 5 Photograph of (a) First fabricated biosensor with the stub resonators coated with MIP and NIP and (b) Second biosensor coated with MIP and uncoated under the microscope.

A series of 5 water glucose solutions were prepared with glucose concentrations varying between 50 mg/dL and 400 mg/dL. The experiment was performed after the water glucose solutions rested for about 12 hours to establish the anomeric equilibrium. The solutions were measured several times in both sensors (MIP-NIP, and MIP-uncoated): right after resting, 1 h after the first measurement, the subsequent measurement was done after 3 h of rest from the first attempt, and the last measurement was carried out after 24 h of rest. The glucose solutions were pumped one by one through the channel with the aid of a peristaltic pump. While the solution kept flowing continuously at a rate of 5 mL/min in each procedure, three sets of data were collected: right after injecting the solution on sensor, 5 min, and 10 min after the first measurement. After each measurement, DI water was pumped into the channel to wash it and remove absorbed glucose from the MIP. To avoid any shift in the dielectric properties of the glucose solutions, the temperature was maintained constant at 20 ℃.

5.5 Measurement Setup

The performance of the proposed biosensor was characterized in terms of its S-parameters using a performance vector network analyzer (VNA) (N5227B from, Keysight, Santa Rosa, CA, USA) in a two- ports configuration after the SOLT calibration up to 20 GHz. The measurement resolution is 0.1 dB, 1 Hz, and 0.5° in terms of magnitude, frequency, and phase, respectively. The device under test (DUT) was connected to the VNA ports via coaxial cables. All experiments were

carried out under normal laboratory environment conditions. In this experiment, S_{21} scattering parameter was used to characterize the glucose concentration. Figure 5.5(a) and (b) show the fabricated sensing device with injection accesses, and Figure 5.5(c) shows the complete experimental setup for the measurement: VNA, DUT, coaxial probes, pump, and the solutions.

In the process, each time, first, the response of the sensor with an empty flow channel was measured, then the flow channel was filled with DI water continuously as a reference and also to wash the glucose from the MIP between each experiment to verify the reproducibility and repeatability of the study, and finally, filled with solutions with various glucose concentrations. The flow of the solutions was controlled using a pump.

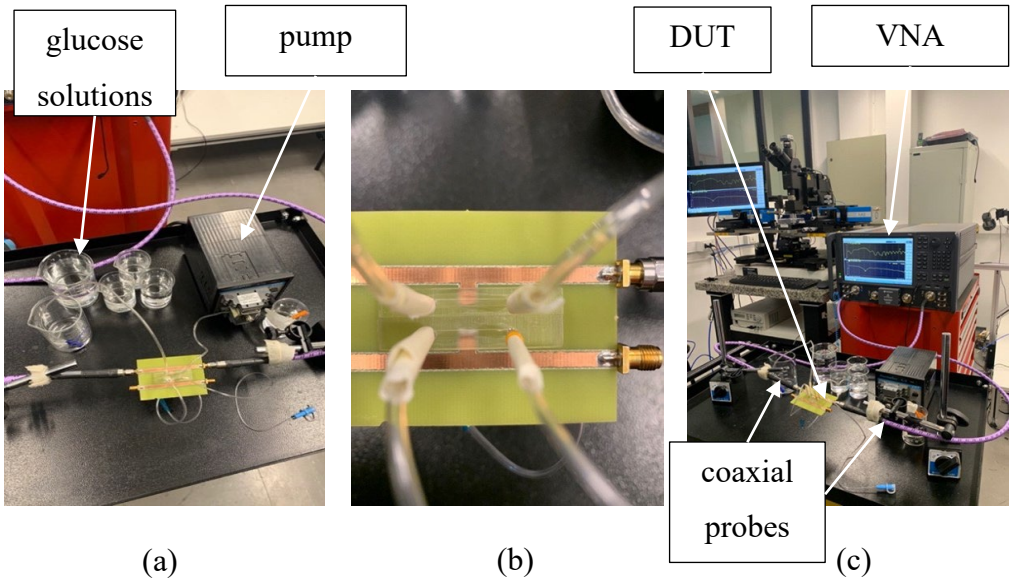

Figure 5. 6 Photograph of (a) solutions and peristaltic pump (b) assembled sensor (c) experimental setup of the sensor with equipment.

5.6 Results

The simulated and measured frequency response of the unloaded sensor (empty flow channel) (in yellow) and the measured frequency response of the loaded flow channel where DI passes the sensing area on top of the stub (in blue) compared to the simulation, up to 10 GHz, are demonstrated in Figure 5.6. The results in both experiments show the agreement between

simulations and measurement is good for the uncoated sensor, which validates the simulation of the sensor's behavior in Ansys.

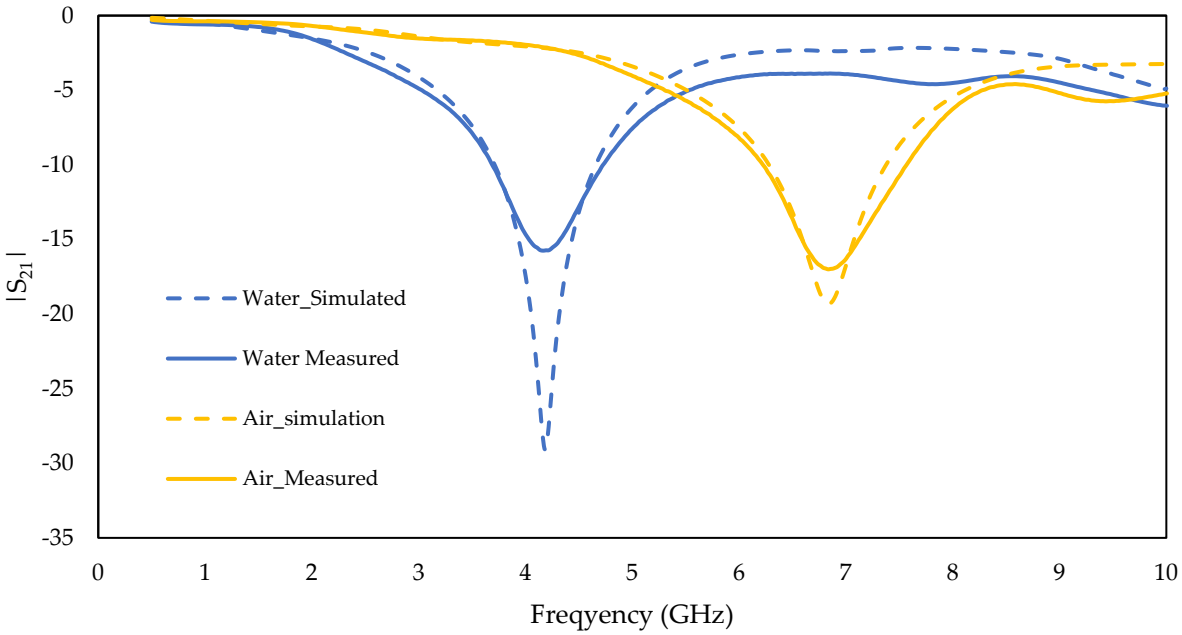

Figure 5. 7 Measured vs. simulated frequency response of the insertion loss (S_{21}) for flow channel filled with air and DI water.

The reflection and transmission coefficients of the MIP-coated biosensor in the frequency range between 2 to 6 GHz are plotted in Figure 5.8. The sensor was exposed to glucose solutions with various concentrations ranging from 50 to 400 mg/dL. A shift towards higher frequencies can be observed in the absorption peak when the glucose content was increased in the solutions.

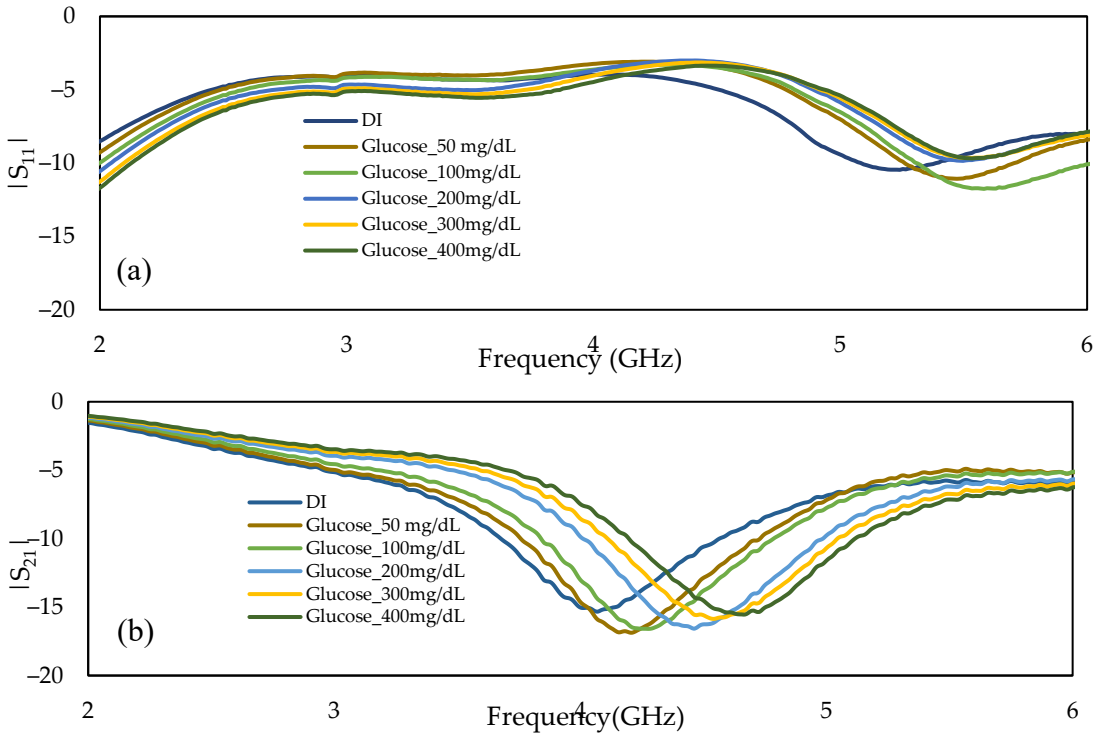

Figure 5. 8 Frequency response of MIP-coated microwave-based stub biosensor (a) Reflection coefficient, $S_{11,}$ and (b) Transmission coefficient, S_{21}.

In this study, we applied the fabricated MIP on two duplicated sensors to validate the performance of the biosensor at several attempts with different masses of MIP. These sensors were tested and the sensitivity in terms of a shift in the absorption peak due to changes in glucose concentrations was verified. Both main and duplicate sensors showed the same behavior in detecting different glucose concentrations in solutions which demonstrated the reproducibility of the sensor, as can be seen in the Frequency response of both main and duplicate senor in Figure 5.9.

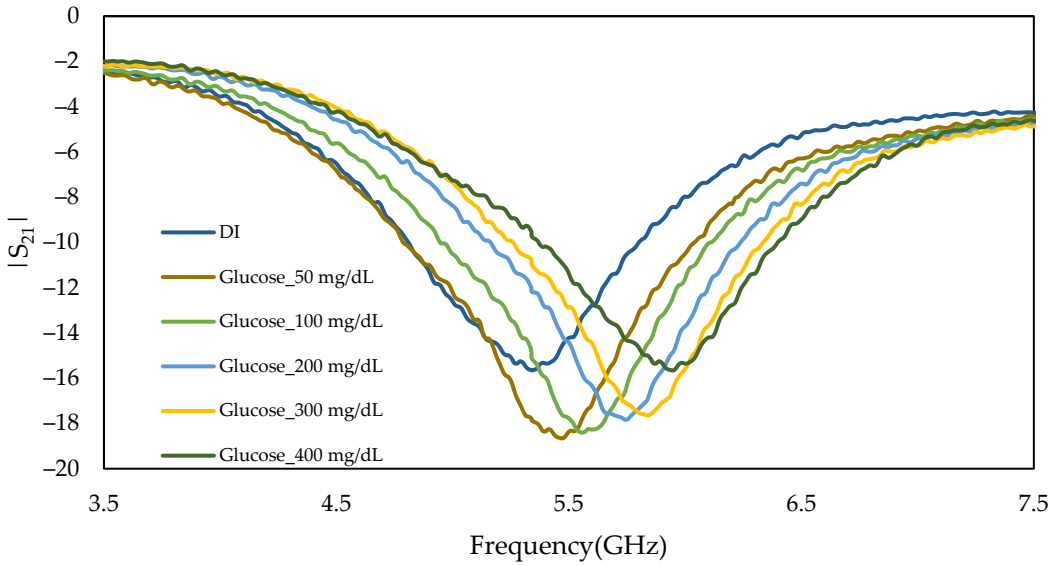

Figure 5. 9 Measured frequency response of the insertion loss (S21) of duplicate MIP-coated microwave-based stub biosensor for the glucose solutions with concentration ranging from 50 mg/dL to 400 mg/dL.

The calibration curves of both main and duplicate MIP-coated sensors were constructed by plotting the absorption peak shift versus the glucose concentrations in Figure 5.9. In addition, the measurements were repeated several times for each sample solution and the results were presented using error bars. A linear relationship between the concentration of glucose and frequency shift can be seen in Figure 5.10, which confirms the behavior of the sensor has the same trend regardless of the mass of MIP.

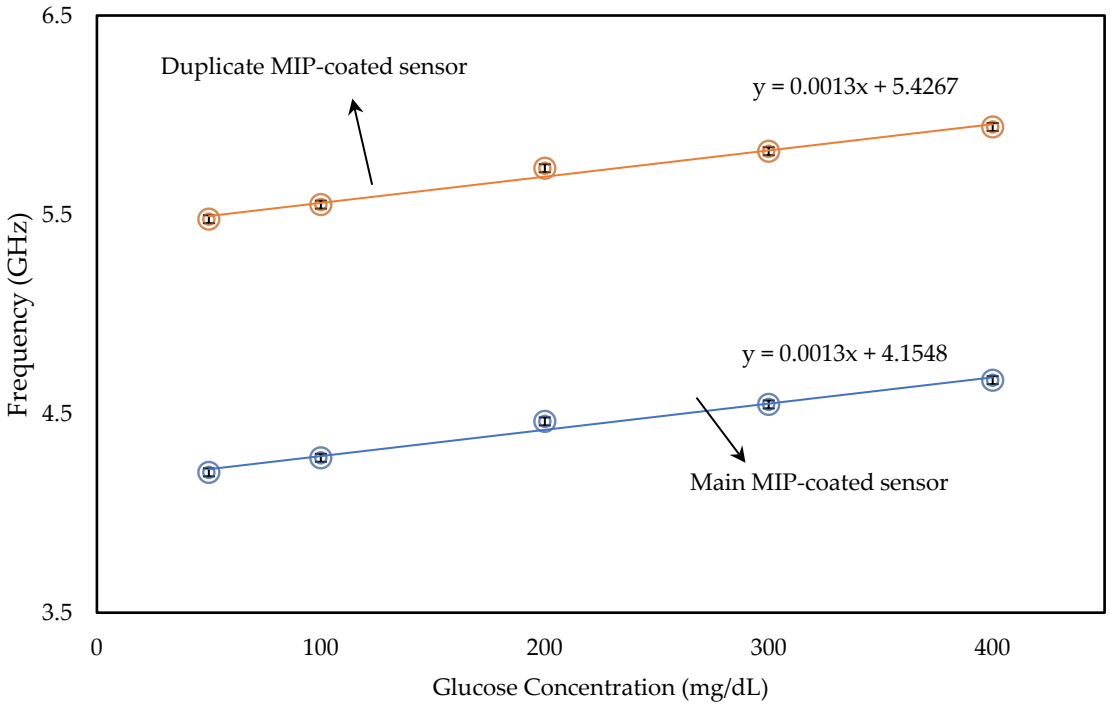

Figure 5. 10 Calibration graph for the main and duplicate MIP-coated microwave-based biosensors exposed to glucose solutions.

In order to verify the proposed sensing principle, the procedure mentioned above was performed in uncoated and NIP-coated stub resonators. A set of measurements were done using the same concentrations of glucose solutions, and the transmitted signal was recorded. As expected, the frequency response of the uncoated and NIP coated sensing devices, in the absence of the template cavities (glucose), did not change with the flow of the same glucose solutions of 100 mg/dL and 400 mg/dL in the flow channel, as demonstrated in Figure 5.11. This finding strongly indicates that measuring the various concentrations of glucose by utilizing a MIP coated biosensor increased the selectivity and, therefore, the detection of glucose levels.

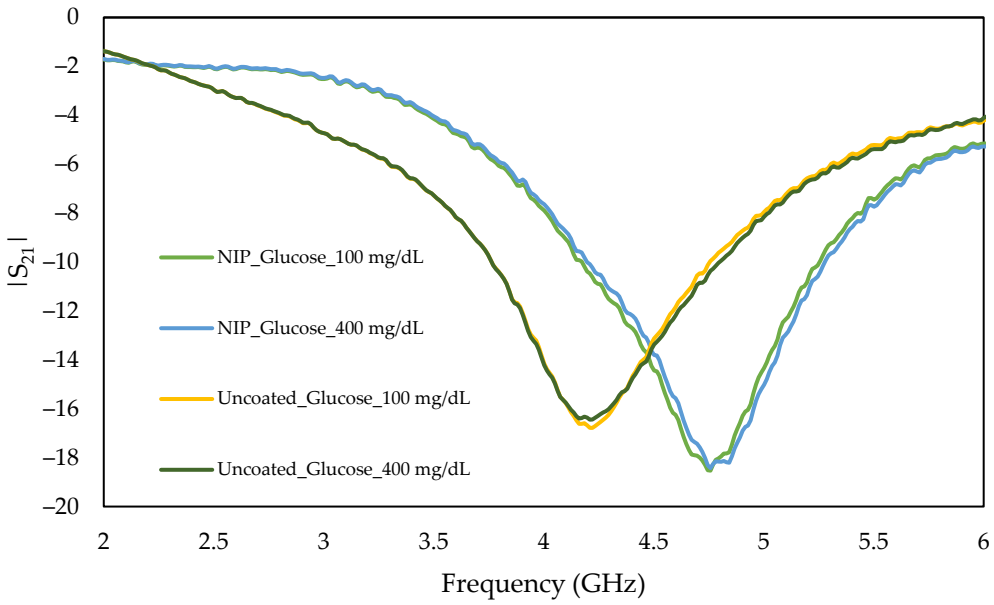

Figure 5. 11 Frequency response of uncoated and NIP-coated microwave-based stub biosensor for the same glucose solutions of 100 mg/dL and 400mg/dL.

To verify the selectivity of the MIP-coated sensor, solutions of glucose and two epimers of glucose, named mannose and galactose, were studied. Figure 5.12 shows the frequency response of 100 mg/dL of glucose, mannose, and galactose solutions. A slight shift in absorption peak can be observed due to the changes in the relative permittivity of the sample solutions.

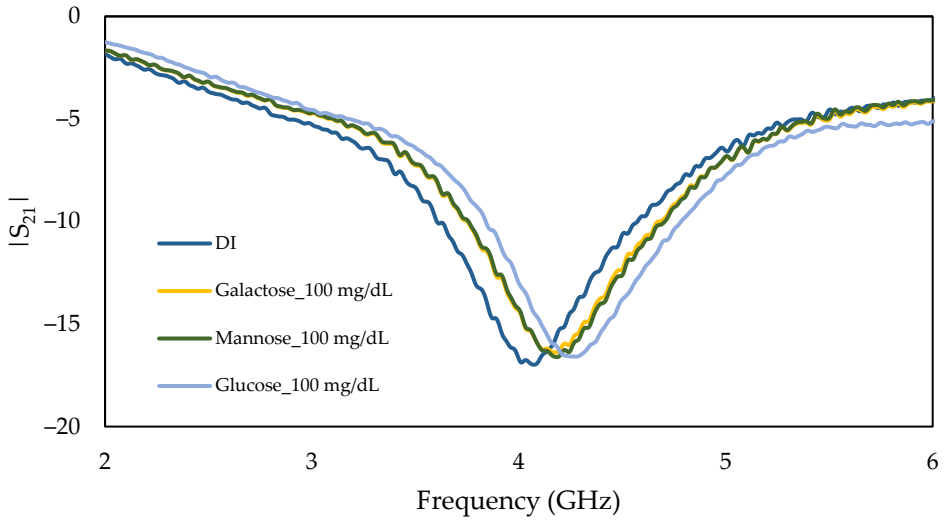

Figure 5. 12 Measured frequency response of the insertion loss (S21) of main MIP-coated microwave-based stub biosensor exposed to 100 mg/dL of glucose, mannose, and galactose solutions.

The experiment was followed by the flow of the mannose and galactose solutions ranging from 100 mg/dL to 300 mg/dL in the channel. The frequency response of the MIP-coated sensor did not change with the flow of the solutions, even by increasing the concentration of the mannose and galactose, as demonstrated in Figure 5.13. This evidenced that our proposed sensor is effectively selective toward glucose than its epimers.

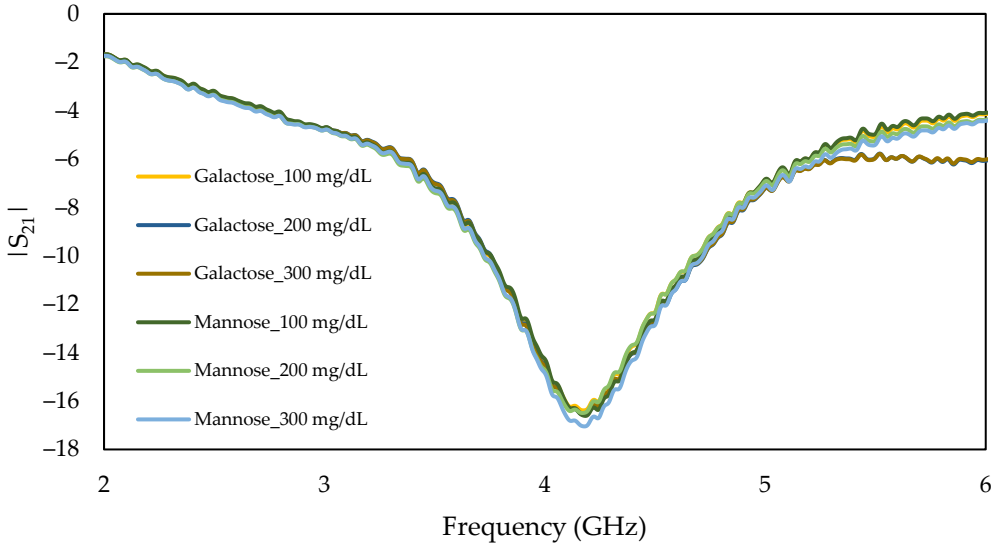

Figure 5. 13 Measured frequency response of the insertion loss (S21) of main MIP-coated microwave-based stub biosensor exposed to mannose and galactose solutions ranging from 100 mg/dL to 300 mg/dL.

Furthermore, to examine the repeatability and stability of the responses, the 100 mg/dL glucose solution was pumped continuously into the flow channel for 75 minutes, and the transmitted signal was recorded at the interval of 15 min. The results on Figure 5.14 show the repeatability and stability of the duplicate MIP-coated sensor with respect to the changes in glucose concentrations in terms of the shift in the resonant frequency (absorption peak). A relative standard deviation (R.S.D.%) of 4.61 was obtained. This indicated that the sensor performs in a repeatable manner which is comparable with the previously reported values of 3.9%–5.6% (Mirmohseni et al., 2014b). As expected, the frequency response does not change during the time.

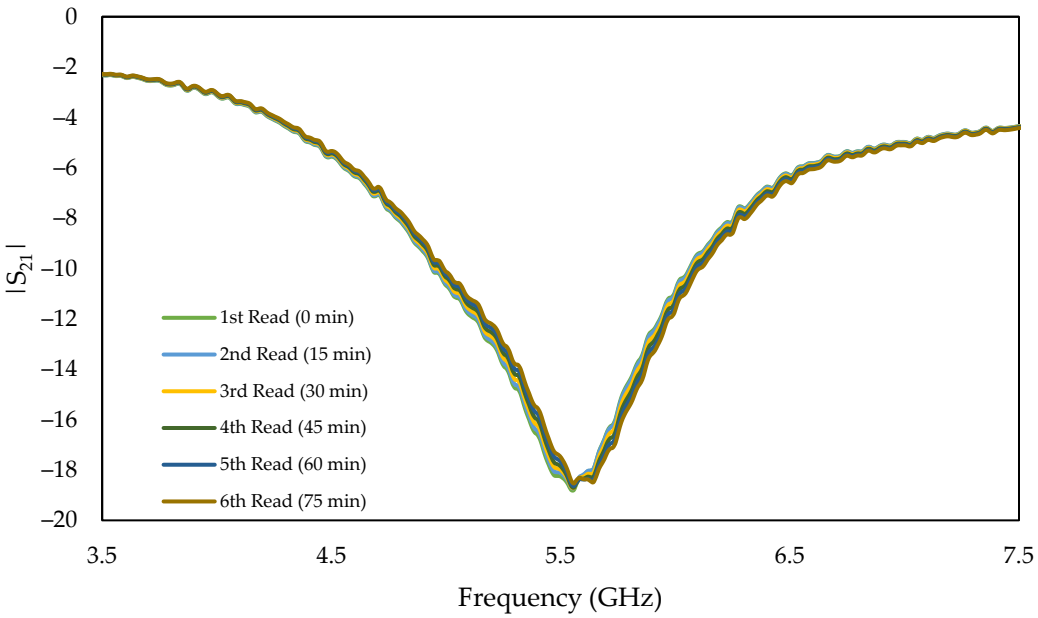

Figure 5. 14 Repeatability and stability test for frequency changes of the duplicate MIP- coated microwave-based stub biosensor: Frequency response exposed to 100 mg/dL glucose solution

Although the studied range of glucose concentrations (50 - 400 mg/dL) covers most of the glucose levels in the human body, the linear response of the proposed biosensor confirmed that solutions with various concentrations can easily be measured after appropriate dilution. Table 5.1 shows the summary of analytical parameters of the proposed biosensor in the studied range of glucose concentrations. To understand the extent of imprinting and explicitness of prepared MIP, the imprinting factor was presented in equation (9), which was calculated by dividing the frequency shift response of MIP ($\Delta f_{MIP} \cong 134\ MHz$ from Figure 5.7 (b)) by the frequency shift response of NIP ($\Delta f_{NIP} \cong 12\ MHz$ from Figure 5.11). In proposed MIP-coated glucose sensor, the imprinting factor of MIP is 11 times higher than that of NIP.

$$IF = \frac{\Delta f_{MIP}}{\Delta f_{NIP}} = 11 \tag{9}$$

Table 5. 1 Analytical parameters of sensing device coated with MIP

[a]R^2	**Sensitivity Factor** (MHz/mg dL^{-1})	[b]**LLD** (ng dL^{-1})	[c]**RSD %**	**Imprinting Factor**
0.9839	1.3	2.4	4.61	11

a Square Correlation Coefficient

b Lower Limit of Detection

c Relative Standard Déviation

5.7 Discussion

Blood glucose level measurement is a challenging task, and there are many factors affecting measurement accuracy that need to be considered when a real-life glucose range measurement is concerned. Table 5.2 summarizes the experimental results of glucose measuring sensors using planar transmission lines stated in the literature and that of our proposed sensor. The studied frequency and concentration ranges and the aver-age sensitivity values with respect to the concentration range for each sensor are also presented in this table. Almost any sensor in the literature shows a frequency shift for different concentrations of glucose, however most of them investigate unrealistic glucose levels. Indeed, in most cases, including (Shahri, Omidvar, Rehder, Serrano, et al., 2021), researchers eliminate the biomarker to measure glucose level. However, the result may not be suitable for real-life blood glucose level measurement since they ignore the effect of other physiological parameters and bioanalyses; hence their selectivity is ambiguous. On the other hand, the enzyme base biomarkers, as in (Camli et al., 2017),(Camli et al., 2016a), give certain confidence that the results are related to the glucose concentration. Still, they are not real-time and less sensitive due to the chemical reaction between glucose and enzyme and insufficient stability. Research shows the relative shift of frequency in the presence of GOD occurs within 25 minutes for glucose to reach the saturation level.

Table 5. 2 Comparison with the state-of-the-art the MIP- coated microwave-based biosensor

Ref.	Sensor Type	Sample Volume (μL)	Glucose Concentration (mg/dL)	Nonloaded f_r (GHz)	Operating f_r (GHz)	Sensitivity f_r (MHz per mg/dL)	R^2	Remarks
(Camli et al., 2017)	Single SRR	90μL	0-50000	1.83	1.49	$0.107 * 10^{-2}$	0.79	Enzyme-coated
(Camli et al., 2016b)	Single SRR	90μL	0-40000	1.82	1.59	$0.174 * 10^{-2}$	0.93	Enzyme-coated
(Shahri et al., 2021)	MLIN	160μL	100-300 1000-8000	-	4.8–5.7	$32*10^{-2}$ $3.2*10^{-2}$	0.98	Non-Enzyme
This work	**Stub Resonator**	**40μL**	**0 - 400**	**7**	**4.4**	**1.3**	**0.9839**	**MIP-coated**

Chapter 6: Conclusion and Future work

The proposed MIP-coated open stub resonator biosensor is developed as an inexpensive and sensitive sensing device that detects variation in glucose concentration in the solution by measuring shifts in the absorption peak. Acrylic acid (AA) is selected as a suitable functional monomer, and 4,4′-Azobis (4-cyanopentanoic acid) (ACPA) is chosen as a fast initiator. Furthermore, the frequency response of the stub resonator shifts due to the varying glucose concentrations, which demonstrates an excellent linear correlation ($R^2 = 0.9839$) within the range of 50 – 400 mg/dL, while the lower limit of detection (LLD) of the sensor is discovered to be 2.4 ng/dL. Our sensing device differentiates the glucose variation regardless of the mass of MIP and is effectively selective toward glucose compared to similar compounds. In addition, it requires a small volume of samples (40 μL) and is highly sensitive (1.3 MHz/(mg/dL)) compared to other similar approaches. This capacity will help us to miniaturize the sensor. Moreover, the combination of molecularly imprinted technology and a microwave resonator that can be fabricated easily at a low cost, provides the opportunity to make a passive and battery-less sensing device for point-of-care monitoring purposes.

The glucose sensor design can be improved to increase sensitivity and selectivity for sensing glucose concentration. The sensitivity of the biosensor can also be enhanced using the FBAR and microstrip design similarly. Consequently, it is possible to optimize the design and architecture of biosensors. Another task that the optimization process suggests is size reduction. Less sample volume will be needed if the biosensor is miniature. Studying the functionality of new substrate materials is possible. Biorecognition components can be used to increase selectivity, which will result in a more effective bio-detection. It is advised that future studies examine blood glucose levels in patients with various forms of diabetes to examine the impact of other physiological processes. It is also possible to study various kinds of biomolecules.

References

Alsaad, A. M., Al-Bataineh, Q. M., Qattan, I. A., Ahmad, A. A., Ababneh, A., Albataineh, Z., Aljarrah, I. A., & Telfah, A. (2020). Measurement and ab initio Investigation of Structural, Electronic, Optical, and Mechanical Properties of Sputtered Aluminum Nitride Thin Films. *Frontiers in Physics*, *8*, 115. https://doi.org/10.3389/FPHY.2020.00115/BIBTEX

Alvarez-Lorenzo, C., & Concheiro, A. (2004). Molecularly imprinted polymers for drug delivery. *Journal of Chromatography B: Analytical Technologies in the Biomedical and Life Sciences*, *804*(1), 231–245. https://doi.org/10.1016/j.jchromb.2003.12.032

Armas Alvarado, M. E. (2017). *Produção e caracterização de filmes de nitreto de alumínio e sua aplicação em guias de onda tipo pedestal.* https://doi.org/10.11606/T.3.2017.TDE-12072017-085316

Association, A. D. (2010). Diagnosis and Classification of Diabetes Mellitus. *Diabetes Care*, *33*(Supplement_1), S62–S69. https://doi.org/10.2337/DC10-S062

Association, A. D. (2019). 2. Classification and Diagnosis of Diabetes: Standards of Medical Care in Diabetes—2019. *Diabetes Care*, *42*(Supplement_1), S13–S28. https://doi.org/10.2337/DC19-S002

Auer, S., Nirschl, M., Schreiter, M., & Vikholm-Lundin, I. (2011). Detection of DNA hybridisation in a diluted serum matrix by surface plasmon resonance and film bulk acoustic resonators. *Analytical and Bioanalytical Chemistry*, *400*(5), 1387–1396. https://doi.org/10.1007/S00216-011-4871-0/FIGURES/5

Ayala, V. C., Moosmann, K., Prucker, O., Rühe, J., & Reindl, L. M. (2009). Chemical modification of surfaces for biochemical and medical sensor applications. *IFMBE Proceedings*, *25*(8), 339–342. https://doi.org/10.1007/978-3-642-03887-7_98/COVER

Baggiani, C., Anfossi, L., & Giovannoli, C. (2007). Solid phase extraction of food contaminants using molecular imprinted polymers. *Analytica Chimica Acta*, *591*(1), 29–39. https://doi.org/10.1016/J.ACA.2007.01.056

Bakhtiar, S., Bhawani, S. A., & Shafqat, S. R. (2019). Synthesis and characterization of molecular imprinting polymer for the removal of 2-phenylphenol from spiked blood serum and river water. *Chemical and Biological Technologies in Agriculture*, *6*(1), 1–10. https://doi.org/10.1186/S40538-019-0152-5/TABLES/5

Ballantine, D. S., Martin, S. J., Ricco, A. J., Frye, G. C., Wohltjen, H., White, R. M., & Zellers, E. T. (1997). Structure Monomer. In *Acoustic Wave Sensors: Theory, Design, and Physico-Chemical Applications* (Vol. 2). http://www.sciencedirect.com:5070/book/9780120774609/acoustic-wave-sensors

Boutati, E. I., & Raptis, S. A. (2009). Self-monitoring of blood glucose as part of the integral care of type 2 diabetes. *Diabetes Care*, *32 Suppl 2*(Suppl 2). https://doi.org/10.2337/DC09-S312

Camli, B., Kusakci, E., Lafci, B., Salman, S., Torun, H., & Yalcinkaya, A. (2016a). A Microwave Ring Resonator Based Glucose Sensor. *Procedia Engineering*, *168*, 465–468. https://doi.org/10.1016/J.PROENG.2016.11.127

Camli, B., Kusakci, E., Lafci, B., Salman, S., Torun, H., & Yalcinkaya, A. (2016b). A Microwave Ring Resonator Based Glucose Sensor. *Procedia Engineering*, *168*, 465–468. https://doi.org/10.1016/J.PROENG.2016.11.127

Camli, B., Kusakci, E., Lafci, B., Salman, S., Torun, H., & Yalcinkaya, A. D. (2017). Cost-effective, microstrip antenna driven ring resonator microwave biosensor for biospecific detection of glucose. *IEEE Journal of Selected Topics in Quantum Electronics*, *23*(2), 404–409. https://doi.org/10.1109/JSTQE.2017.2659226

Carneiro, J. M. T., Dias, A. C. B., Zagatto, E. A. G., Santos, J. L. M., & Lima, J. L. F. C. (2005). An improved sampling approach in multi-pumping flow systems applied to the spectrophotometric determination of glucose and fructose in syrups. *Analytica Chimica Acta*, *531*(2), 279–284. https://doi.org/10.1016/J.ACA.2004.10.038

Cass, A. E. G., Davis, G., Francis, G. D., Allen, H., Hill, O., Aston, W. J., Higgins, I. J., Plotkin, E. V., Scott, L. D. L., & Turner, A. P. F. (1984). Ferrocene-Mediated Enzyme Electrode for Amperometric Determination of Glucose. *Analytical Chemistry*, *56*(4), 667–671. https://doi.org/10.1021/AC00268A018/ASSET/AC00268A018.FP.PNG_V03

Chen, M., Cai, W. P., Zhu, Q. Z., Wang, X. S., & Xu, J. G. (1999). Determination of glucose based on the effect of photons as a substitute for glucose oxidase. *Analytica Chimica Acta*, *388*(1–2), 11–17. https://doi.org/10.1016/S0003-2670(99)00130-0

Chretiennot, T., Dubuc, D., & Grenier, K. (2014). Double stub resonant biosensor for glucose concentrations quantification of multiple aqueous solutions. *IEEE MTT-S International Microwave Symposium Digest*. https://doi.org/10.1109/MWSYM.2014.6848570

Chuma, E. L., Iano, Y., Fontgalland, G., & Bravo Roger, L. L. (2018). Microwave sensor for liquid dielectric characterization based on metamaterial complementary split ring resonator. *IEEE Sensors Journal*, *18*(24), 9978–9983. https://doi.org/10.1109/JSEN.2018.2872859

Cicek, A., Trak, D., Arslan, Y., Korozlu, N., Kaya, O. A., & Ulug, B. (2019). Ultrasonic Gas Sensing by Two-Dimensional Surface Phononic Crystal Ring Resonators. *ACS Sensors*, *4*(7), 1761–1765. https://doi.org/10.1021/ACSSENSORS.9B00865/SUPPL_FILE/SE9B00865_SI_001.PDF

Clark, L. C., & Lyons, C. (1962). Electrode systems for continuous monitoring in cardiovascular surgery. *Annals of the New York Academy of Sciences*, *102*(1), 29–45. https://doi.org/10.1111/J.1749-6632.1962.TB13623.X

Costanzo, S. (2017). Non-invasive microwave sensors for biomedical applications: New design perspectives. *Radioengineering*, *26*(2), 406–410. https://doi.org/10.13164/RE.2017.0406

Dai, S., Shin, Y. S., Barnes, C. E., & Toth, L. M. (1997). Enhancement of Uranyl Adsorption Capacity and Selectivity on Silica Sol−Gel Glasses via Molecular Imprinting. *Chemistry of Materials*, *9*(11), 2521–2525. https://doi.org/10.1021/CM970209K

de Fonseca, B., Rossignol, J., Stuerga, D., & Pribetich, P. (2015). Microwave signature for gas sensing: 2005 to present. *Urban Climate*, *14*, 502–515. https://doi.org/10.1016/J.UCLIM.2014.10.010

Dehdashtian, S., & Hashemi, B. (2019). Voltammetric sensing of minoxidil using a molecularly imprinted polymer (MIP)-modified carbon paste electrode. *Chemical Papers 2019 74:1*, *74*(1), 157–165. https://doi.org/10.1007/S11696-019-00860-4

DeMiguel-Ramos, M., Díaz-Durán, B., Escolano, J. M., Barba, M., Mirea, T., Olivares, J., Clement, M., & Iborra, E. (2017). Gravimetric biosensor based on a 1.3 GHz AlN shear-mode solidly mounted resonator. *Sensors and Actuators B: Chemical*, *239*, 1282–1288. https://doi.org/10.1016/J.SNB.2016.09.079

Ding, S., Lyu, Z., Niu, X., Zhou, Y., Liu, D., Falahati, M., Du, D., & Lin, Y. (2020). Integrating ionic liquids with molecular imprinting technology for biorecognition and biosensing: A review. *Biosensors and Bioelectronics*, *149*, 111830. https://doi.org/10.1016/J.BIOS.2019.111830

DOMB, A. J. (1996). *PREPARATION OF BIOLOGICALLY ACTIVE MOLECULES BY MOLECULAR IMPRINTING*.

Ebrahimi, A., Scott, J., & Ghorbani, K. (2020). Microwave reflective biosensor for glucose level detection in aqueous solutions. *Sensors and Actuators A: Physical*, *301*, 111662. https://doi.org/10.1016/J.SNA.2019.111662

Engineering of Micro/Nano Biosystems | INSIS. (n.d.). Retrieved December 5, 2022, from https://www.insis.cnrs.fr/fr/engineering-micronano-biosystems

Figueiredo, L., Erny, G. L., Santos, L., & Alves, A. (2016). Applications of molecularly imprinted polymers to the analysis and removal of personal care products: A review. *Talanta*, *146*, 754–765. https://doi.org/10.1016/J.TALANTA.2015.06.027

Frew, J. E., & Hill, H. A. O. (1987). Electrochemical Biosensors. *Analytical Chemistry*, *59*(15), 933–944. https://doi.org/10.1021/AC00142A001/ASSET/AC00142A001.FP.PNG_V03

Fu, Y. Q., Luo, J. K., Nguyen, N. T., Walton, A. J., Flewitt, A. J., Zu, X. T., Li, Y., McHale, G., Matthews, A., Iborra, E., Du, H., & Milne, W. I. (2017). Advances in piezoelectric thin films for acoustic biosensors, acoustofluidics and lab-on-chip applications. *Progress in Materials Science*, *89*, 31–91. https://doi.org/10.1016/J.PMATSCI.2017.04.006

Galsin, J. S. (2019). Crystal Structure of Solids. *Solid State Physics*, 1–36. https://doi.org/10.1016/B978-0-12-817103-5.00001-3

García-Baños, B., Cuesta-Soto, F., Griol, A., Catalá-Civera, J. M., & Pitarch, J. (2006). Enhancement of sensitivity of microwave planar sensors with EBG structures. *IEEE Sensors Journal*, *6*(6), 1518–1522. https://doi.org/10.1109/JSEN.2006.884506

García-Gancedo, L., Al-Naimi, F., Flewitt, A. J., Milne, W. I., Ashley, G. M., Luo, J. K., Zhao, X., & Lu, J. R. (2011). ZnO-based FBAR resonators with carbon nanotube electrodes. *IEEE Transactions on Ultrasonics, Ferroelectrics, and Frequency Control*, *58*(11), 2438–2445. https://doi.org/10.1109/TUFFC.2011.2100

Garcia-Gancedo, L., Pedros, J., Flewitt, A. J., Milne, W. I., Ashley, G. M., Luo, J., & Ford, C. J. B. (2010). Ultrafast sputtered ZnO thin films with high kT for acousticwave device applications. *Proceedings - IEEE Ultrasonics Symposium*, 1064–1067. https://doi.org/10.1109/ULTSYM.2010.5935455

García-Gancedo, L., Pedrós, J., Iborra, E., Clement, M., Zhao, X. B., Olivares, J., Capilla, J., Luo, J. K., Lu, J. R., Milne, W. I., & Flewitt, A. J. (2013). Direct comparison of the gravimetric responsivities of ZnO-based FBARs and SMRs. *Sensors and Actuators B: Chemical*, *183*, 136–143. https://doi.org/10.1016/J.SNB.2013.03.085

Ge, Y., & Turner, A. P. F. (2009). Molecularly imprinted sorbent assays: recent developments and applications. *Chemistry (Weinheim an Der Bergstrasse, Germany)*, *15*(33), 8100–8107. https://doi.org/10.1002/CHEM.200802401

Giangu, I., Stavrinidis, G., Stefanescu, A., Stavrinidis, A., Dinescu, A., Konstantinidis, G., & Muller, A. (2015). Pressure sensors based on high frequency operating GaN FBARs. *Proceedings of the International Semiconductor Conference, CAS*, *2015-December*, 99–102. https://doi.org/10.1109/SMICND.2015.7355174

Gudkov, A. G., Ivanov, Y. A., Meshkov, S. A., Agasieva, S. V., Petrov, V. I., Sinyakin, V. Y., & Schukin, S. I. (2015). Prospects for Application of Radio-Frequency Identification Technology with Passive Tags in Invasive Biosensor Systems. *Biomedical Engineering 2015 49:2*, *49*(2), 98–101. https://doi.org/10.1007/S10527-015-9506-X

Guha, S., Jamal, F. I., & Wenger, C. (2017). A Review on Passive and Integrated Near-Field Microwave Biosensors. *Biosensors*, *7*(4). https://doi.org/10.3390/BIOS7040042

Haginaka, J. (2008). Monodispersed, molecularly imprinted polymers as affinity-based chromatography media. *Journal of Chromatography. B, Analytical Technologies in the Biomedical and Life Sciences*, *866*(1–2), 3–13. https://doi.org/10.1016/J.JCHROMB.2007.07.019

Hallil, H., Bahoumina, P., Pieper, K., Lachaud, J. L., Rebiere, D., Abdelghani, A., Frigui, K., Bila, S., Baillargeat, D., Zhang, Q., Coquet, P., Pichonat, E., Happy, H., & Dejous, C. (2019). Differential passive microwave planar resonator-based sensor for chemical particle detection in polluted environments. *IEEE Sensors Journal*, *19*(4), 1346–1353. https://doi.org/10.1109/JSEN.2018.2881487

Haynes, W. M. (2016). Hanbook of chemistery and phisics. *Journal of Experimental Psychology: General*, *136*(1), 2652.

He, X. F., Liu, X., Yin, X. F., Wen, Z. Y., & Chen, K. W. (2011). Active control scheme for improving mass resolution of film bulk acoustic resonators. *Applied Mathematics and Mechanics (English Edition)*, *32*(6), 749–756. https://doi.org/10.1007/S10483-011-1454-9/METRICS

Heller, A., & Feldman, B. (2008). Electrochemical glucose sensors and their applications in diabetes management. *Chemical Reviews*, *108*(7), 2482–2505.

https://doi.org/10.1021/CR068069Y/ASSET/IMAGES/LARGE/CR-2006-08069Y_0001.JPEG

Hillberg, A. L., Brain, K. R., & Allender, C. J. (2005). Molecular imprinted polymer sensors: implications for therapeutics. *Advanced Drug Delivery Reviews*, *57*(12), 1875–1889. https://doi.org/10.1016/J.ADDR.2005.07.016

Hjertén, S., Liao, J. L., Nakazato, K., Wang, Y., Zamaratskaia, G., & Zhang, H. X. (1997). Gels mimicking antibodies in their selective recognition of proteins. *Chromatographia 1997 44:5*, *44*(5), 227–234. https://doi.org/10.1007/BF02466386

Hornyak, R., Lewis, M., & Sankaranarayan, B. (2016). Radio frequency identification-enabled capabilities in a healthcare context: An exploratory study. *Health Informatics Journal*, *22*(3), 562–578. https://doi.org/10.1177/1460458215572923

Huang, Q. A., Dong, L., & Wang, L. F. (2016). LC Passive Wireless Sensors Toward a Wireless Sensing Platform: Status, Prospects, and Challenges. *Journal of Microelectromechanical Systems*, *25*(5), 822–841. https://doi.org/10.1109/JMEMS.2016.2602298

Huang, S. Y., Omkar, Yoshida, Y., Inda, A. J. G., Xavier, C. X., Mu, W. C., Meng, Y. S., & Yu, W. (2019). Microstrip Line-Based Glucose Sensor for Noninvasive Continuous Monitoring Using the Main Field for Sensing and Multivariable Crosschecking. *IEEE Sensors Journal*, *19*(2), 535–547. https://doi.org/10.1109/JSEN.2018.2877691

International Diabetes Federation. (2019). IDF Diabetes Atlas. *9th Edn. Brussels,*. https://www.diabetesatlas.org

Jiao, X., Shi, Y., Zhong, H., Zhang, R., & Yang, J. (2015). AlN thin films deposited on different Si-based substrates through RF magnetron sputtering. *Journal of Materials Science: Materials in Electronics*, *26*(2), 801–808. https://doi.org/10.1007/s10854-014-2467-0

Kamohara, T., Akiyama, M., & Kuwano, N. (2008). Influence of molybdenum bottom electrodes on crystal growth of aluminum nitride thin films. *Journal of Crystal Growth*, *310*(2), 345–350. https://doi.org/10.1016/j.jcrysgro.2007.10.033

Kanno, S., Yanagida, Y., Haruyama, T., Kobatake, E., & Aizawa, M. (2000). Assembling of engineered IgG-binding protein on gold surface for highly oriented antibody immobilization. *Journal of Biotechnology*, *76*(2–3), 207–214. https://doi.org/10.1016/S0168-1656(99)00186-8

Kim, H. Y., Kim, K. B., Cho, S. H., & Kim, Y. Il. (2012). Analysis of resonance characteristics of Bragg reflector type film bulk acoustic resonator. *Surface and Coatings Technology*, *211*, 143–147. https://doi.org/10.1016/j.surfcoat.2011.10.032

Krishnaswamy, S. V., Rosenbaum, J., Horwitz, S., Vale, C., & Moore, R. A. (1990). Film bulk acoustic wave resonator technology. *Ultrasonics Symposium Proceedings*, *1*, 529–536. https://doi.org/10.1109/ultsym.1990.171421

Krudpun, W., Chudpooti, N., Lorwongtragool, P., Seewattanapon, S., & Akkaraekthalin, P. (2019). PSE-Coated Interdigital Resonator for Selective Detection of Ammonia Gas Sensor. *IEEE Sensors Journal*, *19*(23), 11228–11235. https://doi.org/10.1109/JSEN.2019.2936102

Lasáková, M., & Jandera, P. (2009). Molecularly imprinted polymers and their application in solid phase extraction. *Journal of Separation Science*, *32*(5–6), 799–812. https://doi.org/10.1002/JSSC.200800506

Li, J., & Lin, X. (2007). Glucose biosensor based on immobilization of glucose oxidase in poly(o-aminophenol) film on polypyrrole-Pt nanocomposite modified glassy carbon electrode. *Biosensors and Bioelectronics*, *22*(12), 2898–2905. https://doi.org/10.1016/j.bios.2006.12.004

Li, L., & Uttamchandani, D. (2009). A microwave dielectric biosensor based on suspended distributed MEMS transmission lines. *IEEE Sensors Journal*, *9*(12), 1825–1830. https://doi.org/10.1109/JSEN.2009.2031388

Li, W., & Li, S. (2007). Molecular imprinting: A versatile tool for separation, sensors and catalysis. *Advances in Polymer Science*, *206*(1), 191–210. https://doi.org/10.1007/12_2006_105/COVER

Link, M., Weber, J., Schreiter, M., Wersing, W., Elmazria, O., & Alnot, P. (2007). Sensing characteristics of high-frequency shear mode resonators in glycerol solutions. *Sensors and Actuators B: Chemical*, *121*(2), 372–378. https://doi.org/10.1016/J.SNB.2006.03.055

Liu Jie, & Wang Joseph. (2001). A Novel Improved Design for the First-generation Glucose Biosensor. *Food Technology and Biotechnology* , 39. https://www.researchgate.net/publication/266499340_A_Novel_Improved_Design_for_the_First-generation_Glucose_Biosensor/citations

Longo, L., & Vasapollo, G. (2008a). Molecularly Imprinted Polymers as Nucleotide Receptors. *Mini-Reviews in Organic Chemistry*, *5*(3), 163–170. https://doi.org/10.2174/157019308785161620

Longo, L., & Vasapollo, G. (2008b). Phthalocyanine-based molecularly imprinted polymers as nucleoside receptors. *Metal-Based Drugs*, *2008*. https://doi.org/10.1155/2008/281843

Ma, Y. L., Ke, H., Valkonen, A., Rissanen, K., & Jiang, W. (2018). Achieving Strong Positive Cooperativity through Activating Weak Non-Covalent Interactions. *Angewandte Chemie International Edition*, *57*(3), 709–713. https://doi.org/10.1002/ANIE.201711077

Makkonen, T., Holappa, A., Ellä, J., & Salomaa, M. M. (2001). Finite element simulations of thin-film composite BAW resonators. *IEEE Transactions on Ultrasonics, Ferroelectrics, and Frequency Control*, *48*(5), 1241–1258. https://doi.org/10.1109/58.949733

Marlene C Morris, Howard F. McMurdie, & et al. (1981). *Standard X-ray Diffraction Powder Patterns*.

Mehrotra, P., Chatterjee, B., & Sen, S. (2019). EM-Wave Biosensors: A Review of RF, Microwave, mm-Wave and Optical Sensing. *Sensors 2019, Vol. 19, Page 1013*, *19*(5), 1013. https://doi.org/10.3390/S19051013

Mirmohseni, A., Pourata, R., & Shojaei, M. (2014a). Application of molecularly imprinted polymer for determination of glucose by quartz crystal nanobalance technique. *IEEE Sensors Journal*, *14*(8), 2807–2812. https://doi.org/10.1109/JSEN.2014.2316819

Mirmohseni, A., Pourata, R., & Shojaei, M. (2014b). Application of molecularly imprinted polymer for determination of glucose by quartz crystal nanobalance technique. *IEEE Sensors Journal*, *14*(8), 2807–2812. https://doi.org/10.1109/JSEN.2014.2316819

Moad, G., Rizzardo, E., & Solomon, D. H. (1989). Other Initiating Systems. *Comprehensive Polymer Science and Supplements*, 141–146. https://doi.org/10.1016/B978-0-08-096701-1.00072-0

Moutaouekkil, M., Talbi, A., El Boudouti, E. H., Elmazria, O., Djafari-Rouhani, B., Pernod, P., & Bou Matar, O. (2019). Highly confined radial contour modes in phononic crystal plate based on pillars with cap layers. *Journal of Applied Physics*, *126*(5), 055101. https://doi.org/10.1063/1.5099956

Nagaraju, M., Gu, J., Lingley, A., Zhang, F., Small, M., Ruby, R., & Otis, B. (2014). A fully integrated wafer-scale sub-mm3 FBAR-based wireless mass sensor. *IFCS 2014 - 2014 IEEE International Frequency Control Symposium, Proceedings*. https://doi.org/10.1109/FCS.2014.6859916

Nirschl, M., Blüher, A., Erler, C., Katzschner, B., Vikholm-Lundin, I., Auer, S., Vörös, J., Pompe, W., Schreiter, M., & Mertig, M. (2009). Film bulk acoustic resonators for DNA and protein detection and investigation of in vitro bacterial S-layer formation. *Sensors and Actuators A: Physical*, *156*(1), 180–184. https://doi.org/10.1016/J.SNA.2009.02.021

Noncommunicable diseases. (n.d.). Retrieved May 30, 2022, from https://www.who.int/news-room/fact-sheets/detail/noncommunicable-diseases

Opik, A., Menaker, A., Reut, J., & Syritski, V. (2009). Molecularly imprinted polymers: a new approach to the preparation of functional materials/molekulaarselt jaljendatud polumeerid--uus valjund funktsionaalsete materjalide valmistamiseks. *Proceedings of the Estonian Academy of Sciences*, *58*(1), 3–12.

https://go.gale.com/ps/i.do?p=AONE&sw=w&issn=17366046&v=2.1&it=r&id=GALE%7CA199194680&sid=googleScholar&linkaccess=fulltext

Palmisano, F., Zambonin, P. G., Centonze, D., & Quinto, M. (2002). A disposable, reagentless, third-generation glucose biosensor based on overoxidized poly(pyrrole)/tetrathiafulvalene-tetracyanoquinodimethane composite. *Analytical Chemistry*, *74*(23), 5913–5918. https://doi.org/10.1021/AC0258608

Pan, J., Chen, W., Ma, Y., & Pan, G. (2018). Molecularly imprinted polymers as receptor mimics for selective cell recognition. *Chemical Society Reviews*, *47*(15), 5574–5587. https://doi.org/10.1039/C7CS00854F

Panda, P., Mantry, S., Mohapatra, S., Singh, S. K., & Satapathy, A. (2014). A study on erosive wear analysis of glass fiber-epoxy-AlN hybrid composites. *Journal of Composite Materials*, *48*(1), 107–118. https://doi.org/10.1177/0021998312469239

Pang, W., Zhang, M., & Liang, J. (2017). *Piezoelectric Micro/Nano Mechanical Devices for Frequency Control and Chemical Sensing* (pp. 1–30). Springer, Singapore. https://doi.org/10.1007/978-981-10-2798-7_23-1

Parsamyan, H. A., Babajanyan, A. Zh., Arakelyan, Sh. Kh., & Lee, K. (2018). DETERMINATION OF GLUCOSE CONCENTRATION IN AQUEOUS SOLUTION BY USING MODIFIED HILBERT SHAPED MICROWAVE METAMATERIAL SENSOR. *Proceedings of the YSU A: Physical and Mathematical Sciences*, *52*(2 (246)), 144–148. https://doi.org/10.46991/PYSU:A/2018.52.2.144

Pasquier, A., Diraison, Y. Le, Joubert, P. Y., & Serfaty, S. (2019). Imaging of a dielectric inclusion using a contactless radio-frequency inductive probe for tissue diagnosis. *Annual International Conference of the IEEE Engineering in Medicine and Biology Society. IEEE Engineering in Medicine and Biology Society. Annual International Conference*, *2019*, 6049–6054. https://doi.org/10.1109/EMBC.2019.8857302

Peeters, M., Eersels, K., Junkers, T., & Wagner, P. (2016). Molecularly Imprinted Polymers: Synthetic Receptors for Diagnostic Medical Devices. *Molecularly Imprinted*

Catalysts: Principles, Syntheses, and Applications, 253–271. https://doi.org/10.1016/B978-0-12-801301-4.00013-X

Pichon, V., & Chapuis-Hugon, F. (2008). Role of molecularly imprinted polymers for selective determination of environmental pollutants--a review. *Analytica Chimica Acta*, *622*(1–2), 48–61. https://doi.org/10.1016/J.ACA.2008.05.057

Piletsky, S. A., Alcock, S., & Turner, A. P. F. (2001). Molecular imprinting: at the edge of the third millennium. *Trends in Biotechnology*, *19*(1), 9–12. https://doi.org/10.1016/S0167-7799(00)01523-7

Poma, A., Turner, A. P. F., & Piletsky, S. A. (2010). Advances in the manufacture of MIP nanoparticles. *Trends in Biotechnology*, *28*(12), 629–637. https://doi.org/10.1016/J.TIBTECH.2010.08.006

Pozar, D. M. (2012). Microwave Engineering, 4th Edition. *John Wiley &Sons, Inc*, 1–756.

Puoci, F., Cirillo, G., Curcio, M., Iemma, F., Spizzirri, U. G., & Picci, N. (2007). Molecularly imprinted solid phase extraction for the selective HPLC determination of α-tocopherol in bay leaves. *Analytica Chimica Acta*, *593*(2), 164–170. https://doi.org/10.1016/J.ACA.2007.04.053

Puoci, F., Iemma, F., & Picci, N. (2008). Stimuli-responsive molecularly imprinted polymers for drug delivery: a review. *Current Drug Delivery*, *5*(2), 85–96. https://doi.org/10.2174/156720108783954888

Quan, J., Saaem, I., Tang, N., Ma, S., Negre, N., Gong, H., White, K. P., & Tian, J. (2011). Parallel on-chip gene synthesis and application to optimization of protein expression. *Nature Biotechnology 2011 29:5*, *29*(5), 449–452. https://doi.org/10.1038/nbt.1847

Rai, A. C., Kumar, P., Pilla, F., Skouloudis, A. N., Di Sabatino, S., Ratti, C., Yasar, A., & Rickerby, D. (2017). End-user perspective of low-cost sensors for outdoor air pollution monitoring. *Science of The Total Environment*, *607–608*, 691–705. https://doi.org/10.1016/J.SCITOTENV.2017.06.266

Ramström, O., & Mosbach, K. (1999). Synthesis and catalysis by molecularly imprinted materials. *Current Opinion in Chemical Biology*, *3*(6), 759–764. https://doi.org/10.1016/S1367-5931(99)00037-X

Rosen, A., Stuchly, M. A., & Vander Vorst, A. (2002). Applications of RF/microwaves in medicine. *IEEE Transactions on Microwave Theory and Techniques*, *50*(3), 963–974. https://doi.org/10.1109/22.989979

Rossignol, J., Barochi, G., De Fonseca, B., Brunet, J., Bouvet, M., Pauly, A., & Markey, L. (2013). Microwave-based gas sensor with phthalocyanine film at room temperature. *Sensors and Actuators B: Chemical*, *189*, 213–216. https://doi.org/10.1016/J.SNB.2013.03.092

Saleh, T. A. (2021). Synthesis of hybrid materials: methods and classification. *Polymer Hybrid Materials and Nanocomposites*, 177–212. https://doi.org/10.1016/B978-0-12-813294-4.00002-9

Schirhagl, R. (2014). Bioapplications for molecularly imprinted polymers. *Analytical Chemistry*, *86*(1), 250–261. https://doi.org/10.1021/AC401251J/ASSET/IMAGES/AC401251J.SOCIAL.JPEG_V03

Scorrano, S., Mergola, L., del Sole, R., & Vasapollo, G. (2011). Synthesis of Molecularly Imprinted Polymers for Amino Acid Derivates by Using Different Functional Monomers. *International Journal of Molecular Sciences 2011, Vol. 12, Pages 1735-1743*, *12*(3), 1735–1743. https://doi.org/10.3390/IJMS12031735

Sellergren, B. (2001). Preface. *Techniques and Instrumentation in Analytical Chemistry*, *23*(C). https://doi.org/10.1016/S0167-9244(01)80001-9

Sellergren, B., & Allender, C. J. (2005). Molecularly imprinted polymers: A bridge to advanced drug delivery. *Advanced Drug Delivery Reviews*, *57*(12), 1733–1741. https://doi.org/10.1016/J.ADDR.2005.07.010

Shahri, A. A., Omidvar, A. H., Rehder, G. P., & Serrano, A. L. C. (2021). A high sensitivity microwave glucose sensor. *Measurement Science and Technology*, *32*(7), 2807–2812. https://doi.org/10.1088/1361-6501/abe1e3

Shahri, A. A., Omidvar, A. H., Rehder, G. P., Serrano, A. L. C., Shahri, A. A., Omidvar, A. H., Rehder, G. P., & Serrano, A. L. C. (2021). A high sensitivity microwave glucose sensor. *MeScT*, *32*(7), 075104. https://doi.org/10.1088/1361-6501/ABE1E3

Shao, J., Huang, Y., & Fan, Q. (2014). Visible light initiating systems for photopolymerization: status, development and challenges. *Polymer Chemistry*, *5*(14), 4195–4210. https://doi.org/10.1039/C4PY00072B

Stuchly, M. A., Kraszewski, A., Stuchly, S. S., & Smith, A. M. (1982). Dielectric properties of animal tissues in vivo at radio and microwave frequencies: comparison between species. *Physics in Medicine & Biology*, *27*(7), 927. https://doi.org/10.1088/0031-9155/27/7/004

Suedee, R., Srichana, T., Chotivatesin, R., & Martin, G. P. (2002). Stereoselective release behaviors of imprinted bead matrices. *Drug Development and Industrial Pharmacy*, *28*(5), 545–554. https://doi.org/10.1081/DDC-120003450

The top 10 causes of death. (n.d.). https://www.who.int/news-room/fact-sheets/detail/the-top-10-causes-of-death

Tunis, S. L., & Minshall, M. E. (2010). Self-monitoring of blood glucose (SMBG) for type 2 diabetes patients treated with oral anti-diabetes drugs and with a recent history of monitoring: cost-effectiveness in the US. *Current Medical Research and Opinion*, *26*(1), 151–162. https://doi.org/10.1185/03007990903400071

Turner, A. P. F. (2000). Biosensors--Sense and Sensitivity. *Science*, *290*(5495), 1315–1317. https://doi.org/10.1126/SCIENCE.290.5495.1315

Updike, S. J., & Hicks, G. P. (1967a). Reagentless Substrate Analysis with Immobilized Enzymes. *Science*, *158*(3798), 270–272. https://doi.org/10.1126/SCIENCE.158.3798.270

Updike, S. J., & Hicks, G. P. (1967b). The Enzyme Electrode. *Nature 1967 214:5092*, *214*(5092), 986–988. https://doi.org/10.1038/214986a0

Van Dieren, S., Beulens, J. W. J., Van Der Schouw, Y. T., Grobbee, D. E., & Neal, B. (2010). The global burden of diabetes and its complications: an emerging pandemic. *European Journal of Cardiovascular Prevention and Rehabilitation : Official Journal of the European Society of Cardiology, Working Groups on Epidemiology & Prevention and Cardiac Rehabilitation and Exercise Physiology*, *17 Suppl 1*(SUPPL. 1). https://doi.org/10.1097/01.HJR.0000368191.86614.5A

Velez, P., Munoz-Enano, J., Grenier, K., Mata-Contreras, J., Dubuc, D., & Martin, F. (2019). Split Ring Resonator-Based Microwave Fluidic Sensors for Electrolyte Concentration Measurements. *IEEE Sensors Journal*, *19*(7), 2562–2569. https://doi.org/10.1109/JSEN.2018.2890089

Voiculescu, I., & Nordin, A. N. (2012). Acoustic wave based MEMS devices for biosensing applications. *Biosensors and Bioelectronics*, *33*(1), 1–9. https://doi.org/10.1016/J.BIOS.2011.12.041

Voinova, M. V. (2009). On mass loading and dissipation measured with acoustic wave sensors. *Journal of Sensors*, *2009*. https://doi.org/10.1155/2009/943125

Wang, C., Cai, F., Li, F., Meng, L., Li, J., Wu, J., Kang, Y., & Zheng, H. (2016). A highly sensitive compact liquid sensor based on slotted phononic crystal plates. *Lab on a Chip*, *16*(23), 4595–4600. https://doi.org/10.1039/C6LC01151A

Widi, R. K., Trisulo, D. C., Budhyantoro, A., & Chrisnasari, R. (2017). Preparation of immobilized glucose oxidase wafer enzyme on calcium-bentonite modified by surfactant. *IOP Conference Series: Materials Science and Engineering*, *223*(1), 012050. https://doi.org/10.1088/1757-899X/223/1/012050

Xu, X. H., Wu, H. S., Zhang, C. J., & Jin, Z. H. (2001). Morphological properties of AlN piezoelectric thin films deposited by DC reactive magnetron sputtering. *Thin Solid Films*, *388*(1–2), 62–67. https://doi.org/10.1016/S0040-6090(00)01914-3

Yankin, S., Talbi, A., Du, Y., Gerbedoen, J. C., Preobrazhensky, V., Pernod, P., & Bou Matar, O. (2014). Finite element analysis and experimental study of surface acoustic wave propagation through two-dimensional pillar-based surface phononic crystal. *Journal of Applied Physics*, *115*(24), 244508. https://doi.org/10.1063/1.4885460

Ye, L., Cormack, P. A. G., & Mosbach, K. (2001). Molecular imprinting on microgel spheres. *Analytica Chimica Acta*, *435*(1), 187–196. https://doi.org/10.1016/S0003-2670(00)01248-4

Yoo, E. H., & Lee, S. Y. (2010). Glucose biosensors: an overview of use in clinical practice. *Sensors (Basel, Switzerland)*, *10*(5), 4558–4576. https://doi.org/10.3390/S100504558

Zhang, M., Du, L., Fang, Z., & Zhao, Z. (2015). Micro Through-hole Array in top Electrode of Film Bulk Acoustic Resonator for Sensitivity Improving as Humidity Sensor. *Procedia Engineering*, *120*, 663–666. https://doi.org/10.1016/J.PROENG.2015.08.703

Zhang, Y., Chen, D., Zhang, Y., & Chen, D. (2013). Propagation of Acoustic Wave in Crystals. In *Multilayer Integrated Film Bulk Acoustic Resonators* (pp. 15–29). Springer Berlin Heidelberg. https://doi.org/10.1007/978-3-642-31776-7_2

Zhang, Y., Luo, J., Flewitt, A. J., Cai, Z., & Zhao, X. (2018). Film bulk acoustic resonators (FBARs) as biosensors: A review. *Biosensors and Bioelectronics*, *116*, 1–15. https://doi.org/10.1016/J.BIOS.2018.05.028

Zhao, X., Ashley, G. M., Garcia-Gancedo, L., Jin, H., Luo, J., Flewitt, A. J., & Lu, J. R. (2012). Protein functionalized ZnO thin film bulk acoustic resonator as an odorant biosensor. *Sensors and Actuators B: Chemical*, *163*(1), 242–246. https://doi.org/10.1016/J.SNB.2012.01.046

Zhong, S., & Jang, C. H. (2014). Highly sensitive and selective glucose sensor based on ultraviolet-treated nematic liquid crystals. *Biosensors and Bioelectronics*, *59*, 293–299. https://doi.org/10.1016/J.BIOS.2014.03.070